UNIVERSIDAD NACIONAL AUTÓNOMA DE MÉXICO

POSGRADO EN ASTROFÍSICA

ASTROFÍSICA OBSERVACIONAL

ATMOSPHERIC CHARACTERIZATION OF SATURN-LIKE PLANETS THROUGH MULTI-BAND PHOTOMETRY

TESIS
QUE PARA OPTAR POR EL GRADO DE:
MAESTRO EN CIENCIAS (ASTROFÍSICA)

PRESENTA:
BRIONES RIVERA MIGUEL

DRA. YILEN GÓMEZ MAQUEO CHEW
DRA. ROMINA PAOLA PETRUCCI
INSTITUTO DE ASTRONOMÍA

INSTITUTO DE ASTRONOMÍA, CIUDAD UNIVERSITARIA, CD. MX., ENERO 2022

Dedication

This work is dedicated to my parents and brother that supported me through the development of this work and always encouraged me to move forward.

Acknowledgments

This research was possible thanks to the Programa de Apoyo a Proyectos de Investigación e Innovación Tecnológica (PAPIIT) from the UNAM IN-107518 and BG-101321.

Abstract

Nowadays, we know it is possible to obtain information about the atmospheric composition of a planet by analyzing the variation of the depth of its planetary transits as a function of wavelength. Until now, several studies of this kind have been made for Jupiter-like planets (Ciceri et al. 2016; Sing et al. 2016; Mancini et al. 2018), compared to that, the number of published papers with Saturn-type planets is small. Having this in mind, we present the results of my Master's degree thesis, which has the goal of studying the atmospheric composition of a sample of Saturn-type exoplanets by using light curves of their planetary transits obtained in different filters. Specifically this work focuses on the transmission spectra of HATS-6b (Hartman et al. 2015a) and WASP-69b (Anderson et al. 2014).

We present one newly acquired light curve for each planet and analyze these in conjunction with transit light curves from the literature. I reduced the time-series photometric data to obtain the corresponding light curves. In the case of HATS-6b, I analyzed a total of 10 transit light curves in different filters, spanning from 0.4 to 1.1 microns, and in the case of WASP-69b, I analyzed a total of 25 light curves that cover from 0.4 to 1.2 microns. I modeled each transit light curve using a dedicated software JKTEBOP (Southworth 2013) to derive the average photometric parameters of the transiting system. Once the average photometric parameters were determined, I derived the depth and the central time of the transit for each of the light curves for the given filter composing thus the observed transmission spectrum for the planet.

We wish to understand the physical and chemical properties of the planet's atmosphere through the comparison to the atmospheric models from Goyal et al. (2018) available in the literature. We fitted the derived transmission spectra of the two planets in our sample with our code that compares the observed transmission spectrum to a database which covers a wide range of atmospheric properties to find the best-fitting atmospheric model by minimizing its χ^2. The physical properties of the transmission spectrum provide constraints on the observed characteristics of the transmission spectra and consequently the planetary atmospheres of the two planets in our sample.

Our results for WASP-69b appear to indicate the presence of Na and Rayleigh scattering in the atmosphere of the planet, in agreement with previous studies done with this planet. For HATS-6b, we detect the presence of Rayleigh scattering in its atmosphere, as well as Na and K. In both cases, the results found seem to indicate the presence of water vapor in the atmosphere, however, this cannot be confirm in this work given the lack of observations in the near-infrared and infrared parts of the transmission spectra of the planets. Overall, more observations are needed to grasp a better understanding of the atmospheres from these Saturn-type planets.

Contents

Chapter 1

Introduction

1.1 Exoplanets

An extrasolar planet, or exoplanet, is a planet that orbits other stars different to our own Sun. The first exoplanets were discovered in the early 1990's. Oddly enough, the first plausible detection of a planet was found around a radio pulsar (Wolszczan & Frail 1992). However it was not until 1995 by Mayor & Queloz (1995) that an exoplanet orbiting around a Solar type star was discovered for the first time; receiving the Nobel Prize of Physics in 2019 for this mayor achievement. Following this breakthrough, dozens of exoplanets were discovered in the following years using the radial velocity technique. Regarding the photometric search for exoplanets it should be said that the first transit detected was reported in 1999 (Henry et al. 2000; Charbonneau et al. 2000). Then by 2004, using the gravitational microlensing technique the first planet was reported (Bond et al. 2004). Some other mayor breakthroughs include the first wide field star survey discoveries in 2004 (Bakos et al. 2002; Pollacco et al. 2006), and the first discovery with space telescopes in 2008 (Borucki et al. 2007). As of October 2021, a total of 4843 known planets have been confirmed (Schneider et al. 2011).

1.2 Transit Model

A planetary transit is a phenomenon that occurs when a planet passes between its host star and an observer on Earth. Specifically, when the planet transits in front of its star, the total flux of light we observe diminishes a certain amount, and this fractional change in the brightness of the star is commonly expressed as ΔF, i.e. the flux variation. It is possible to consider the transit of a planet in front of its star as a simply geometry problem where one small disk (the planet) moves in front of a bigger disk (the host star) that has a fraction of its light blocked and thus, diminishing the total amount of light that we detect. In reality, the difficulty of studying the transit of a planet across its host star increases when considering other phenomena, such as the effects of stellar limb darkening (see Section 4.3), blending from background objects and effects due to eccentricity of the planetary orbit (Perryman 2011). Also, the planet itself may be emitting some light because of the presence of an atmosphere or simply reflecting its host star light on its surface (much like the moon with sunlight). For simplicity of the calculations, this additional flux coming from the planet is often considered a negligible amount. Also relevant is the assumption that both the star and planet are of spherical shape, again, this is likely not the case at all; but it allows to simplify the mathematics needed to explain the transit phenomenon.

With the assumptions of zero flux from the planet and spherical shapes for both star and planet we can say that ΔF is given by a ratio of the areas of both planet and host star, i.e.,

$$\Delta F \approx \left(\frac{R_p}{R_s}\right)^2 = k^2$$

where R_p is the radius of the planet, R_s the radius of the star, k is the radius ratio, and k^2 is commonly known as the transit depth of the planet. The four principal parameters that one can inferred from the light curve of a transit are: the period P (two or more transits are need to know P), the transit depth ΔF, the total transit duration, i.e., the interval between the first and fourth contact points t_T, and the transit duration between ingress and egress, i.e, the interval between the second and third contact points t_F (Perryman 2011). When a transit occurs, there are four contact points, that represent the moments where the disk of the planet touches

the stellar disk. The first two contact points correspond to the transit ingress and the third and fourth contact points to the transit egress. In Figure 1.1 we show a diagram with the main observable parameters from a transit light curve. During t_F the light curve is relatively (but not totally) flat.

From a transit light curve, it is possible to determine the stellar mass M_s, the stellar radius R_s, the companion radius R_p, the orbital semi-major axis a, and the orbital inclination i (Seager & Mallén-Ornelas 2003). However, in order to achieve this, several assumptions must be made. For this solution to work, the planet's orbit is assumed to be circular, i.e., with an eccentricity e=0; the mass of the planet M_p smaller than the stellar mass $M_p \ll M_s$; the stellar mass-radius relation should be known and the light must come from a single stellar object, instead of two or more background stars/objects (Seager & Mallén-Ornelas 2003).

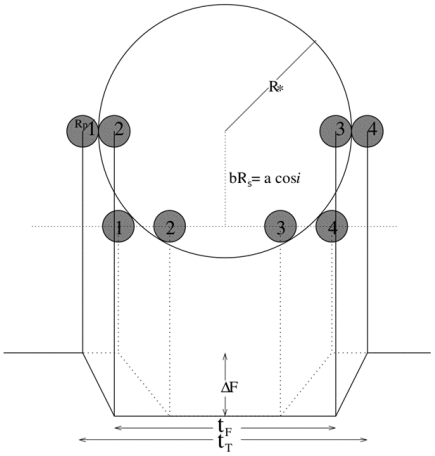

Figure 1.1: Diagram with the definition of the transit light curve observables. The geometry of the star-system is shown on the upper part of the diagram. In the lower part, the schematic of two light curves are shown as solid and dotted lines. Here we see the transit depth ΔF of the planet, the total transit duration t_T, and the transit duration between ingress and egress t_F. During the duration of t_F, the planet is fully inside the disk of the host star. In the upper part we see the first, second, third and fourth contact points of the planet as it transits its host star, where R_p is the radius of the planet, R_s is the radius of the host star and b is the impact parameter with an orbital inclination i. The difference between the solid and dotted transit light curves at the bottom can be attributed to a different b, which determines the shape of the light curve. Image taken from Seager & Mallén-Ornelas (2003).

In Seager & Mallén-Ornelas (2003) a set of analytical expressions was derived to relate the observable parameters of a transit with the orbital parameters. The process presented in that work starts by defining a set of equations related to the observable parameters P, ΔF, t_T, t_F that we previously mentioned. The first equation is the transit depth,

$$\Delta F = \left(\frac{R_p}{R_s}\right)^2,$$

followed by the transit shape, which is defined as the ratio of the duration of that "flat part" of the light curve, t_F, and the total transit duration t_T,

$$\frac{\sin\left(t_F \pi / P\right)}{\sin\left(t_T \pi / P\right)} = \frac{\sqrt{[1-(R_p/R_s)]^2 - [(a/R_s)\cos i]^2}}{\sqrt{[1+(R_p/R_s)]^2 - [(a/R_s)\cos i]^2}},$$

the total transit duration,

$$t_T = \frac{P}{\pi} \arcsin\left(\frac{R_s}{a}\sqrt{\frac{[1+(R_p/R_s)]^2 - [(a/R_s)\cos i]^2}{1-\cos^2 i}}\right),$$

Kepler's third law, assuming a circular orbit, where G is the universal gravitational constant and M_p the mass of the planet,

$$P^2 = \frac{4\pi^2 a^3}{G(M_s + M_p)},$$

and the stellar mass-radius relation,

$$R_s = cM_s^x,$$

where c is a constant coefficient for stellar sequences (i.e. main sequence, giants, etc.), and x is the power law of the stellar sequence (Seager & Mallén-Ornelas 2003).

Some of the equations can be simplified if one assumes that $R_s \ll a$, which is a reasonable assumption and equivalent to $t_T\pi/P \ll 1$ (Seager & Mallén-Ornelas 2003). Under this assumption, $\arcsin x \approx x$ and $\sin x \approx x$, where x is defined as above; so the transit shape equation becomes independent of P and now,

$$\left(\frac{t_F}{t_T}\right)^2 = \frac{(1 - R_p/R_s)^2 - [(a/R_s)\cos i]^2}{(1 + R_p/R_s)^2 - [(a/R_s)\cos i]^2},$$

and the total transit equation becomes,

$$t_T = \frac{PR_s}{\pi a}\sqrt{\left(1 + \frac{R_p}{R_s}\right)^2 - \left(\frac{a}{R_s}\cos i\right)^2}.$$

The analytical solutions presented in Seager & Mallén-Ornelas (2003) for four combinations of physical parameters that can be obtained from the observable parameters (ΔF, t_T, t_F, P) could allow us to calculate the five physical parameters (R_s, M_s, i, a, R_p) of the system. These four combinations are: the planet-star radius ratio,

$$\frac{R_p}{R_s} = \Delta F,$$

the impact parameter b, which is defined as the projected distance between the planet and star centers during midtransit (see Figure 1.1), and is derived from the planet-star radius ratio and the transit shape equation,

$$b \equiv \frac{a}{R_s}\cos i = \sqrt{\frac{(1 - \sqrt{\Delta F})^2 - (t_F/t_T)^2(1 + \sqrt{\Delta F})^2}{1 - (t_F/t_T)^2}},$$

the ratio a/R_s, derived from the transit duration equation,

$$\frac{a}{R_s} = \frac{2P}{\pi}\frac{\Delta F^{1/4}}{\sqrt{(t_T^2 - t_F^2)}},$$

and the stellar density ρ_s, derived from the a/R_s equation and Kepler's third law (assuming $M_p \ll M_s$),

$$\rho_s = \frac{32}{G\pi}P\frac{\Delta F^{3/4}}{(t_T^2 - t_F^2)^{3/2}}.$$

It should be noted that for the b, a/R_s and ρ_s equations, the solutions are shown after taking into consideration the previously mentioned assumptions of $R_s \ll a$ and $t_T\pi/P \ll 1$. For further details on the development of the solution, we suggest consulting Seager & Mallén-Ornelas (2003).

The five physical parameters can be derived from the equations above. The stellar mass, in solar mass units is then,

$$\frac{M_s}{M_\odot} = \left(k^3\frac{\rho_s}{\rho_\odot}\right)^{1/(1-3x)},$$

the stellar radius in solar radius units,

$$\frac{R_s}{R_\odot} = k\left(\frac{M_s}{M_\odot}\right)^x = \left(k^{1/x}\frac{\rho_s}{\rho_\odot}\right)^{x/(1-3x)},$$

the orbital radius a, derived from M_s and Kepler's third law with $M_p \ll M_s$,

$$a = \left(\frac{P^2GM_s}{4\pi^2}\right)^{1/3},$$

the orbital inclination i,

$$i = \cos^{-1} b\frac{R_s}{a},$$

and the planetary radius,

$$\frac{R_P}{R_\odot} = \frac{R_s}{R_\odot}\sqrt{\Delta F}.$$

The probability of any transit being detectable is given by the fraction of the celestial sphere swept out by the shadow of the planet (Bozza et al. 2016). For a grazing transit to occur, a planet with R_p must meet the condition $R_s + R_p > a\cos i > R_s - R_p$. For a full transit to happen, $a\cos i > R_\star + R_p$ needs to become true (Bozza et al. 2016). So if the planet transits, then the shadow it casts on the celestial sphere can be calculated. As explained in Bozza et al. (2016), the fraction of the solid angle on the celestial sphere enclosing cones with opening angles in the range i to $i + di$ is given by

$$\frac{d\Omega}{4\pi} = \frac{2\pi \sin i di}{4\pi} = \frac{d(\cos i)}{2}.$$

The probability that a partial or full transit will occur in a randomly oriented orbit is given by

$$Pr\left(\cos i < \frac{R_s + R_p}{a}\right) = \frac{1}{2}\int_{-(R_s+R_p)/a}^{(R_s+R_p)/a} d(\cos i) = \frac{R_s + R_p}{a},$$

and when $R_p \ll R_s$, the probability of a transit is simply R_s/a, i.e.,

$$Pr\left(\cos i < \frac{R_s}{a}\right) \simeq 0.0046\left(\frac{R_s}{R_\odot}\right)\left(\frac{1au}{a}\right).$$

1.3 Transmission Spectrum

As explained in the previous section, if we can measure the transit depth of a planet as it passes between its host star and our line of sight, we can effectively calculate the radius of the planet relative to the parent star. When a planet transits, the radius that we measure will directly depend on whether the planet has an atmosphere or not. If the planet lacks of any kind of atmosphere, then the radius that we measure will remain constant in every wavelength we observe it with. However, if the planet is enveloped by any kind of atmosphere then when observed, its transit depth will vary, appearing bigger or smaller at different wavelengths. This means that the transit depth of a planet is wavelength dependent and will have different values, depending on the filter used for its observation (Seager & Sasselov 2000). Thus, the transmission spectrum is simply a measure of the transit depth as as function of wavelength (Perryman 2011). What we observe are the absorption and/or scattering features of the planetary atmosphere, that have been imprinted in the light of the host star (Seager & Sasselov 2000; Brown 2001). A transmission spectrum can be expressed as

$$\Delta\lambda = \left(\frac{R_{p,\lambda}}{R_{s,\lambda}}\right)^2 = \frac{2}{R_s^2}\int_0^{R_{max}} rdr(1 - e^{-\tau_\lambda(r)}),$$

where λ is the wavelength, R_p is the planet radius, R_s is the stellar radius, R_{max} is the maximum height of observable atmosphere, r is the height in the atmosphere perpendicular to the direction of the ray, and $\tau(r)$ is the slant optical depth through the chord traversed by a ray at r (Perryman 2011). The optical depth of the incident stellar rays varies according to the pressure, temperature and chemical composition of the atmosphere of the planet (Perryman 2011).

It is possible to determine roughly the amplitude of spectral features in a transmission spectrum using the atmospheric scale height H (Perryman 2011). The atmospheric scale height can be defined as change in altitude over which the pressure drops by a factor e (Deeg & Belmonte 2018). The scale height equation is given by

$$H = \frac{kT}{\mu g},$$

where k is the Boltzmann constant, T the temperature of the planetary atmosphere, μ the mean molecular weight of the atmosphere and g the surface gravity. Then, the amplitude of spectral features in the transmission spectrum is given by

$$\delta_\lambda = \frac{(R_p + nH)^2}{R_s^2} - \left(\frac{R_p}{R_s}\right)^2 \approx 2nR_pH/R_s^2,$$

where n is the number of scale heights crossed at wavelengths with high opacity (Perryman 2011).

1.4 Atmospheric Models

The goal of defining atmospheric models is to better understand the composition and characteristics of the atmosphere of a planet. Some of the things one can learn from these models include the temperature pressure profile, day-night temperature gradients, circulation patterns and chemical composition (Perryman 2011). It is known that for any ideal gas that is in hydrostatic equilibrium, the number density per unit area above an altitude z is

$$N \sim \frac{p(z)}{\mu g(z)} = n(z)H,$$

where H is the atmospheric scale height, μ is the mean molecular weight, $p(z)$ is the pressure and $g(z)$ is the gravity. For a isothermal gas, this provides information on some basic atmospherical characteristics (Chamberlain & Hunten 1987; Houghton 2002).

In all planetary atmospheres there are always some radiative transfer physics in play because of the irradiation coming from the host star, and the complexity of this depends on the atomic and molecular composition, temperature and pressure that describe the absorption properties of the atmosphere. For example, the upper atmosphere of hot Jupiters is dominated by radiative transfer, with the radiation efficiency, depending on the emission and absorption characteristics of the elements and molecules present (Perryman 2011). The radiative transfer in atmospheres mainly fueled from stellar irradiation can also modify the pressure-temperature relation that describes the atmosphere and in turn this variation affects the mass-radius relation of the planet (Perryman 2011). An interesting phenomenon present in atmospheres is temperature inversion, where the presence of strong absorbers in the visible and ultraviolet part of the spectrum at the upper layers of the atmosphere heat up and prevent the energy trapped in the inner parts of the atmosphere to escape, leading to a thermal inversion where the temperature in the atmosphere increases with altitude (Hubeny et al. 2003; Guillot 2010). Normally this is not the case as stellar irradiation is expected to heat and penetrate to even the lower parts of an atmosphere, heating it from below which causes the temperature to decrease with altitude.

Another parameter to consider in atmospheric models is albedo. The albedo is a measure of the reflectivity of a planet atmosphere from the total absorption and scattering of light (Perryman 2011). Albedos are heavily dependent on the characteristics of the atmosphere. When a planet has an extensive coverage of clouds in its atmosphere the light reflected from its host star increases and thus, there is a high albedo, which reduces the infrared luminosity and increases the stellar radiation that is reflected (Perryman 2011).

There has been a great development in the field of atmospheric modeling for exoplanets and the way scientist can interpret physical characteristics of a planet from looking at its transmission spectrum. Thanks to the collaborations of several groups around the world, there has been a wide development of models for hot gas giants (e.g. hot Jupiters, hot Neptunes), super Earths and young planets detected by direct imaging. The complexity of these models has increased over time from one-dimensional (1-D) to three-dimensional (3-D) models as well as those that can be adjusted to have a solar-composition or thermochemical equilibrium. Some of the models developed over the years but not all, can be seen in Seager & Sasselov (2000); Sudarsky et al. (2000); Brown (2001); Sudarsky et al. (2003); Hubeny et al. (2003); Guillot (2010); Madhusudhan & Seager (2010); Budaj et al. (2012); Perez-Becker & Showman (2013); Amundsen et al. (2014a); Showman et al. (2015); Sing et al. (2016); Komacek et al. (2017); Goyal et al. (2018, 2019).

The classical models that have been developed for explaining exoplanetary atmospheres include in one way or another equilibrium conditions. For example, given the planet gravity, radius, incident stellar radiation and some elemental abundances, it is possible for equilibrium models to compute the stellar spectrum with the assumption that the modeled plane-parallel atmosphere is under radiative-convective equilibrium, local thermodynamic equilibrium (LTE), hydrostatic equilibrium and chemical equilibrium (Perryman 2011; Deeg & Belmonte 2018). The radiative-convective equilibrium can be constrained to determine a pressure-temperature (P-T) profile that is consistent with the incident radiation from the host star and the chemical composition. The advantage of equilibrium models is that they can represent with a high level of accuracy atmospheres in conditions where the dynamics of the atmosphere and non-equilibrium processes do not influence the temperature structure and chemical composition in a significant way (Perryman 2011).

This scenario happens when considering a chemical equilibrium in the atmosphere. There are several physical processes that when present, can drive the planetary atmosphere out of equilibrium. Some processes that have been studied in exoplanetary atmospheres are: vertical mixing of species due to turbulent processes on timescales shorter than the equilibrium reaction time scales; photochemical reactions of species driven by strong incident radiation and molecular diffusion of gravitational settling of species (Deeg & Belmonte 2018). It is expected that non-equilibrium chemistry will be dominant by exoplanet atmospheres, as it has been found out that it is

prevalent in the solar system giant planets and some brown dwarfs (Deeg & Belmonte 2018). It also has been shown by some studies that non-equilibrium is prevalent in cooler atmospheres with a $T_{eq} \lesssim$1300K, whereas atmospheres with a $T_{eq} \gtrsim$2000K tend to be in chemical equilibrium in a steady state (Deeg & Belmonte 2018).

1.5 Hot Jupiters and Saturn-like planets

Gas giant planets are basically giant balls made primarily of hydrogen and helium, with some small fraction of heavier elements (e.g. carbon, oxygen, nitrogen) and molecules like water or carbon dioxide (Perryman 2011). In broad terms it can be said that gas giant exoplanets have a similar range of masses and radii to that of our own solar system giants, Jupiter and Saturn; so it is quite probable that these exoplanets also have a similar structure in their interior. Hot Jupiters are gas giant planets that have a $P \lesssim 7$ d, a $M_p \gtrsim 100\ M_\oplus$ and orbit very close to their host star with $a < 5$ au (Deeg & Belmonte 2018). This type of gas giants are relative scarce, with an occurrence rate of about 1% in nearby Sun-like main sequence-stars (Wright et al. 2012). Transit probability for hot Jupiters is ∼10% (Deeg & Belmonte 2018).

Throughout the years various proposals have been made for the classification of gas giant atmospheres. Two of the systems proposed are: A system which assigned five classes to gas giants presented in Sudarsky et al. (2000, 2003). Here the properties of the planet atmospheres depend on the temperature. In this classification, class I would present NH_3 clouds and a $T_{eq} \lesssim 150K$, meaning a planet orbiting a cool star or with a distant orbit. Class II planets would have clouds of water, $T_{eq} \sim 150 - 250K$, and the atmospheres would consist mainly of H_2 and hydrogen-rich molecules (e.g. CH_4). Class III planets would be cloudless, $T_{eq} \sim 300 - 850K$, this class of planet would have no cloud cover due to absence of condensates that are suitable; an so they would appear as blue globes (due to Rayleigh scattering and CH_4 absorption) . Class IV planets would contain alkali metal in their atmospheres, $T_{eq} \gtrsim 900K$, where the dominant carbon molecule would be carbon monoxide, and prominent lines of alkali metals such as sodium and potassium are present. Finally for class V, $T_{eq} \gtrsim 1400K$, these extremely hot planets would have silicate and iron cloud decks high up in the atmosphere.

Other classification system was suggested by Burrows et al. (2007) and Fortney et al. (2008), as most hot Jupiters can be classified neatly in two categories that are characterized by the stellar incident flux and its relation with opacities produced by titanium(II) oxide (TiO) and vanadium(II) oxide (VO) (Hubeny et al. 2003). The first type is class pM, planets in this category are characterized for having higher temperatures and a strong incident stellar flux which gives a gas-phase for TiO and VO, and also have temperature inversion due to the absorbing molecules in high part of the atmospheres. The second class, pL, is made of cooler planet which receive significant less stellar flux. however the incident flux in the atmosphere is absorbed in deeper layers, with no temperature inversion and the condensation of titanium and vanadium occurs.

Saturn-type planets have not been studied as extensively as hot Jupiters, however, there are some Saturn-type systems that are worth mentioning here. WASP-117b is a Saturn-type planet first reported in Lendl et al. (2014) with a period of 10 days and a high eccentricity of 0.302. In Anisman et al. (2020), water vapor and a layer of opaque clouds appears to have been detected. This adds WASP-117b to a list of similar planets that appears to have water vapor features and a layer of clouds that can weaken the transmission spectrum signal (Sing et al. 2016). Another important discovery related to WASP-117 came from Carone et al. (2021), where they detect high level of atmospheric metallicity about log (2.58) and a lack of methane in its atmosphere. Another Saturn-type planet is WASP-131b, first discovered by Hellier et al. (2017). Not much is known about its planetary atmosphere. Southworth et al. (2020) studied the planet physical properties and found that its measurements for temperature and metallicity were in agreement with those reported by Hellier et al. (2017). The last planet that we want to present has been extensively studied ever since it was first reported by Faedi et al. (2011), WASP-39b. Its atmospheric properties have been studied by Sing et al. (2016); Nikolov et al. (2016); Fischer et al. (2016); Wakeford et al. (2018); Pinhas et al. (2019); Kirk et al. (2019). The metallicity of this planet has been constrained between solar and slightly sub-solar values, while the C/O ratio is also constrained to a solar-like ratio, where there are also being clues for the presence of Na and K (Goyal et al. 2018).

In this work, we present the analysis of newly acquired light curves for WASP-69b and HATS-6b and light curves that we gathered from the literature. We derived the transit depth of each light curve and compose a transmission spectrum for each of the planets. Our objective is to analyze the composition and characteristics of the atmosphere of these two Saturn-type exoplanets by comparing their transmission spectra to the atmospheric models from Goyal et al. (2018).

Chapter 2

Sample Of Saturn-like Exoplanets

In this chapter, we present the criteria used to select the Saturn-type planets of our initial sample, and we describe the Saturn-type planets finally analyzed in this thesis. Saturn type planets are defined as planets with a mass between 0.22 and 0.37 M_J (Sato et al. 2005; Johnson et al. 2018; Lendl et al. 2012). For reference, Saturn itself has a mass of 0.29 M_J[1]. We compiled a list with all the type-like Saturn planets discovered up to August 2018. This data is presented in Table 2.1.

We used Table 2.1 as a starting point for choosing the most suitable planets to study in this work. The requirements set to chose the planets are: the planet must be observable in the Southern Hemisphere (given that the telescopes we use to perform our observations are located there, see Chapter 3), the host star must have a visual magnitude $V \leq 14$ mag, the planet must produce a transit depth of at least 0.010 magnitudes or higher, and the planet must not have any previous transmission spectrum reported in the literature. We excluded the only Saturn-type planet in our initial sample observed by the CoRoT mission, because the host-star V magnitude is >14 mag. We also excluded objects from the Kepler mission, given that it only studies objects in the Northern Hemisphere. And finally, we excluded those systems observed by GROND, because almost all of them have a transmission spectrum already built (HATS-6b being one exception (Hartman et al. 2015a)).

After considering the previously mentioned requirements, we were left with six potential candidates: WASP-39b, WASP-29b, WASP-69b, WASP-117b, HATS-6b and WASP-131b. We decided two of the planets that had no previous transmission spectrum and for which we also had some observations available, WASP-69b and HATS-6b. We also selected a Saturn-type planet that could serve as a control object, i.e., a Saturn-type planet that had a transmission spectrum already published in the literature and its atmospheric properties extensively characterized, so that we could verify that our methodology was indeed right. In Table 2.2, we present the transit, stellar and planetary parameters of HATS-6b and WASP-69b. In Sections 2.1 and 2.2, we present some relevant stellar and planetary parameters of these two systems.

2.1 The WASP-69b Planet

WASP-69b is a Saturn-type planet with a mass of 0.26 ± 0.017 M_J, a radius of 1.057 ± 0.047 R_J and an equilibrium temperature of 963 ± 18 K that was first detected by Anderson et al. (2014). This planet orbits its host star every 3.86 days, it has an orbital inclination of 86.71 ± 0.20 ° and an adopted eccentricity of 0. It orbits around an active mid-K dwarf with a stellar mass of 0.826 ± 0.029 $M_\odot$, a radius of 0.813 ± 0.028 $R_\odot$, an effective temperature of 4715 ± 50 K and a metallicity [Fe/H] of 0.144 ± 0.077 dex (Anderson et al. 2014).

2.2 The HATS-6b Planet

HATS-6b is a Saturn-type planet first reported by Hartman et al. (2015a). It has a planetary mass of 0.319 ± 0.070 M_J, a radius of 0.998 ± 0.019 R_J and an equilibrium temperature of 712.8 ± 5.1 K. HATS-6 b orbits its host star every 3.33 days, has an orbital inclination of 88.210 ± 0.084 ° with a fixed eccentricity of zero. It orbits around a M1 star with a mass of 0.574 ± 0.027 $M_\odot$, with a radius of 0.570 ± 0.011 $R_\odot$, with an effective temperature of 3724 ± 18 K and a metallicity [Fe/H] of 0.200 ± 0.091 dex (Hartman et al. 2015a).

[1]The mass of Saturn an other data can be check in the following site: https://nssdc.gsfc.nasa.gov/planetary/factsheet/saturnfact.html

Table 2.1: Initial sample of Saturn-type exoplanets

Planet	Mass (M_J)	Radius (R_J)	V (mag)	Transit depth (mag)	N_{obs}	N_{fil}	$Transspec$	Discovery Paper
Kepler-396b	0.220	0.310	-	-	0	0	No	Yang et al. (2013)
EPIC 201498078b	0.223	0.850	10.60	-	1	1	No	Johnson et al. (2018)
HATS-5b	0.237	0.912	12.63	0.0125	11	4	No	Zhou et al. (2014)
WASP-29b	0.243	0.841	11.30	0.0108	1	1	No	Hellier et al. (2010)
Kepler-145c	0.250	0.350	11.93	-	1	1	No	Xie (2014)
KOI-188 b	0.250	0.978	15.00	-	1	1	No	Hébrard et al. (2014)
WASP-69b	0.260	0.813	9.87	0.0193	6	6	No	Anderson et al. (2014)
HATS-43b	0.261	1.180	13.59	0.0239	6	2	No	Brahm et al. (2018)
HAT-P-38b	0.267	0.825	12.56	0.0097	40	3	Yes	Sato et al. (2012)
CoRoT-25b	0.270	1.080	15.00	-	3	1	No	Almenara et al. (2013)
WASP-131b	0.270	1.220	11.40	0.0073	7	4	No	Hellier et al. (2017)
HATS-20b	0.273	0.776	13.76	0.0087	11	3	No	Bhatti et al. (2016)
WASP-117b	0.275	1.021	10.15	0.0087	6	3	No	Lendl et al. (2014)
Kepler-277 b	0.280	0.261	13.40	-	1	1	No	Xie (2014)
WASP-126b	0.284	0.960	10.80	0.0066	4	4	No	Maxted et al. (2016)
WASP-39b	0.280	1.270	12.10	0.0215	30	22	Yes	Faedi et al. (2011)
KOI-192b	0.290	1.230	14.50	-	1	1	No	Hébrard et al. (2014)
HAT-P-19b	0.292	1.132	12.90	0.0215	32	6	Yes	Hartman et al. (2011)
WASP-21b	0.300	1.210	11.60	0.0130	14	8	No	Bouchy et al. (2010)
WASP-83b	0.300	1.040	12.90	0.0112	4	1	No	Hellier et al. (2015)
HAT-P-51b	0.309	1.293	13.44	0.0176	14	3	No	Hartman et al. (2015b)
WASP-151b	0.310	1.130	12.90	0.0110	7	3	No	Demangeon et al. (2018)
WASP-20b	0.313	1.459	10.68	0.0125	9	2	No	Anderson et al. (2015)
HATS-6b	0.319	0.998	15.16	0.0342	8	7	No	Hartman et al. (2015a)
HATS-21b	0.332	1.123	12.19	0.0138	8	2	No	Bhatti et al. (2016)
Kepler-16 (AB)b	0.333	0.754	12.00	-	1	1	Yes	Doyle et al. (2011)
HAT-P-67b	0.340	2.085	10.06	0.0076	9	4	No	Zhou et al. (2017)
KOI-195b	0.340	1.090	15.00	-	1	1	No	Hébrard et al. (2014)
HD 149026b	0.357	0.718	8.15	0.0031	30	4	Yes	Sato et al. (2005)
WASP-49b	0.378	1.115	11.36	0.0149	38	3	Yes	Lendl et al. (2012)

NOTE: The table shows the data of each system as it was during the beginning of this work (August 2018). Since then, some systems have been further studied, with new observation data being generated. In this table, N_{obs} represents the number of observations that each system has, N_{fil} the number of different filters used in each photometric observation, and $Transspec$ represents whether a planet already has a published transmission spectrum in the literature or not (up to August 2018).

Table 2.2: System parameters

Parameter	Symbol (Unit)	WASP-69b Anderson et al. (2014)	HATS-6b Hartman et al. (2015a)
Orbital period	P (d)	3.8681382 ± 0.0000017	3.3252725 ± 0.0000021
Epoch of mid-transit	T_c (BJD, UTC)	2455748.83344 ± 0.00018	2456643.740580 ± 0.000084
Transit duration	T_{14} (d)	0.0929 ± 0.0012	0.08504 ± 0.00045
Transit ingress/egress duration	$T_{12} = T_{34}$ (d)	0.0192 ± 0.0014	0.01545 ± 0.00039
Transit depth	$\Delta F = R_p^2/R_*^2$	0.01786 ± 0.00042	0.03232 ± 0.00028
Impact parameter	b	0.686 ± 0.023	$0.427^{+0.020}_{-0.021}$
Orbital inclination	i (°)	86.71 ± 0.20	88.210 ± 0.084
Eccentricity	e	0 (adopted) (<0.10 at 2σ)	0 (fixed)
Stellar mass	M_* ($M_\odot$)	0.826 ± 0.029	$0.574^{+0.020}_{-0.027}$
Stellar radius	R_* ($R_\odot$)	0.813 ± 0.028	0.570 ± 0.011
Stellar surface gravity	$\log g_*$ (cgs)	4.535 ± 0.023	4.683 ± 0.010
Stellar effective temperature	T_{eff} (K)	4715 ± 50	3724 ± 18
Stellar metallicity	[Fe/H] (dex)	0.144 ± 0.077	0.200 ± 0.091
Planetary mass	M_p (M_J)	0.260 ± 0.017	0.319 ± 0.070
Planetary radius	R_p (R_J)	0.813 ± 0.028	0.998 ± 0.019
Planetary surface gravity	$\log g_p$ (cgs)	2.726 ± 0.046	2.90 ± 0.12
Planetary density	ρ_p (ρ_J)	0.219 ± 0.031	0.399 ± 0.089
Orbital major semi-axis	a (AU)	0.04525 ± 0.00053	$0.03623^{+0.00042}_{-0.00057}$
Planetary equilibrium temperature	T_{eq} (K)	963 ± 18	712.8 ± 5.1

Chapter 3

Observations

In this chapter, we present the reader the details of the telescopes and instruments used in the observation of our sample of transiting planets, as well as relevant information related to each of the transit observations obtained and analyzed in this work. In the first section of this chapter, we present the telescope, camera and observations of the WASP-69 system used for this thesis. In the second section, we explain the telescope, camera and observations gathered for the HATS-6 system. Only for these two systems, we acquired new data from transit observations. The newly collected data is presented in this chapter, while details of the data gathered from the literature is described in Chapter 2.

The telescopes used for the observations are located in two different astronomical observatories. One observatory is the Estación Astrofísica de Bosque Alegre (EABA), and the second one is Complejo Astronómico El Leoncito (CASLEO), both of them located in Argentina. In Table 3.1, we summarize the characteristics of all EABA and CASLEO cameras used. In Table 3.2, we present the log of the observations made for this work, while in Table 3.3 we give a brief summary of the number of calibration images taken for each transit observation.

Table 3.1: Telescopes and instruments used for the transit observations

Site	Telescope	Camera	Pixel Array Size	Pixel Size	Pixel Scale	FoV	Gain	Readout Noise	Dark Current
–	–	–	–	μm	arcsec/pixel	arcmin	e^-/ADU	e^-	e^-/pixel/hr
EABA	1.54-m	Apogee Alta F16M	4096×4096	9	0.25	16.8×16.8	1.45	22	72
CASLEO	2.15-m	Roper Scientific	2048×2048	13.5	0.45	9	2.18	3.14	< 1

Table 3.2: Log of the observed systems with Saturn-type planets

System	Date	Site	Telescope	Camera	Filter	Binning	Exposure-Time (s)	N_{obs}
WASP-69	2018-09-01	EABA	1.54-m	F16M	B	2×2	50	209
HATS-6	2016-01-10	CASLEO	2.15-m	Roper	R	5×5	10	650

Note: The date given corresponds to the start of the transit and N_{obs} is the number of useful exposures taken.

Table 3.3: Number of calibration frames generated per observation

System	Bias	Dark	Sky Flat	Dome Flat
WASP-69	10	8	0	10
HATS-6	10	0	10	10

3.1 Observation of WASP-69

EABA operates several telescopes of different sizes. The telescope used for this work is a Newtonian telescope with a diameter of 1.54-m, a focal length of 7.48-m and a focal ratio of f/4.9. In Figure 3.1, we show both the

[1]EABA images taken from https://oac.unc.edu.ar/files/bosque5.jpg and https://oac.unc.edu.ar/files/100_0827.jpg respectively.

Figure 3.1: Left: Image of the EABA telescope dome[1]. Right: Image of the 1.54-m telescope.

telescope dome and 1.54-m telescope of the Bosque Alegre observatory (31° 35′ 54″ S, 64° 32′ 58″ W), located 1350-m above sea level. EABA is equipped with a set of Johnson UBVRI filters and a pair of cameras. The camera used in this work is an Apogee Alta F16M with an array size of 4096×4096 pixels, a pixel size of 9μm, a pixel scale of 0.25 arcsec/pixel, a FoV of 16.8×16.8 arcmin^2, a gain of 1.45 e^-/ADU and a readout noise of 22 e^- (gain and readout noise concepts are explained in Section 4.1).

For this system, we obtained one new transit observation the night of the 1st of September 2018. It was done with the EABA 1.54-m telescope and using the Apogee Alta F16M camera. The transit of the planet was observed by Emiliano Jofré. The transit of the planet was observed with a Johnson B filter (central wavelength of 431.765 nm). The total of the transit was observed, i.e., all four contact points are visible (Figure 1.1) in the resulting light curve (for information on transit models, see Section 1.2). During the night of observation, the atmospheric conditions were not photometric, as the sky was partially cloudy. A 2-pixel binning of the images in both x and y directions was performed for the observation. Calibration images (bias, dark and dome flats) were also taken and are shown in Table 3.3. Details on calibration images and data reduction procedure are shown in Section 4.1.

3.2 Observation of HATS-6

Figure 3.2: Left: Image of the 2.15-m telescope dome at CASLEO. Right: Image of the 2.15-m telescope[2].

CASLEO is an astronomical center (31° 47′ 54.7″ S, 69° 17′ 44.1″ W) located 2552-m above sea level. The telescope used in this work is the Jorge Sahade telescope, a Ritchey-Chrétien telescope with a primary mirror of 2.15-m, a focal length of 5.58-m and a focal ratio of f/8.485. The transit of the planet was observed by

[2]CASLEO images taken from https://www.conicet.gov.ar/wp-content/uploads/Telescopio-CASLEO-web.jpg and https://casleo.conicet.gov.ar/wp-content/uploads/sites/42/2018/05/casleo05-768x505.jpg respectively.

Romina Petrucci. Both the telescope dome and the 2.15-m telescope can be seen in Figure 3.2. CASLEO also has available a set of Johnson UBVRI filters. The telescope uses a Roper Scientific camera with an array size of 2048×2048, a pixel size of 13.5 μm, a pixel scale of 0.45 arcsec/pixel, a circular FoV of 9 arcmin in diameter, a gain of 2.18 e^-/ADU and a readout noise of 3.14 e^- when equipped with a focal reducer, which we used during the transit observation of HATS-6 given that it increases the FoV of the camera and, hence, the number of stars present in the field of the images.

We obtained a new transit observation on the night of the 10th of January 2016. This transit was observed with the 2.15-m telescope located at CASLEO using the Roper Scientific camera. A Johnson R filter (central wavelength of 639.636 nm) was used for the observation. This time, only half of the transit was observed, with only the third and fourth contacts points observed. This was due to time restrictions given for the night of observation with HATS-6. Atmospheric conditions during the observation night were photometric. A 5-pixel binning of the images in both x and y directions was performed for the observation. Again, calibration images (bias, sky flats and dome flats) were acquired(see Table 3.3). Given that dark current is not significant in the Roper Scientific camera used, no dark frames were generated for this transit observation.

Chapter 4

Methodology

4.1 Data Reduction

The process of data reduction is the correction of atmospheric and instrumental effects created by observing any object with a charged-coupled device (CCD), regardless of the type of image taken (spectroscopic or photometric). This step must be done before we can perform any type of analysis on our data, because the raw images that are obtained usually contain noise from different sources that prevents the analysis of data contained within the images. This section is designed to explain concepts needed to familiarize the reader with some properties of CCDs, such as noise sources and how to correct them or at least minimize their influence when using the CCD for data gathering. At the same time that these concepts are explained, we describe the practical work done by us and the process of data reduction that followed, which allowed us to obtain the transit light curves from our sample of Saturn-type planets.

Before we start, it is convenient that we provide a brief explanation of what a CCD actually is. Basically, a charged-couple device is a type of integrated circuit built onto a surface made of silicon which forms light sensitive units commonly known as pixels. Through the photoelectric effect, incoming photons that strike the surface of the silicon generate an electric charge of free electrons. Then, the electronics within the CCD measure this charge value and turn it into a digital output that represents the light pattern illuminating over the CCD. A commonly used analogy ever since Janesick & Blouke (1987) is that each pixel works as a sort of water bucket that collects rainwater (photons). All these buckets are exposed to the same amount of time and rain, with each one collecting a different amount of rainwater that can then be measured one at a time and used to create a two-dimensional visualization of the water distribution within the buckets.

It is crucial that the reader understands the idea that all electrons behave in the exact same way and thus, are indistinguishable from one another regardless of their origin. So once a pixel in a CCD collects charge generated by the electrons, it is not longer possible to determine the exact origin of the electron that created said charge. If this electric charge accumulated by the pixel originates from electrons caused by noise coming from within the electronics or by incoming photons from space is something that cannot be answered once the charge contained in each pixel is read (when the physical charge is translated into digital counts).

The first of source of noise one has to understand is readout noise, which can be defined as the number of electrons introduced per pixel into the digital signal when the readout of the CCD occurs (Howell 2006). This readout noise is made of two different components. First, is the noise created when converting from an analogue signal to a digital value. Analogue-to-Digital (A/D) circuits and on-chip amplifiers tend to produce a distribution of possible values that are centered around a mean value. However, one must be careful as this does not necessarily mean that said distribution is Gaussian (Merline & Howell 1995). So even if the same pixel with the same amount of charge is read more than once, the final value may not be the same. The second component is the noise created by the electronic components of the CCD itself that introduces electrons in the readout process and produces additional fluctuations in the output. These two noise sources add up to generate an uncertainty in the output counts given by each pixel every time a readout is performed. The 1σ level of this uncertainty is called readout noise and it basically depends on the electronic properties of the on-chip output amplifier and the output electronics (Djorgovski 1984).

Some factors that may contribute to the readout noise level include the temperature, sensitivity, physical size of the on-chip amplifier and the building of the integrated circuit of the amplifier (Howell 2006). Whenever a

CCD creates a new output image, there is noise that is added into every pixel every time the pixel array is readout. For example, a readout noise of 10 electrons should on average contribute to 10 extra electrons of charge in every pixel during the readout. The readout noise value of the CCDs contained within the cameras used in this work are shown in Table 3.1.

Next, we shall explain what the gain of a CCD is. The gain is a value given by the CCD electronics and it basically represents how the amount of charge collected in each pixel will be assigned to a digital number in the output image (Howell 2006). The unit used to represent the gain of a CCD is given as electrons/Analogue-to-Digital Unit (e^-/ADU). Same as with the readout noise, the gain values of the CCDs used in this work can be seen in Table 3.1.

The first step toward the study of our object of interest is the acquisition of its astronomical observations with a CCD, what we call the science images. The exposure time for WASP-69 and HATS-6 images was 50 and 10 seconds, respectively. This time is dependent on the magnitude of the star, transit depth of the planet, conditions on the night of observation and optimization of the stars scintillation. In each of the images obtained the pixels will receive additional counts to that of the object of interest, created by electrons coming from the readout noise, dark current (explained further ahead) and even electrons generated by the background sky, all of which adds to the overall noise contained within each image. A more detailed explanation on the exact nature of these noise sources is made below along with the steps performed to correct them. A nonuniform response is also present in the CCD array from each of the pixels, that needs to be corrected called flat field calibration, such as the image shown in Figure 4.1. This is why at the center of any CCD image reduction process there is a basic set of frames used as the main tools for the calibration and reduction steps.

Each of these frames has the purpose of calibrating the science images from the undesired contributions previously mentioned that only adds noise to each image. What the data reduction process does, is that it allows for a minimization in the levels of noise in the resulting images, allowing the astronomical object to be analyzed. As mentioned in Section 3, we made one new transit observation for WASP-69 and HATS-6, with the rest of the transit light curves used in this work being acquired from several authors in the literature.

The new observations of WASP-69 and HATS-6 were reduced using the Image Reduction and Analysis Facility (IRAF) software. IRAF is a general purpose software system that allows for the reduction and study of astronomical data. It was written and supported by the National Optical Astronomy Observatories (NOAO) in Tuczon, Arizona. The reasons for working with IRAF is that it includes programs for general image processing, graphics applications and programs that enable the user to reduce and analyze optical astronomy data using the NOAO package. The first step of what we did on our data reduction process is loading the necessary packages from IRAF. These include the main NOAO package, which includes the IMRED package (used for image reduction), the CCDRED package (that stands for CCD generic reductions) and the ASTUTIL package that contains the tools needed to compute airmass, dates, convert coordinates, etc.

Once the packages are loaded, two custom programs called CORHEADER and CALIBRA are called into IRAF as tasks (Petrucci et al. 2020). Both of these programs used in the IRAF environment automatize the data reduction process. What CORHEADER does is the edition to the headers of all calibration and science images. The header of an image is a section of the data (usually found at the beginning of the file) that contains information about the image, such as the number of pixels, array size, date of creation, author, etc. CORHEADER gathers as input parameters from the user: the name of the object, its right ascension, the declination, the epoch, the name of the observatory and the filter of the observation. All of these parameters are added into the header data of each image. The CALIBRA program is somewhat more elaborate, as it is specifically designed to perform the entirety of the data reduction process with data coming from the EABA and CASLEO instruments, both described in Chapter 3. It should be noted that CALIBRA automatically runs the CORHEADER program by itself as a sort of sub-program, so it is not necessary for the user to run both programs. For CALIBRA to run, one must input all the science images, calibration frames, the name of the object, the name of the observatory and the filter used during the transit observation. Following this, CALIBRA will ask for the specific EABA or CASLEO CCD used during the transit observation, so as to register its gain and readout noise accordingly. The values used in this work are shown in Table 3.1. Then, it will proceed to make sure that the bias, dark and flat calibration frames are present in the same directory as the science images (otherwise some warnings may be displayed) and convert all images (science and calibration alike) to a .FITS format if they are not already and begin the data reduction process.

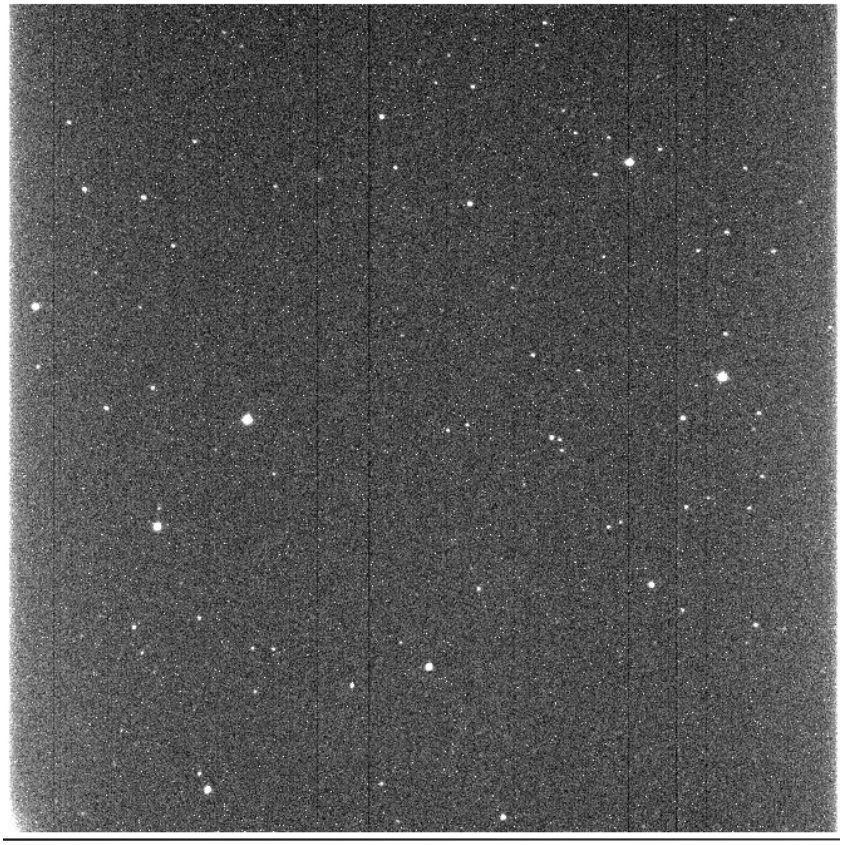

Figure 4.1: Example of a raw science image taken from a CCD. The generated image contains noise from several sources and pixel-to-pixel variations that must be corrected from the image in order to perform a proper analysis. This image corresponds to an observation of WASP-69 with the 17' x 17' CCD present at the EABA site.

4.1.1 Bias level calibration

So what exactly is the bias level of a CCD and how can it be corrected from our images? It is a calibration measurement done to estimate the value produced by an empty pixel (one with zero collected electrons) within a CCD. When the value of an empty pixel is readout and passes through A/D conversion, the result is a mean value with a distribution centered around zero (Howell 2006). As one can imagine, this means that pixels may end up having a negative value, which does not make sense at all, as there is no such thing as a negative pixel. In order to counter this effect in the output image, CCD electronics commonly provide a positive offset value for each image obtained. This offset value, becomes the true mean zero level of the CCD bias level. It should be noted that variations in the mean zero level of a CCD are plausible, usually over a period of months or even years, affecting the readout electronics of the CCD (Howell 2006). To calibrate CCD images for bias noise level the two most used calibration processes are the usage of overscan regions generated in all science frames or correction via bias frames. For this work, we used the bias frames calibration method using the frames gathered on both observation nights for WASP-69 and HATS-6.

To create bias frames a CCD image is taken with a total exposure time of zero seconds and without any kind of light exposure i.e., with the shutter closed, during which one simply reads the CCD. This means that bias frames give the readout noise of the unexposed CCD pixels through the on-chip electronics and A/D converter, producing a two-dimensional bias image as output that can be displayed on a computer like the bias frame shown in Figure 4.2. Bias frames represent two-dimensional structures that describe the CCD bias level. If a structure is found in the bias frames it is possible to extract the mean bias level value from all pixels of the science frames, or to remove the two-dimensional bias pattern by subtracting the bias image from all the dark, flat and science frames in a pixel-by-pixel subtraction. This second approach is basically how the bias calibration done in this work functions. It is recommended that several of these frames be made, because pixel values differ slightly from the real bias level due to the readout noise and variations found within the electronics, so a statistical sampling of several bias frames (preferably more than 10) has to be done, to diminish the contribution of these

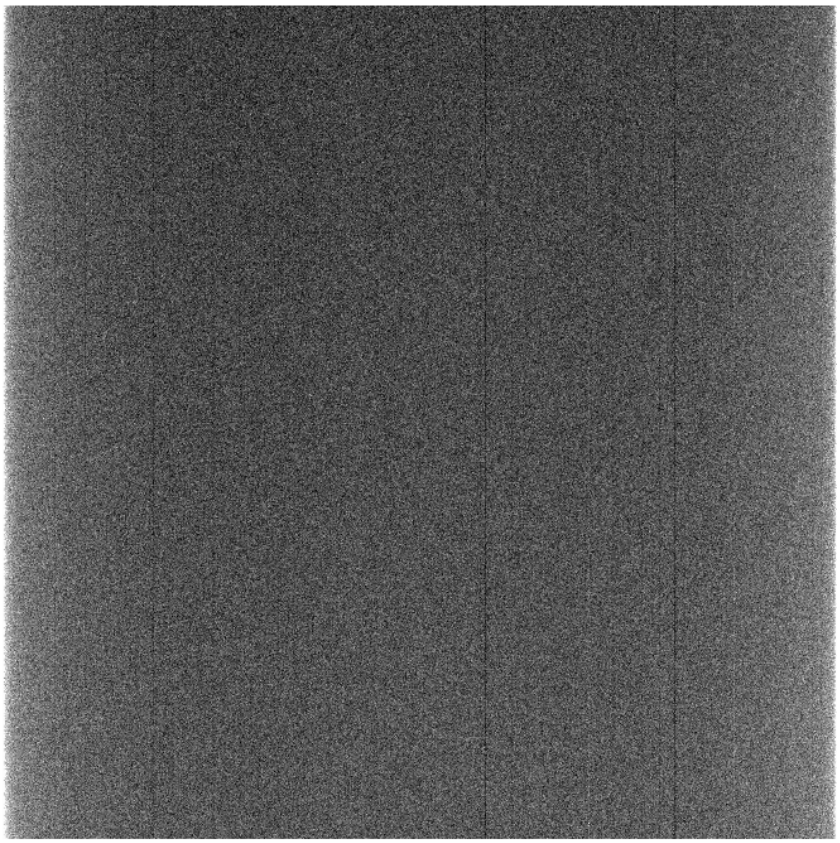

Figure 4.2: In this figure we show an example of how a bias frame used to calibrated for bias level noise looks like. Several of these frames are made and averaged to produce a master frame that will be subtracted from the other images. This bias frame was created from the same observation night used for WASP-69.

variations. The number of bias frames generated for each of our transit observations is shown in Table 3.3, with all the generated bias frames from both transit observations being used in the process. In Figures 4.3 and 4.4 it is shown the histograms of both the master bias frames generated for each of WASP-69 and HATS-6 transit observations. These are the frames used to calibrate all the dark, flat and science frames from bias noise level. If the histogram of an averaged bias frame, were to show a Gaussian distribution, then the mean level of this distribution would be the bias level offset for the CCD; with the width of the distribution being related to the readout noise (Mortara & Fowler 1981) and gain of the CCD by the expression

$$\sigma_{ADU} = \frac{Read\,noise}{Gain},$$

where σ is the width of the distribution in full width at half maximum units (FWHM). The FWHM[1] is a parameter used to describe the width of a function between the distance at which the curve is half of the maximum of its value.

Returning to the CALIBRA program, it now calls the function IMSTATISTICS[2]. This function allows the user to compute and print image pixel statistics for all images specified, given a set of initial input parameters. These initial parameters and the values used for this part of the calibration work are: the minimum good pixel value limit (**lower** = **INDEF**), the maximum good pixel value limit (**upper** = **INDEF**), the maximum number of iterative clipping cycles (**nclip** = **3**), the low side clipping factor in sigma (**lsigma** = **3**), the high side clipping factor in sigma (**usigma** = **3**) and the width of the histogram bins used for computing the midpoint (estimate of the median) and the mode (**binwidt** = **0.1**). The statistical quantities printed as output are: the image name, the number of pixels used to do the statistics (**npix**), the mean of the pixel distribution (**mean**), the standard deviation of the pixel distribution (**stddev**), the minimum pixel value (**min**) and maximum pixel value (**max**).

[1]For more information on FWHM, consider checking the following site: https://mathworld.wolfram.com/FullWidthatHalfMaximum.html

[2]For more details on IMSTATISTICS consult the following reference page: https://iraf.net/irafhelp.php?val=imstatistics&help=Help+Page

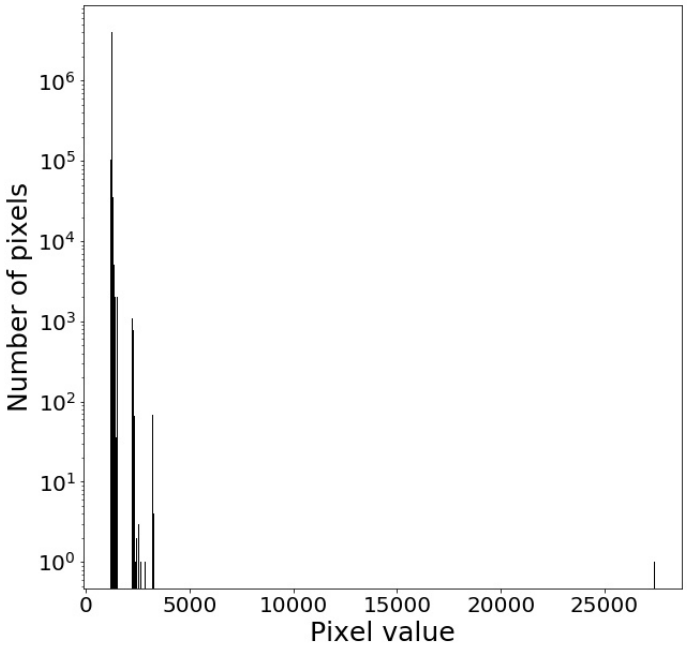

Figure 4.3: Histogram of the bias master frame for the WASP-69 transit observation. Here the histogram shows the pixel value reported by each pixel against the total number of pixel in the bias frame. Almost all pixels are grouped together around three central values, all of which have a value below 5000. The pixels with a count number greater than 25000 correspond to a column of hot pixels that exists within the frame.

This step is done by CALIBRA to gathered statistical information from all the bias frames that is used to assemble an averaged frame that will serve as a master bias frame and applied to the dark, flat and science frames for bias level calibration. All the bias frames taken for each transit observation are used to create the master frames. For the assembling of this averaged master frame it is necessary to call another function, IMCOMBINE[3]. As the name implies, this function manages to combine several images using various algorithms that the user can select. The input parameters needed for IMCOMBINE and the values used for the bias frames combination are: a list of frames to combine, the type of combining operation to perform (**combine** = **average**), the number of low and high pixels to be rejected by the minmax algorithm (**nlow** = **3**, **nhigh** = **3**), low and high sigma clipping factors used by the algorithm (**lsigma** = **1**, **hsigma** = **1**), CCD readout noise (**rlec**) and CCD gain (**gan**).

Once the master bias has been generated, CALIBRA proceeds to calibrate the rest of the dark, flat and science images from bias level noise by subtracting from them the master bias frame and creating a new set of intermediate dark, flat and science images that have been corrected from bias level. These new dark and flat frames will be used in a similar process to correct the new science images for dark current noise and flat field variation (explained in the following subsections). This concludes the part of CALIBRA where it corrects for bias level noise, and now it proceeds to apply dark current noise calibration.

4.1.2 Dark current calibration

The next source of noise that needs to be considered is thermal noise caused by a phenomenon called dark current. Any object at a temperature above absolute zero will always contain a certain amount of thermal noise within. The silicon atoms that compose a CCD present thermal perturbations that cause some electrons to become free from the silicon valence band and get collected by the potential well of each pixel (Howell 2006). When the pixels are readout, a signal is received as output by adding up the all electrons, however electrons are indistinguishable from one another, regardless of their origin, so electrons collected from dark current contribute

[3]For more information on IMCOBINE consult the following page: https://iraf.net/irafhelp.php?val=imcombine&help=Help+Page

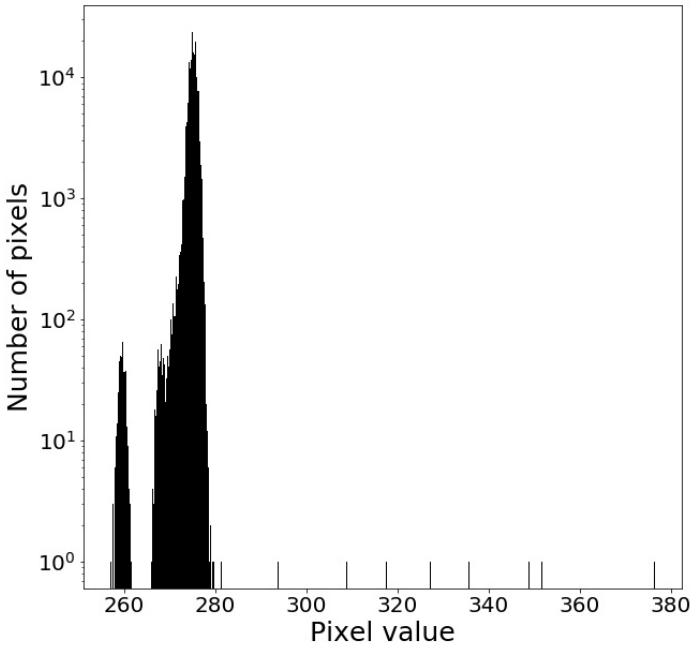

Figure 4.4: Histogram of the bias master frame for the HATS-6 transit observation. In this case, most of the pixels are distributed around two central values below 280. The remaining pixels in the frame are hot pixels that have values greater than 280 and up to 380.

equally to those created by astronomical photons in the output signal.

Thermal generated electrons can be described as a function of temperature; with the dark current of a CCD usually expressed in number of thermal electrons generated per second per pixel. To give the reader an idea of the importance of the contribution by dark current electrons to a CCD image, at room temperature this value is approximately 2.5x10^4 electrons/pixel/second (Howell 2006). For a properly cooled CCD (usually using liquid nitrogen) this value drastically drops to a range between 2 to 0.04 electrons/pixel/second (Howell 2006). An example of the impact of dark current electrons is as follows: suppose a CCD that has a dark current value of 2 electrons/pixel/second, taking a 10 minute exposure frame would produce 1200 thermal electrons in every pixel that were not accounted for in the first place and are included in the output signal upon readout. The dark current values of the cameras used in this work are shown in Table 3.1. As previously mentioned, the additional charge generated by the dark current electrons cannot be differentiated from the charge obtained from space-collected photons which generate electrons, and this naturally gives a limit to the minimum noise levels that a CCD can achieve. The effect of dark current noise can be removed from CCD frames via dark frame calibration.

Dark frames are taken with the shutter closed and for a certain amount of time, that usually is the same exposure time as the scientific images. In this work, the dark frames created for the WASP-69 and HATS-6 observation were done using the same exposure time as the science images. These dark frames will contain a bias level and dark current noise but zero electrons generated from space photons. An example of a dark frame is provided in Figure 4.5. Besides providing information about thermal noise in a CCD, these frames can also give information about bad pixels in the CCD and cosmic ray strikes at the site of observation. As stated in the previous subsection, the new dark frames that have been calibrated from bias level noise are used to correct the remaining flat and science frames. Once again CALIBRA makes use of IMSTATISTICS to gather information on the dark frames. The new values of the input parameters are: **lower** = **INDEF**, **upper** = **INDEF**, **nclip** = **2**, **lsigma** = **3**, **usigma** = **3**, **binwidt=0.1**. For the IMCOMBINE function the input parameters are now: **combine** = **median**, **nlow** = **3**, **nhigh** = **3**, **lsigma** = **3**, **hsigma** = **3**, **rlec** and **gan**. Same as with the bias calibration, CALIBRA creates a master dark frame and uses it on the flat frames and science images by subtracting it from them. These new flat frames and science images have been corrected for bias level and dark current noise and are ready to enter the next step of the data reduction process.

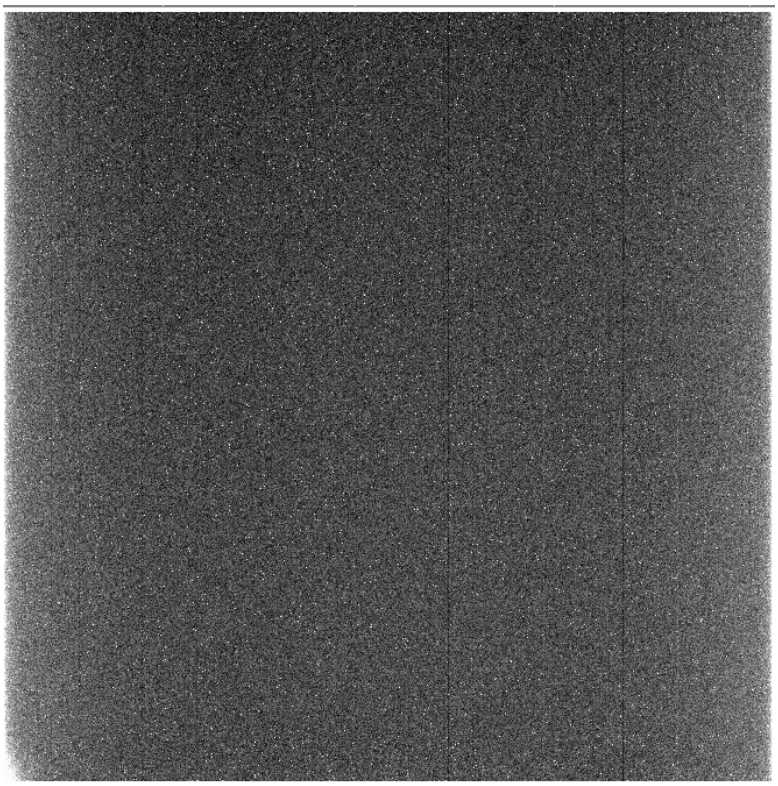

Figure 4.5: Dark frame taken from the WASP-69 transit observation. All dark frames are corrected from bias level noise and combined into a master frame. This frame is then used to calibrate the flat frames and science images from dark current noise. The frame shown here has not been calibrated for bias level noise yet.

4.1.3 Flat field calibration

We now discuss the idea of flat field on CCDs, what is it and how must it be corrected out of science images. Within every CCD, each pixel has a certain gain or quantum efficiency value (QE). This QE value represents the number of electrons produced in a pixel by every incoming photo that impacts the CCD, so the QE can be seen as the percentage of light detected by the CCD. Even for pixels in the same array, this QE value differs slightly from one pixel to another. This kind of variation makes it necessary to flatten the response of all pixels to the radiation received from observations. In order to correct the pixel array from this variation, flat field frames are used to calibrate the CCD images (Howell 2006). This type of frame is made by exposing all pixels to a uniform illuminating source that has the same spectral response to that of the science images. This means generating a frame that is both spatially and spectrally flat. If one can achieve this then all that remains is dividing the science images by the flat frame and with that the calibration of pixel-to-pixel variations for CCD images is done. Although flat frames also help to compensate the images for any dust accumulation that may occur.

There are a couple of methods used to create a flat field image with CCDs. The first method consists of illuminating a flat screen located inside the telescope dome with a light source (usually a hot filament quartz lamp) and taking frames of this screen. The illuminated interior is several times brighter than the night sky so the exposures taken must be short to avoid saturating the CCD. The second method commonly used relies on the same idea of taking exposures with the telescope but using the dawn or dusk sky instead (Howell 2006). Flat frames obtained from the first method are called dome flats and sky flats is the name for those obtained from the dawn or dusk sky. The number of flat frames taken for each transit observation are shown in Table 3.3. For the WASP-69 transit observation (shown in Figure 4.7) we made use of dome flats, while for the HATS-6 one, both sky and dome flats were taken and used to obtained two different light curves. One using the sky flat as calibration and the other with the dome flats and choosing the light curve with the least dispersion.

For a flat field image to be useful it is necessary to use a light source brighter than the resulting astronomical image studied because a bright light source results in an image with high signal-to-noise ratio (why this concept is relevant to CCD imaging is discussed in Subsection 4.2). Finally it should be added that pixels respond in different ways to different colors of light, and as such, flat field frames need to be obtained through the same

filter as the one used in the observation.

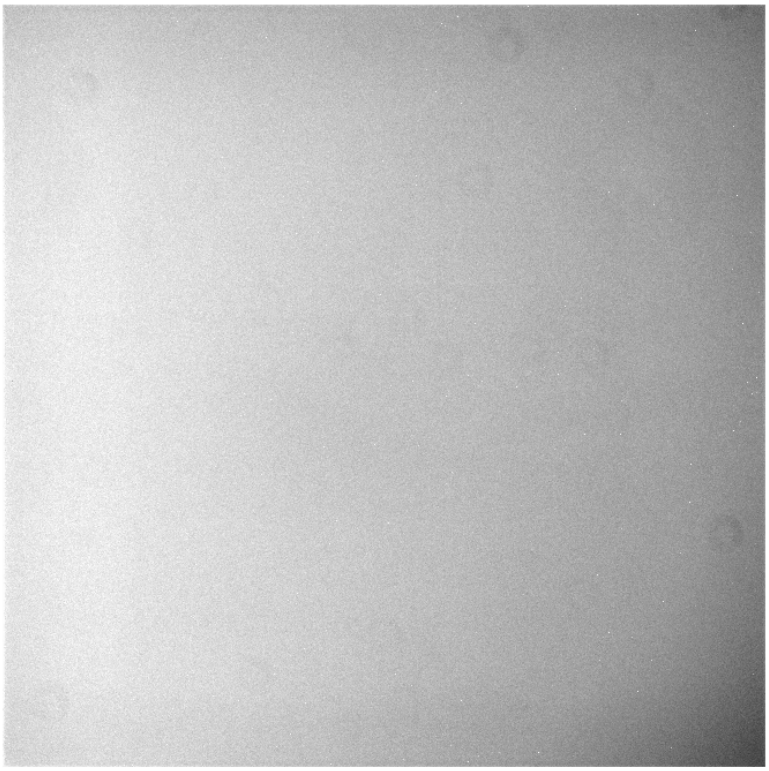

Figure 4.6: Raw flat-field frame used in the data reduction process. This image has yet to be corrected for bias level and dark current noise. Once all the flat images are calibrated and the master image is created it is applied to all the science images to correct them of any pixel-to-pixel variations that may be present in the CCD. This particular image was also taken from the WASP-69 observation night using a Johnson B filter.

When working on flat field frames there are two major concerns associated with the resulting frames. First, the needed uniform illumination of every CCD pixel, or what was previously called spatially flat, must be quite even (about one part in a thousand) but in reality, this is extremely difficult to produce (Howell 2006). The second problem is that there is a wavelength dependency for QE variations in the pixels. Therefore, the flat field image obtained and all the object images that need calibration must have the exact same wavelength distribution over the band-pass of interest, in other words, be spectrally flat. Indeed is this a problem, as lamps and dawn/dusk skies are not similar at all in spectral shape (or color temperature) to the dark nighttime sky, where star and galaxy are observed. The result is that in most cases, obtaining a perfect flat field image is quite unlikely. Nevertheless this is not necessarily a constrain given that there are several fields of astronomy where obtaining a perfect flat field for all wavelengths is not required. Flat frames are needed for every type of filter used during observation. All the flat frames used in this work are generated using the dome flat frames procedure.

CALIBRA runs once again the IMSTATISTICS function with the following parameters: **lower** = **INDEF**, **upper** = **INDEF**, **nclip** = **2**, **lsigma** = **3**, **usigma** = **3**, **binwidt** = **0.1**, and the resulting data is used while calling IMCOMBINE to create the master flat frame with the input parameters being: **combine** = **average**, **nlow** = **2.5**, **nhigh** = **2.5**, **lsigma** = **3**, **hsigma** = **3**, CCD readout noise and gain. This final master flat frame is divided by all the science images. An example of a typical flat-field image can be seen in Figure 4.6. For a good flat field image to be made it is recommended that five to ten or even more flats be made in every filter. The number of flat frames produced for each transit observation are shown in Table 3.3.

4.1.4 Final step of the data reduction process

CALIBRA can perform the reduction steps even when one or two types of calibration frames are not present (if that is the case some warnings may appear). At the end, the new FITS images generated by the program in-between steps are deleted so the user remains with just the original calibration and science images plus a copy of new corrected science images.

With this done, we finally have all our science images calibrated from bias level noise, dark current noise and

flat field variations. An example of the final images created by the CALIBRA program can be seen in the Figure 4.7. It is with these new set of science images that we proceed to the next step of the process, where the goal is to measure the number of counts collected by the CCD from our object of interest using the aperture photometry method.

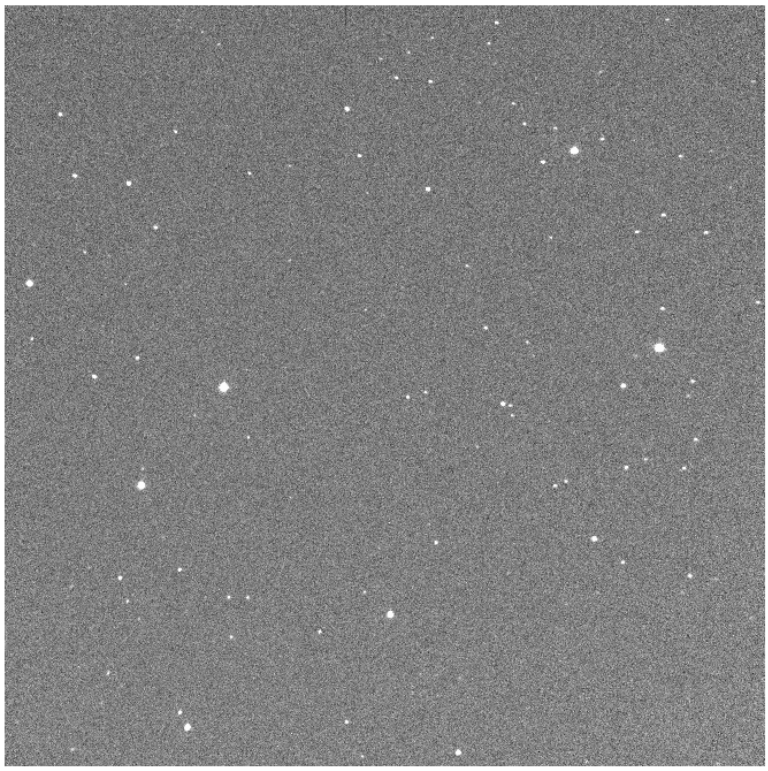

Figure 4.7: Science image that has been calibrated for bias level noise, dark current noise and pixel-to-pixel variation using flat-field images by the CALIBRA program. Once all the science images have been properly reduced we can proceed to the next step of the work done to obtain the transit light curves of a planet. The image shown here is the exact same one that we see in Figure 4.1 from the WASP-69 observation after the calibration was performed.

4.2 Photometry

Photometry the process of determining the amount and temporal nature of light emitted by an object as a function of wavelength (Howell 2006). In this section, we present the photometry of the data gathered from our own transit observations (described in Chapter 3). All the images used in this section have been reduced, i.e., they have been calibrated following the steps previously described in Section 4.1. The first part of this section describes the technique of aperture photometry and the process to measure the instrumental magnitude of every star in every image of our transit observations. The second part of this section explains the technique of differential photometry and how it is implemented to calculate the differential magnitudes to obtain the light curves of each transit.

4.2.1 Aperture Photometry

Aperture photometry is a technique that consist of adding up all the observed pixel counts within a specific radius centered around the source (Howell 2006). To measure the number of pixel counts that one object has, an aperture that begins on the x and y coordinates of the center of the star up to a radius r is used. Usually, the aperture shape is circular or in some cases square (the work done here makes use of a circular aperture). Obtaining the instrumental magnitude of the stellar object of interest is the main objective of the aperture photometry method, with the instrumental magnitude being the non-calibrated apparent magnitude, that is calculated for an astronomical object in an image. The instrumental magnitude depends on the number of counts that the object has within the aperture used, and it also gives information about the brightness of an astronomical object as seen from the Earth. For measuring the brightness of an object on a CCD frame, the photometry process can be summarized as follows: add up all the counts coming from pixels that collected light from the star, calculate the contribution of the background sky with nearby pixels and subtract the background sky contribution from the value found for the stellar object in order to obtain the total amount of light coming from the star (Da Costa 1992).

The value of this aperture radius r can be three times the FWHM of the star, as it has been shown by Merline & Howell (1995) that this value of r usually encircles almost all (but no 100%) of the flux coming from the star. This assertion can be seen in Figure 4.8. This is of importance, given that finding the aperture size that yields almost 100% of the object counts is needed for the aperture technique to work, otherwise one may end up with a wrong value of the instrumental magnitude. However, in the field of photometry, one must also focus on finding the maximum possible S/N ratio (see Section 4.1) of the object of interest, and not only its total count value. It should be mentioned, that there is a relation between the radius used for the aperture and the S/N ratio obtained (Howell 1989). Even if using three times the FWHM as aperture means collecting the entirety of the flux coming from the star, that does not necessarily mean it results in the maximum S/N ratio for the measurement (Howell 2006). For a maximum S/N ratio to be obtained, one must increase the total amount of stellar counts in the aperture, i.e., increase the number of stellar counts by increasing the radius of the aperture. However, this also means introducing more background sky counts into the aperture area that increase the error of the measurement. So, it becomes necessary to find the ideal balance between maximizing the S/N ratio and minimizing the noise introduced in the measurement (Da Costa 1992; Mighell 1999; Howell 2006). Again, finding the aperture size at which the S/N ratio is maximum for an object is important because it is also needed for the aperture photometry process that we explain ahead.

Identification of stars in the image field

Once the data is calibrated, we must identify our star of interest in the images. This is a rather simple but important step because, so far, we have no way of identifying any of the stars in the images, without a reference. For this, we made use of the Aladin Catalog[4]. Aladin is an interactive sky atlas developed at CDS, Strasbourg Observatory, France (Bonnarel et al. 2000; Boch & Fernique 2014), that allows the visualization of digitized astronomical images. By comparing existing images found in the Aladin Catalog with the stars in the field of our images, we are able to identify the stellar object of interest. Image resolution and the orientation of the frames are some aspects to consider when determining the star of interest.

The next step consists of selecting one reference image from all our science images. This reference image is chosen from the images taken during the same observation night. The selected image will be used to perform the initial analysis that leads to the actual aperture photometry process and as such, it is necessary for the reference image to have an overall good quality, meaning, the reference image should contain both the stellar

[4]The Aladin Catalog can be consulted in the following link: http://aladin.u-strasbg.fr/AladinLite/

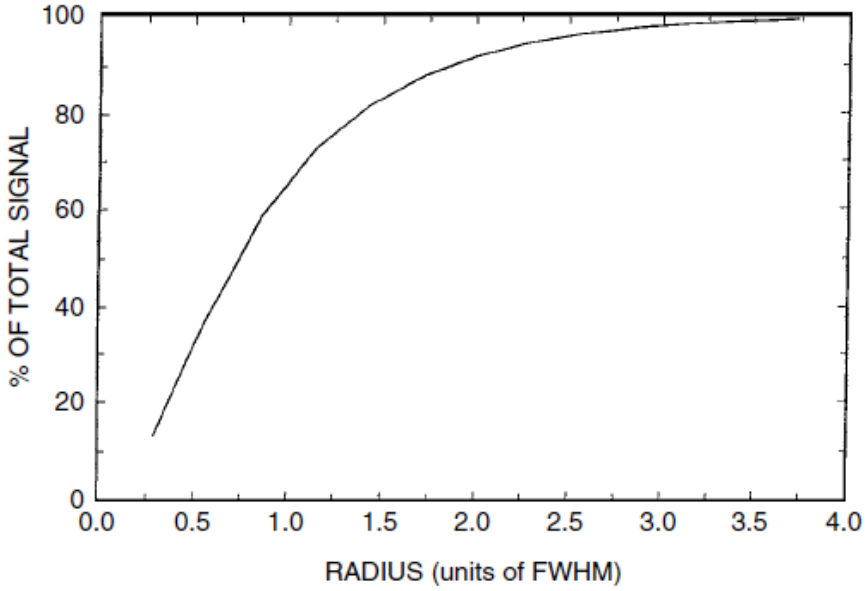

Figure 4.8: Figure of the total amount of counts (here % of total signal) gathered from a stellar object within a radius r in units of FWHM. It can be seen that when r is three times the FWHM, almost 100% of the signal coming from the stellar object is contained. This figure was taken from Howell (2006).

object of interest and other several potential comparison stars. Within the reference image, both the star of interest and the other stars in the field, should have well defined stellar profiles, i.e, no images containing stars with unclear or vague contours should be selected. Of all the images taken during the transit observation, it is recommended to select the reference image from those images generated through half of the transit observation. This is to account for potential stars at the fringes of the image that will serve as reference, coming in and out of the field of the images throughout the transit observation. This is due to the celestial tracking used by the telescopes (presented in Chapter 3) not being that good, with variations of up to 100 pixels per night in the x and y central coordinates of the star. This is why the center of the stars in the images move during the observation.

With a reference image selected, and the star of interest identified, we return to the IRAF software package. We employ the IMEXAMINE task to analyze our reference image. IMEXAMINE[5] provides us with several quick-look tools used for image examination and data analysis. The first step is, to obtain a rough estimation of the background sky value. The IMEXAMINE task contains the m command that can print statistical parameters centered around the image cursor that the user sees over the image. These parameters include: the number of pixels within the examined area, the mean number of counts, the median value of these counts, the standard deviation, and the minimum and maximum count value found. With this, we select ten regions of space on the reference image that do not appear to contain any objects whatsoever and calculate an average of the mean and standard deviation values given by IMEXAMINE. This averaged mean and standard deviation of the background sky value will be used to detect stellar objects in every image (how is explained in the following paragraphs). Another parameter that we wish to find is the FWHM of our star of interest. For this, we use the IMEXAMINE r command that displays radial profile plots for the stellar object flux, centered where the cursor is located. Once the figure is displayed, the FWHM is the last number appearing in the bottom part. In Figure 4.9 and Figure 4.10 we show the radial profile plots created by IMEXAMINE for the WASP-69 and HATS-6 stars, using the reference images selected during the WASP-69 and HATS-6 transit observations respectively.

Now, we make use of the IRAF/DAOPHOT package. Originally, DAOPHOT was an independent software package created to work with stellar photometry by Stetson (1987, 1990, 1992a). The IRAF/DAOPHOT package basically uses the algorithms of DAOPHOT, adapted to the IRAF environment. DAOPHOT is one of several packages contained within the digital stellar photometry package (DIGIPHOT) of IRAF, so we first load DIGIPHOT package and then DAOPHOT. Once both packages are loaded, we call the DAOFIND task.

[5]IMEXAMINE documentation can be found in the following page: http://iraf.noao.edu/cgi-bin/irafhelp?imexamine

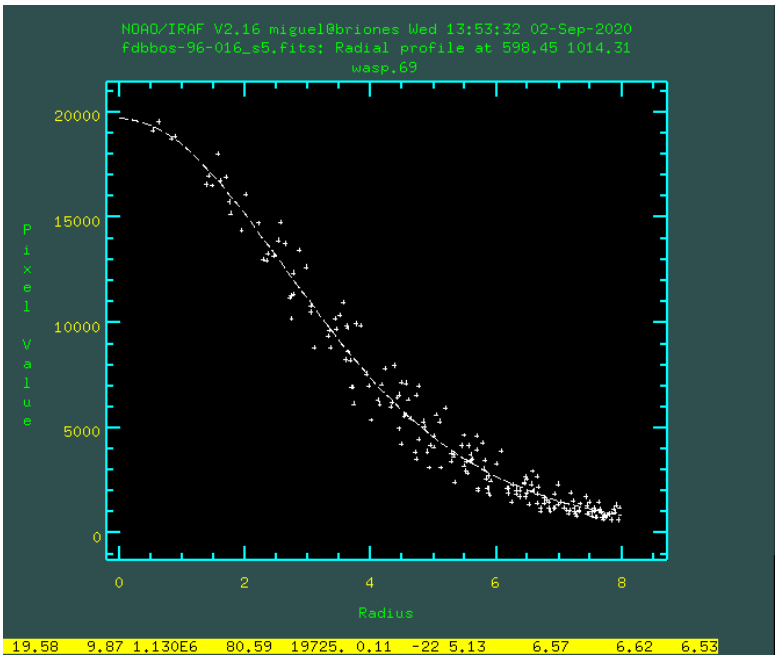

Figure 4.9: Radial profile plot of WASP-69 generated by IMEXAMINE. On the top of the image, the name of the reference file, the coordinates of the center and the object name can be seen. The horizontal axis is the plotting radius in pixels, while the vertical axis represents the summed pixel count value within the aperture. Here, the FWHM found by IMEXAMINE is 6.53 pixels (1.63 arcsec).

DAOFIND[6] works by searching point sources (stars) in an image, where said point sources must have peak intensities above a threshold set by the user (Davis 1994). We calculated this threshold as three times the averaged standard deviation of the background sky counts. After the point sources are identified, DAOFIND calculates an approximation to the center of the sources, and computes their magnitude and shape characteristics (sharpness and roundness of the object) (Davis 1994). This information is then stored by DAOFIND in an output file. We want DAOFIND to locate our stars of interest (WASP-69, HATS-6), plus any additional stars present in the field of the reference image that may serve as comparison stars. The results gathered by DAOFIND with the reference image will be used as a starting point for the detection of the same stars in the rest of the science images of the same observing night.

DAOFIND works by reading the parameters declared inside the task, plus two sets of algorithm parameters. These inputs are: the reference image, and the DATAPARS and FINDPARS algorithm parameters. Once DAOFIND is loaded, we input the name of the reference image. Then, we open and edit DATAPARS and FINDPARS. DATAPARS[7], is a group of parameters that control the data dependent parameters. Inside DATAPARS, the edited parameters are: the FWHM value we previously obtained from the radial profile plots (**fwhmpsf**) in pixel units that optimizes the star searching algorithm, the averaged standard deviation previously obtained of the sky background for a region absent of stars in the image (**sigma**), the minimum good data value given by the averaged background count value minus three times the averaged standard deviation (**datamin**), the maximum good data value given by the CCD saturation level (**datamax**), where **datamin** and **datamax** are used by the algorithm to remove any bad data present; the CCD readout noise value (**readnoi**), the CCD gain value (**epadu**), the exposure time image header keyword (**exposur**=**CEXPTIME**), the airmass image header keyword (**airmass**=**airmass**), the filter image header keyword (**filter**=**FILTERS**) and the time of observation image header keyword (**obstime**=**UTMIDDLE**). The rest of the parameters inside DATAPARS not mentioned here are left with their default values.

The second group of parameters is FINDPARS, a subset that edits the star selection parameters. Inside FINDPARS the only edited parameter is: the object detection threshold above local background value (**thresho**) we previously mentioned. In the case of WASP-69, this value was 42.50 counts, and for HATS-6, 13.95 counts (see Table 4.1). This **thresho** parameter controls the amount of objects detected. If the number of this parameter is too small, then, many objects will be counted as stars and if the number is too big, only the

[6]For more information on DAOFIND please consult the following site: https://iraf.net/irafhelp.php?val=daofind
[7]DATAPARS documentation found in: https://iraf.net/irafhelp.php?val=daophot.datapars&help=Help+Page

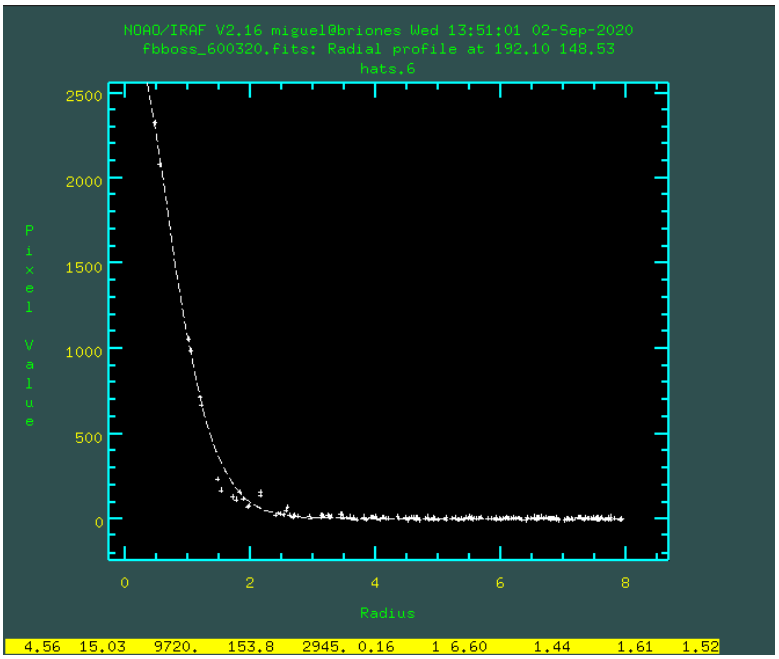

Figure 4.10: Radial profile plot of HATS-6. The name of the reference image, the coordinates and object name are displayed on the top. The radius in pixels is shown in the horizontal axis against the summed pixel count value of the star in the vertical axis. In HATS-6, the FWHM found is 1.52 pixels (0.68 arcsec).

Table 4.1: DAOFIND parameter values used for the WASP-69 and HATS-6 images.

DAOFIND parameter	WASP-69	HATS-6
fwhmpsf (pixels)	6.53	1.46
sigma	14.16	4.65
datamin (pixel counts)	33.45	136.62
datamax (pixel counts)	60000	60000
readnoi (e^-)	22	3.14
epadu (e^-/ADU)	1.45	2.18
thresho (pixel counts)	45.50	13.95

brightest stars will be accounted for. Again, those FINDPARS parameters not mentioned here are left with default values.

When running DAOFIND, it will ask us one final confirmation of the parameter values given, and once we do so, it will output a .COO file named after the reference image containing a brief summary of the input parameters given to DAOFIND, plus the number of stars detected, their x and y central coordinates, their magnitude and numerical identifier, among other pieces of information. We can check the results that DAOFIND outputs by running the TVMARK task and declaring as input the .COO file just created. TVMARK will show the central coordinates of the stars (denoted by a color point) and their identification numbers in the reference image. In Figure 4.11 and Figure 4.12, we show the results found by the DAOFIND task using the reference images selected for each of the transit observations. DAOFIND can run any number of times, changing the input parameters as needed, if the results are found to be unsatisfactory or mistaken, i.e., if DAOFIND founds too many or too few stellar objects, or if the program mistakenly "detects" artifacts in the images as stars.

Now, we take the DAOFIND .COO output file generated for the reference image and rename it as "refcoords". This file will serve as a reference file that contains the results given by DAOFIND. Next, we choose which reference stars we preserve in the image and which ones we remove. This is because, even if the stars have a count value above the input threshold and are properly detected and centered, sometimes they are too faint to serve in the rest of the photometric process or, as previously said, are in the fringes of the image. As the transit observation continues, these stars located at the edges of the image may disappear from the image field, making them inadequate as comparison stars in all the science images. We remove the stars that we do not want and renumber the rest of the stars in ascending order. This order is given by the identification number

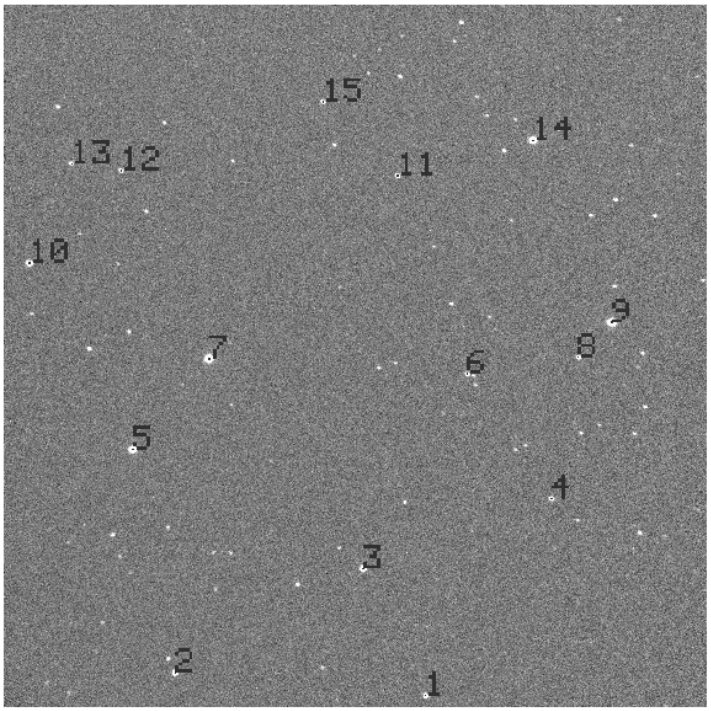

Figure 4.11: Reference image for the WASP-69 transit observation. Each number corresponds to one star detected by the DAOFIND task, with the center coordinates of each star shown as a black dot by the TVMARK task. For reference, WASP-69 is the star with the number 7 on it.

of each star. As preparation for the aperture photometry process, we create a file named "coords" with the coordinates in pixel units of the brightest stars in the field found by DAOFIND. It is recommended to choose at least three stars or more. We call the IMEXAMINE task once again, and call a command that creates a vector plot between two cursor points selected on the image. These two points must be at opposite positions and cross the star of interest by its center at a distance that falls outside the star contour. From this vector plot we must obtain two values necessary for the photometry process. The first one is the radius of the distance measured from the central maximum pixel value of the star to where the count values reach zero or almost zero. We name this value "radius1". The second value is basically the FWHM of the vector plot, called "radius2". Figures 4.13 and 4.14 show the vector plots produced by IMEXAMINE used in this work for the transit observations.

Measuring the background sky value and instrumental magnitude

Measuring the contribution of the background sky on a CCD frame is another step that needs to be done during the photometric analysis of the images. This background contribution value must be subtracted from the counts collected for the object of interest, before we measure the total flux. The background of the image contains photons coming from the sky, unresolved stars and galaxies, readout noise, etc (Howell 2006). We already explained how to account for both dark current and readout noise (see Section 4.1), so we assume that the main source of noise is the contribution of photons coming from both space and the atmosphere. A technique commonly used is to place an annulus (Figure 4.15) around the stellar object and find its mean counts per pixel (Howell 2006). This annulus is made of an inner and external radius, separated by a certain width. One method to estimate the background level with this annulus is to extract the value of all pixels within the annulus, obtain the total sum and divide by the number of pixels present inside the annulus, yielding an average value per pixel for the background level (Howell 2006). For a good statistical determination of the background level, the total number of pixels inside the annulus should be at least three times that of the star aperture (Merline & Howell 1995). The task of background determination is really important, as the quality of our S/N ratio for every star in the frame depends on it.

Once the center of the stars is found and the background level is known, it is possible to find the total counts from inside the star aperture. By using an aperture of radius r located in the x, y coordinates of the star center we can obtain the total count value S of all pixels within the area A ($=\pi r^2$) (Howell 2006). Naturally, this value includes all the counts from both the aperture star and background level. The background level

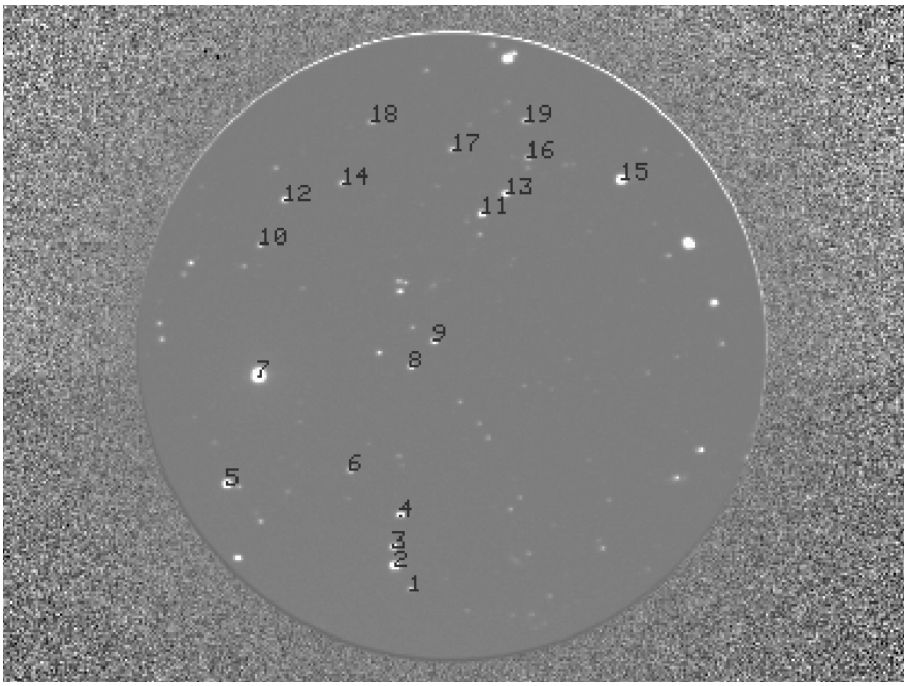

Figure 4.12: Reference image used for the HATS-6 transit observation. Same as with Figure 4.11, each number corresponds to one star detected by the DAOFIND task, with the center coordinates of each star shown as a black dot by the TVMARK task. HATS-6 is the star with the reference number 4.

B, can now be subtracted from the aperture count value. With this, we can calculate the intensity I, of the star as $I = S - n_{pix}\ \overline{B}$ where $\overline{B}$ is the mean value of the background and n_{pix} is the total number of pixels within A (Merline & Howell 1995; Howell 2006). Now, we calculate the instrumental magnitude using I with the expression:

$$m = -2.5log_{10}(I) + c$$

where I is the star intensity per unit time, i.e. flux. and c a constant (Da Costa 1992; Howell 2006).

Aperture corrections and the growth curves method

In this subsection, we explain what the growth curve method and aperture correction are, and how they are applied to our work. The Point-Spread-Function (PSF) is defined as the two-dimensional intensity distribution produced at the detector by the image of an unresolved point source (Da Costa 1992). For this work, we assume that the PSF shape is the same for all stars in the frame, regardless of their brightness and position (Da Costa 1992); an acceptable assumption given our observations. However, the intensity of the PSF can vary depending on the brightness of the star. For this reason, brighter stars will have PSF with a higher intensity than that of dimmer stars. To obtain the instrumental magnitude of each star, one must include as close to 100% of the stellar flux within the aperture. To include almost 100% of the stellar flux inside the aperture is similar to including almost all the PSF within the aperture. The aperture radius must be big enough to contain the majority of the counts coming from the star; however, for faint stars, bigger apertures include not only the stellar counts, but an even greater contribution from the background sky counts, thus, resulting in a wrong instrumental magnitude measurement for big apertures. An example of this can be seen in Figure 4.16, where the effects of steadily increasing the aperture size for both faint and bright stars is shown, and where the instrumental magnitude obtained for the faint star starts to diverge from the rest once the aperture selected becomes large enough. This problem can be solved by applying a correction known as aperture correction, which is the difference between the magnitudes obtained with a small and a large aperture in bright stars. The small aperture is that for which we obtain the maximum S/N ratio, and the large aperture is the one that contains almost 100% of the stellar flux. This correction is added to the measures done for faint stars with small aperture. This produces an effective large aperture measurement for said faint stars (Da Costa 1992). Here, the important part is to determine the appropriate size of the large aperture used. In order to achieve that, the growth curves method can be used (Howell 1989; Stetson 1990, 1992b). In Figure 4.16 we show an example of growth curves for five stars taken from a single CCD frame.

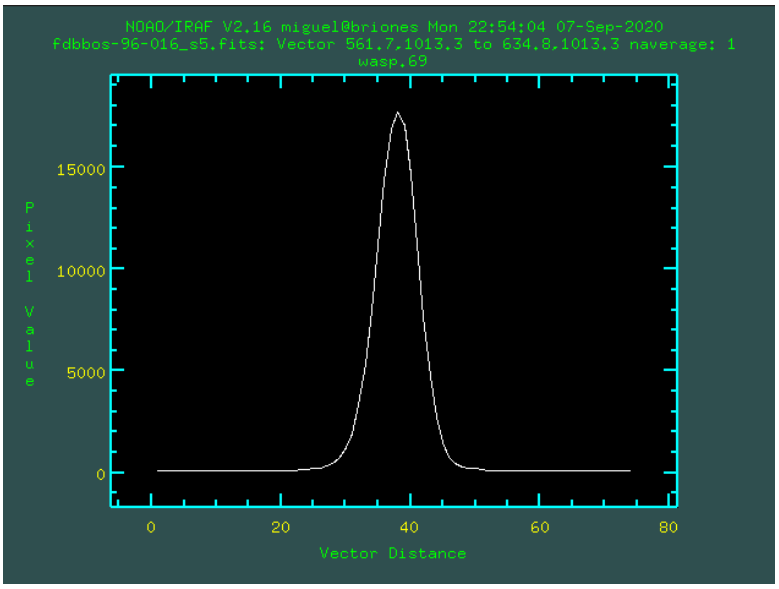

Figure 4.13: Vector plot of WASP-69 from the reference image. In the top part, the name of the file, the vector coordinates in pixel and object name are shown. The plot show on the horizontal axis the distance between two user selected points in the image, with the units in pixels. The vertical axis represents the pixel value of the pixels. For WASP-69 case, the radius1 value is 15 and radius2 is 10.

The growth curves measures as many bright stars as possible through several concentric apertures that increase in radius, and then calculate the magnitude differences between successive apertures for every star (Stetson 1990). The differences in magnitude are plotted as a function of radius, with the curve that connects these magnitudes being the average growth curve of the image. Then, the average magnitude differences between successive apertures are read from the curve and summed, starting from the outside and moving inward, to get cumulative corrections from each of the smaller apertures (Stetson 1990). For the brighter stars in the field, their growth curves generally need little or no correction in their aperture size, with this aperture usually being three times the FWHM (Howell 2006). Once the bigger aperture is found using the growth curve method for the bright stars, the differential magnitude is performed between the magnitude values from both the small and big apertures. With this, we obtain the aperture correction and add it to the instrumental magnitude calculated for all stars (both faint and bright) using the small aperture radius.

The FOTOMCAP process

In this next step of the photometric process, we make use of the FOTOMCAP code (Petrucci & Jofré 2016). FOTOMCAP is a quasi-automatic code written for IRAF and designed to calculate the instrumental magnitudes of stellar objects in the same field (Petrucci & Jofré 2016), using the aperture correction method presented by Howell (1989) and Stetson (1990) to obtain transit light curves. The input that FOTOMCAP needs is: all the calibrated science images, the CCD readout noise, the gain, the CCD saturation level, the primary mirror diameter of the telescope used in the observation, the elevation of the telescope above sea level and the reference image selected. The output will be a file containing the instrumental magnitudes for each star on every image, its respective errors, the Heliocentric Julian Date (HJD), the file name, the airmass, the star number, and the central coordinates of each star in pixel units.

The first part of the FOTOMCAP code is designed to find the centers of all the stars in every image given and calculate the shift in the positions of the stars (coordinates in pixel units) compared to the reference image. For this, FOTOMCAP makes use of the IMCENTROID task. IMCENTROID[8] works by measuring the X and Y coordinates of a set of stellar objects in a group of images. It also measures the mean X and Y distance shift between each image and the reference image. The stellar objects given as input are contained within the "coords" file that we previously created. For this reason, once we execute FOTOMCAP, it will ask for four parameters needed by the IMCENTROID task. These parameters are: the size in pixels of the box used for a rough estimation of the center of stellar objects (**bigbox**), the size in pixels of the box used for the final estimation

[8]For more information on IMCENTROID consult the following page: https://iraf.net/irafhelp.php?val=imcentroid&help=Help+Page

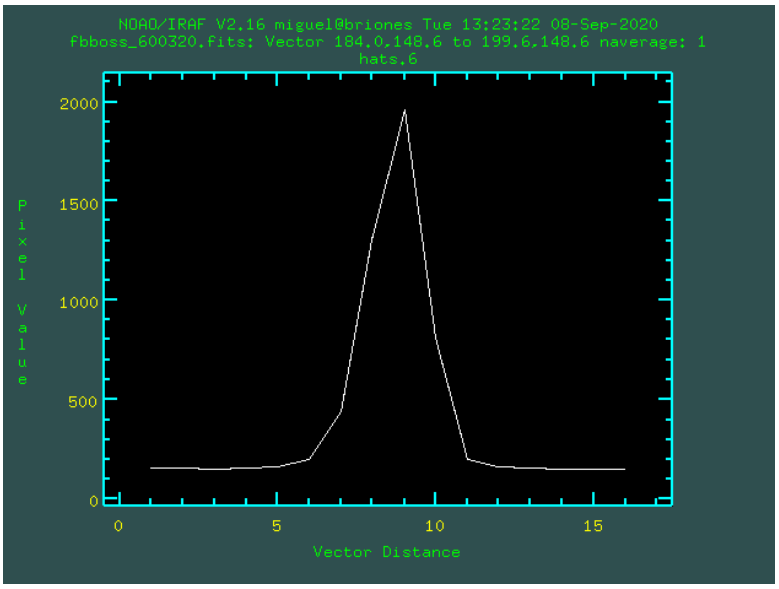

Figure 4.14: Idem to Figure 4.13, but showing the vector plot of HATS-6. The radius1 value is 5 and radius2 is 4.

of the center (**boxsize**), the maximum number of centering iterations to be made (**niterate**) and the tolerance of convergence for the centering algorithm used (**tolerance**). Once these inputs are given, FOTOMCAP will ask for confirmation that all stellar objects are centered in all the images (via visual confirmation of the user), and proceed towards the next part of the code. In case the centers found are not aligned with the stars in the images, a new set of values for the IMCENTROID parameters must be given.

The second part of the code calculates the instrumental magnitudes of each star. For doing so, FOTOMCAP first computes the magnitudes of bright stars using two methods. The selected stars and their coordinates come from the "coords" file we previously edited. The first computing process uses the growth curves method where several measurements of each star magnitude are performed, but with each consecutive measurement the radius of the aperture increases up until it equals the "radius1" previously mentioned (see Subsection 4.2.1). The final magnitude value chosen by FOTOMCAP, called m_{CC}, will be the one that remains constant, despite the increasing in size of the aperture radius (Petrucci & Jofré 2016). In the second computing process, FOTOMCAP calculates the S/N ratio value for each star with progressively larger apertures up until it equals the "radius2" previously calculated. Finally, it selects on the final value of the magnitude, m_{SN}, once the S/N ratio value is maximum in a given aperture radius (Petrucci & Jofré 2016). FOTOMCAP uses the PHOT task to calculate both m_{CC} and m_{SN}. The PHOT[9] task is designed to perform aperture photometry on a list of stars, and is part of the DAOPHOT package. As input, PHOT needs: a list containing the images of the transit observation, a text file with the initial coordinates of the stellar objects (as with the IMCENTROID step, the input file used is "coords") and a file containing the background sky values of every stellar object. These background sky values are required by FOTOMCAP to obtain the stellar center and FWHM, and are automatically calculated by FOTOMCAP in the surrounding area of each star. FOTOMCAP calculates the inner radius of the sky ring as the aperture radius plus five additional pixels, and the outer ring radius is calculated as the aperture radius plus ten more pixels (see Figure 4.15 for reference). Inside this annulus, FOTOMCAP obtains the background sky values for each stellar object. For every i star present in the "coords" file, FOTOMCAP computes $\Delta m_i = (m_{CC} - m_{SN})_i$ and then, calculates the Δm of the whole image as the median of these Δm_i values (Petrucci & Jofré 2016). This Δm is used as the aperture correction in each image. In the last step, the instrumental magnitude m_{ins} of each star in the field of the image (registered in the "refcoords" file previously created) is obtained via $m_{ins} = m_{SN} + \Delta m$. The errors used by FOTOMCAP are those obtained by the PHOT[10] task (Petrucci & Jofré 2016). The error of the magnitude that PHOT calculates is given by: $merror = (1.0857 \cdot error)/f$; with $error = \sqrt{\frac{f}{epadu} + A \cdot \sigma^2 + A^2 \cdot \frac{\sigma^2}{n_{sky}}}$, where f is the stellar flux, $epadu$ is the CCD gain, A is the area of the aperture in square pixels, σ is the standard deviation and n_{sky} is the number of sky pixels. The output of FOTOMCAP consist of three files. The first file, contains the instrumental magnitude

[9]For more information on PHOT visit the page: https://iraf.net/irafhelp.php?val=daophot.phot&help=Help+Page
[10]More information about the PHOT task on the following page: http://iraf.noao.edu/scripts/irafhelp?phot

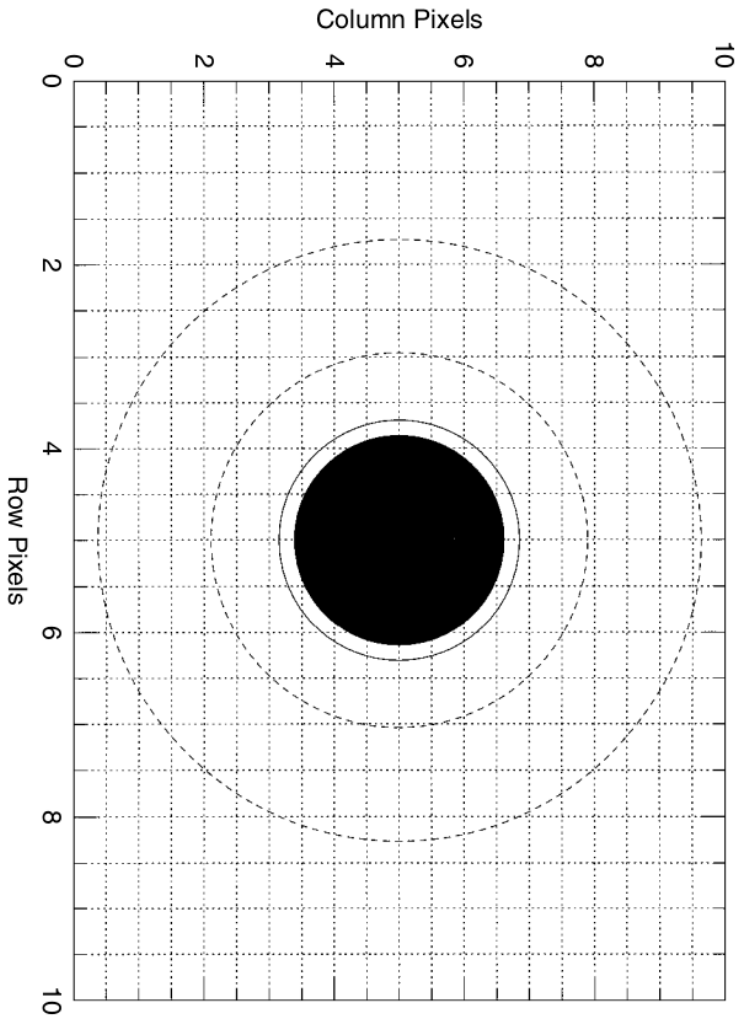

Figure 4.15: Representation of a stellar object on a CCD pixel grid. Vertical and horizontal axes correspond to the pixel array coordinates. The solid line represents the aperture of the star, and the dashed lines the inner and outer background sky annuli. To estimate the background level, the number of counts of the pixels inside the annuli are added up and divided by the number of pixels inside the annuli. Example figure taken from Howell (1989).

and error values of all the computed stars in every image. The second file contains the measured background sky level of every image. And the last file, has the FWHM value calculated for every image. With this result we continue the process into the next part, the differential photometry technique.

4.2.2 Differential Photometry

Differential photometry is a technique that allows one to measure short term variations from bright objects with a high degree of photometric precision (Howell 2006). Differential photometry is particularly useful when observing crowded fields of astronomical objects, or when searching for variable sources, in this case, exoplanets. The differential photometry process consists of taking a measurement of several sources on the same CCD image, employing a differential technique to eliminate the extrinsic variations (caused by the atmospheric extinction) in a systematic way, that only leaves the signal of the object of interest (Howell 2006). Differential photometry consists in creating a difference in magnitude or flux ratio between the star of interest V, and one or more stars of the same image field that will serve as comparison C_i. When this difference in magnitudes $V - C_i$ or flux ratio V/C_i is applied to every image of the transit observation, it allows us to obtain a light curve with a high degree of precision, with the brightness variations produced by the atmospheric extinction or observing conditions removed. The criteria used to select comparison stars are that these must be non-variable objects, isolated from any other stars in the field so that their measured brightness does not overlap with that of other stars, and to

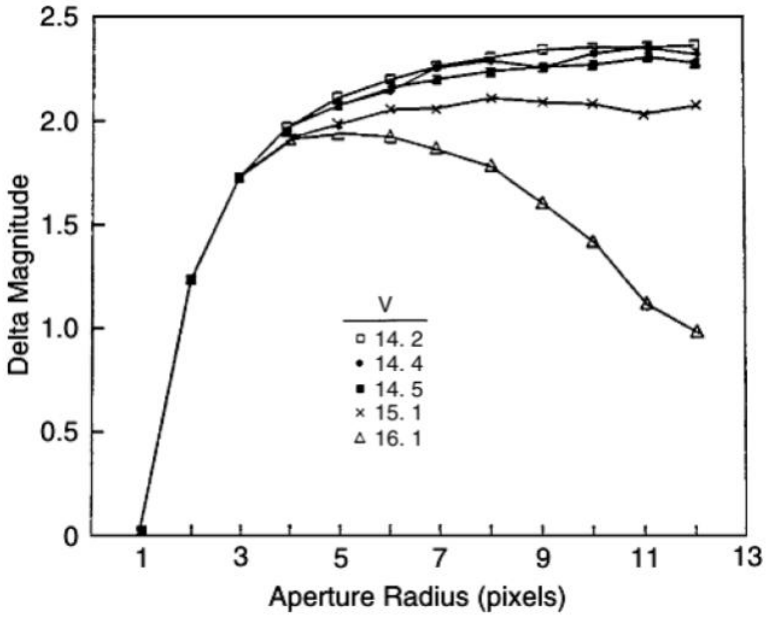

Figure 4.16: Plot showing the growth curves of five stellar objects in a CCD frame. The horizontal axis represents the increase in the aperture radius, while the vertical axis is the difference in magnitude between the successive apertures of each star. The visual magnitude reported for each star is also shown with different symbols. In this figure, we see that the growth curves for the three brightest objects share a similar growth, while for the other two, fainter objects (shown in x's and triangles), deviate from this mean as the aperture increases. Figure taken from Howell (1989).

produce the light curve with the smallest dispersion possible. Also, when calculating the differential magnitude it is important that the comparison stars do not possess a significant variation in their instrumental magnitude throughout the transit observation.

To obtain the light curves of the transit observations of WASP-69 and HATS-6 we applied the differential photometry technique, and chose the stars used as comparison with a code written in IRAF, RESTARCORAP. RESTARCORAP is a custom written program that searches if any of the stellar objects found by DAOFIND in the field of every image is variable, i.e., if its measured flux varies during the entire transit observation. When loading RESTARCORAP into IRAF environment as a task, the program will ask as input: a list with the name of all the reduced images, the magnitudes file created by FOTOMCAP, the total number of selected stars in the field of the images (same number as the one in the "refcoords" file) and the name of the output file (in this case, our file is named "estadistica"). What we get is an output file where the first two columns of the data represent the ID of each star, with the last column being the standard deviation resulting of calculating the difference in magnitude for every combination of stars ($s1 - s2,\ s1 - s3,\ s1 - s_n,\ s2 - s3,\ ...$). We are interested in the results obtained for the difference in magnitude between our star of interest and the rest of comparison stars. With this data, we can try and perform the differential photometry using comparison stars with the smallest standard deviation. The standard deviations obtained with RESTARCORAP for the stars in the fields of WASP-69 and HATS-6 are shown in Tables 4.2 and 4.3.

Continuing with the last part of the photometric process, we load the FOTDIFFLU program into the IRAF environment as a new task. FOTDIFFLU is another custom written program that calculates the difference in instrumental magnitude between the selected comparison stars and the object of interest. FOTDIFFLU works by receiving as input: the list containing all the images, the FOTOMCAP magnitudes file, a file with the identification number of the comparison stars and the name of the output file that will contain the results of the differential photometry. Inside the file with the identification number we can declare any type of combinations for stars to be used as comparison however, we are only interested in using those that have been shown by the RESTARCORAP task to have the smallest standard deviation. The output file of this task contains four columns of data for every image. The airmass of the image, the date (in HJD), the relative (or differential) flux and the uncertainty of the relative flux as measured by IRAF. For WASP-69, three comparison stars with numbers 2, 4 and 9 were chosen given that the three had the smallest standard deviation values (see Table 4.2).

Table 4.2: RESTARCORAP program results for the WASP-69 observations.

ID	x center (pixels)	y center (pixels)	σ	Comparison info
1	499.984	101.341	0.02062	Not used
2	1045.886	404.074	0.01755	Used
3	1593.917	607.273	0.12760	Not used
4	375.826	750.163	0.01321	Used
5	1348.523	970.515	0.02215	Not used
6	598.510	1014.232	-	WASP-69
7	1672.339	1018.986	0.02607	Not used
8	1769.553	1120.576	0.02702	Not used
9	1146.854	1547.529	0.01964	Used
10	343.045	1562.707	0.27332	Not used
11	197.752	1583.187	0.27326	Not used
12	1540.662	1650.832	0.28138	Not used
13	929.998	1763.203	0.27650	Not used

Note: The first column corresponds to the stellar object identification number as found by DAOFIND and saved into the "refcoords" file. The identifications of the stars in this table correspond to those shown in Figure 4.11. Here, x center and y center correspond to the stellar objects central coordinates found by DAOFIND in the pixel array, and σ is the standard deviation for the difference between the comparison stars and the WASP-69 star (object number 6).

For HATS-6, three comparison stars with numbers 2, 3 and 5 were selected as comparison stars (Table 4.3). The comparison stars used in the analysis of both planets were not flux weighted in any way, i.e., a simple sum is used, independent of their value in magnitude.

Most of the light curves obtained from the literature, and the ones obtained from our WASP-69 and HATS-6 observations had the date of the transit data in HJD format. We used the online tool[11] presented by Eastman et al. (2010) that allows us to convert the date of our observations from HJD to Barycentric Julian Days (BJD). Where these BJD refer to the Julian Date on Earth corrected for the differences in the planet's position with respect to the barycenter (center of mass) of the Solar System. As input, we give the dates of the transit, and the right ascension and declination of the star of interest.

Now that we have converted the date, we proceed to changing the units of our light curves from relative flux to relative magnitude. For this, we simply convert the fluxes using the flux-magnitude relation $m = -2.5 \cdot log_{10} f$ where m is the relative magnitude and f the relative flux. For the errors, we calculated them using error propagation, where $\sigma_m = \frac{dm}{df}\sigma_f$, so we get that the error for the relative magnitude is $\sigma_m = 1.0857\frac{\sigma_f}{f}$, that is obtained by differentiating the flux-magnitude relation. For those light curves that we gathered from the literature without any flux errors we obtained them by calculating the standard deviation from the out of transit data of the light curve and assigning that value to all the points of the transit.

The light curves generated from FOTDIFFLU still contain some dispersion in the measured magnitude caused by systematics contributions (correlated noise). These systematicities are generated by the observing conditions and characteristics of the telescope and CCD, such as the airmass, FWHM of the star, and the displacement of the center of the star in the x and y axis of the pixel array of the CCD. These systematic contributions can be minimized by using a multiple linear regression model that uses the residuals (o-c) and systematics. In this case, the residuals come from a model given by the JKTEBOP code where all input parameters are fixed (see section 4.3). For this purpose, we use the "corsis" program, a PYTHON3 code that corrects the differential photometry results obtained from a transit, using a multiple linear regression model. This program needs as input a text file that contains: the date in BJD, the relative magnitude of the transit, the error of the relative magnitude, the airmass, the FWHM (in arcsec units), the displacement of the comparison star in the x axis (in pixels), the displacement of the comparison star in the y axis, the sky value obtained for the comparison star, the peak value of the comparison star, the x displacement of the star of interest, the y displacement of the star of interest, the sky value of the star of interest and the peak value of the star of interest. The corsis code runs a total of six multiple linear regression models, each one running with a different combination of input parameters, and each giving as output: a χ^2_ν value, the BJD date, input relative magnitude, error of

[11]The HJD to BJD conversion tool can be found in the following link: http://astroutils.astronomy.ohio-state.edu/time/hjd2bjd.html

Table 4.3: RESTARCORAP program results for the HATS-6 observations.

ID	x center (pixels)	y center (pixels)	σ	Comparison info
1	196.310	117.273	0.02537	Not used
2	189.948	127.166	0.02082	Used
3	189.416	135.206	0.02100	Used
4	192.106	148.337	-	HATS-6
5	120.184	161.327	0.01912	Used
6	171.409	166.951	0.10145	Not used
7	133.278	206.452	0.02199	Not used
8	196.298	209.808	0.02485	Not used
9	206.231	220.646	0.02197	Not used
10	133.860	260.545	0.06107	Not used
11	226.043	273.710	0.06020	Not used
12	144.093	279.210	0.05881	Not used
13	235.695	281.814	0.06081	Not used
14	167.840	286.321	0.06080	Not used
15	284.320	287.667	0.06121	Not used
16	245.146	296.711	0.06296	Not used
17	213.564	300.300	0.06261	Not used

Note: Same as with Table 4.2, these are the stellar objects used by RESTARCORAP using the "refcoords" file. For this observation, HATS-6 is the star number 4.

the relative magnitude, the systematic magnitude found by the model, and the corrected magnitude obtained by subtracting the systematic magnitude to the original magnitude. Out of six possible models, we chose the model that gave the smallest value of χ^2_ν. This step was only applied to the WASP-69 light curve observed from the EABA observatory (see Chapter 3), as we considered that the contribution of systematics to the light curve were considerable. This was not the case for the HATS-6 observation, where the light curve data of the transit was not significantly affected by systematics.

The final results obtained in this section can be seen in Figures 4.17 and 4.18, where we show the normalized light curves obtained from the WASP-69 and HATS-6 system observations described in Chapter 3 and two transit models that fit the data using JKTEBOP. The tables containing the differential photometry results with FOTDIFFLU for the WASP-69 and HATS-6 transit observations are shown in Tables A.1 and A.2.

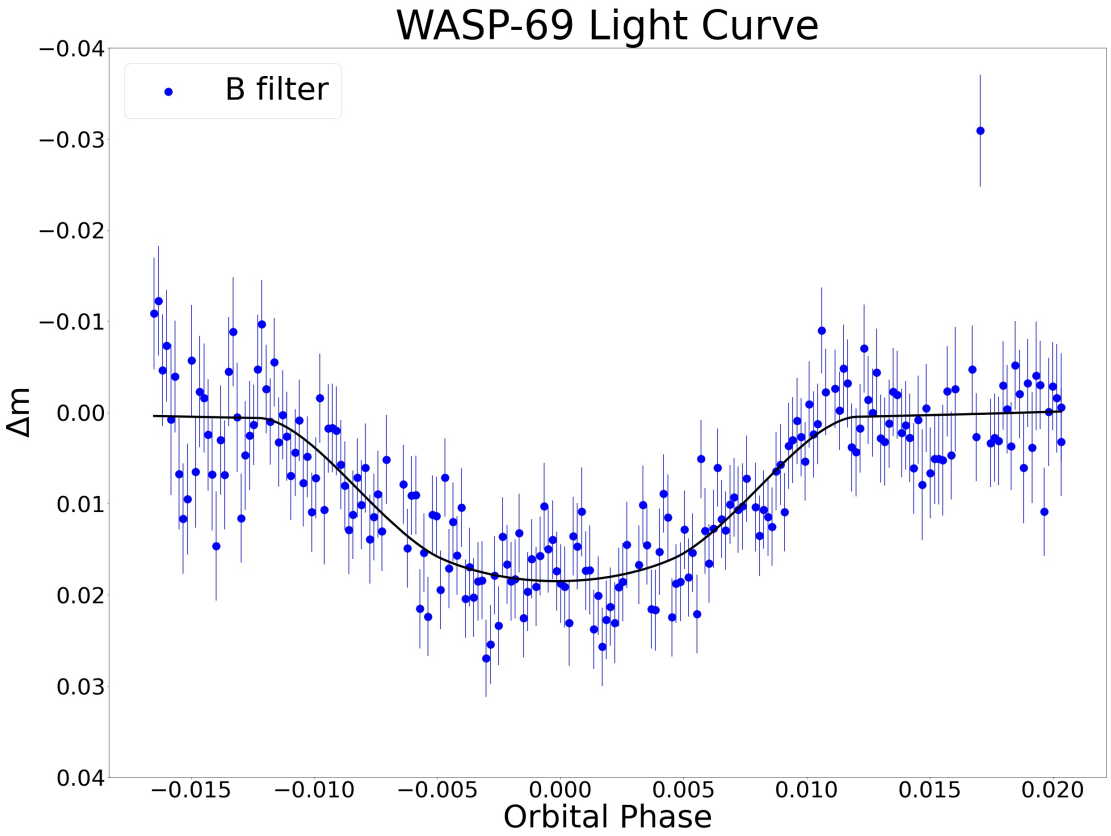

Figure 4.17: Normalized light curve obtained from the WASP-69 transit observation. The horizontal axis represents the phase of the light curve, where zero is the point of mid transit. The vertical axis shows the normalized relative magnitude of the light curve. This light curve was corrected from systematic noise using the "corsis" program. The black line is the model found for this light curve that best fits the data, using a transit model with quadratic coefficients for the limb darkening law of the star (also explained in the next section).

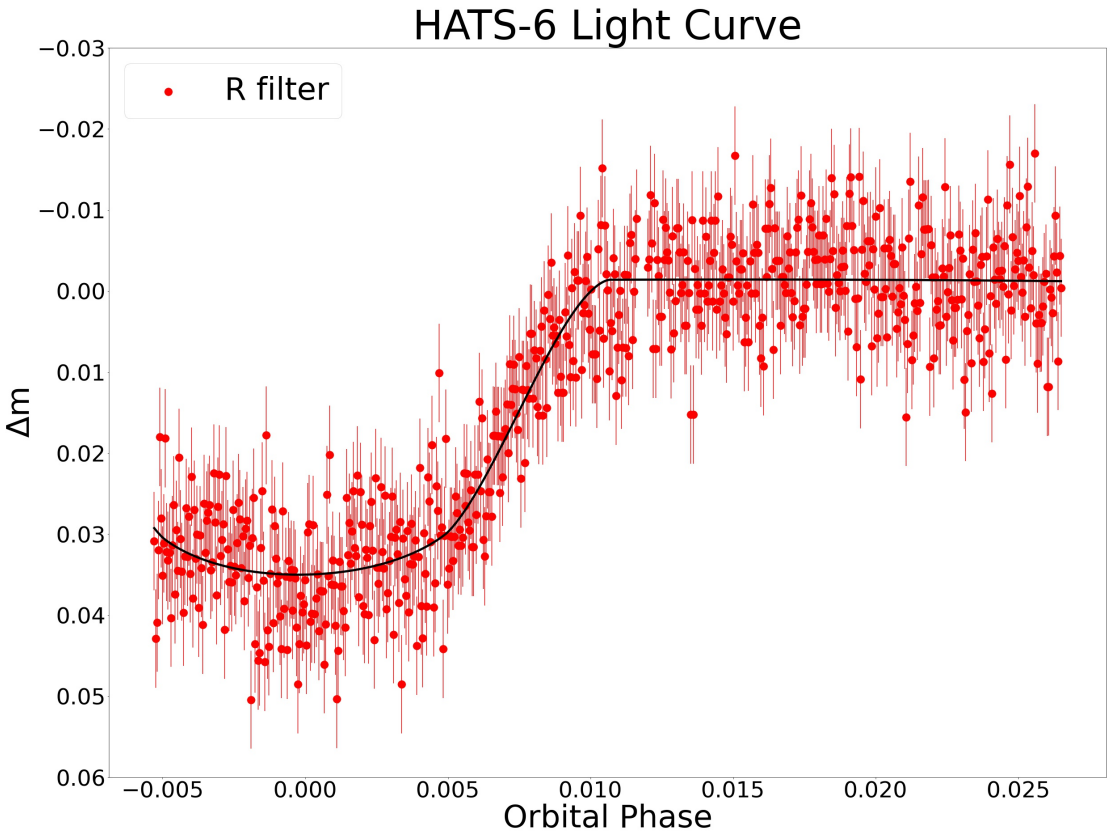

Figure 4.18: Normalized light curve obtained from the HATS-6 transit observation. Same as Figure 4.17, the x-axis shows the phase of the transit, the y-axis the normalized magnitude. The black line is the transit model found by the JKTEBOP program that best fits the data, using quadratic coefficients for the limb darkening law. As stated in Chapter 3, only the third and fourth points of contact, i.e., half of the light curve, is displayed here.

4.3 Transit Fitting

In this section, we explain the process of how the transit of a planet is fitted using a model that describes the transiting phenomena. In this work, the goal of fitting a transit is to obtain a measurement of its transit depth and inclination. This allows us to estimate the radius of the star, the radius of the planet, the orbital inclination and the orbital semi-major axis of the planet.

For WASP-69, we used the EABA light curve derived in Chapter 3 and the light curves available in the literature, taken from Anderson et al. (2014), Murgas et al. (2020), and the Exoplanet Transit Database (ETD)[12]. For HATS-6, we used the CASLEO light curve derived in Chapter 3 and the light curves from Hartman et al. (2015a), the TESS space mission (Ricker et al. 2015), and the ETD. In Table 4.4 we present a summary of the observations (both photometric and spectrophotometric) that we gathered from the literature.

Table 4.4: Summary of observations taken from the literature

Planet	Author/Source	Facility	Date	Number of Images	Filter/Wavelength Range
WASP-69b	Anderson et al. (2014)	Euler/EulerCam	2011 Nov 10	367	Gunn-r
WASP-69b	Anderson et al. (2014)	TRAPPIST	2012 May 21	873	Sloan z'
WASP-69b	Murgas et al. (2020)	GTC/OSIRIS	2016 Oct 05	590	515-905 nm
WASP-69b	Rea (2016)	PCO	2016 Aug 28	245	Clear
WASP-69b	Bretton (2019)	BPO	2019 Sep 27	322	V
WASP-69b	Gaitan (2020)	-	2020 Sep 13	43	R
HATS-6b	MAST[a]	TESS	From 2018 Dec 11 to 2019 Jan 07	1675	TESS-band[b]
HATS-6b	Hartman et al. (2015a)	GROND/MPG 2.2 m	2014 Mar 06	95	g
HATS-6b	Hartman et al. (2015a)	GROND/MPG 2.2 m	2014 Mar 06	95	r
HATS-6b	Hartman et al. (2015a)	GROND/MPG 2.2 m	2014 Mar 06	95	i
HATS-6b	Hartman et al. (2015a)	GROND/MPG 2.2 m	2014 Mar 06	95	z
HATS-6b	Hartman et al. (2015a)	LCOGT[c] 1 m	2013 Dec 07	149	i
HATS-6b	Hartman et al. (2015a)	CTIO 0.9 m	2012 Sep 03	34	Gunn-z
HATS-6b	Jongen (2020)	DSC	2020 Feb 02	84	Clear
HATS-6b	Bretton (2015)	BPO	2015 Jan 06	113	Clear

[a]MAST stands for Mikulski Archive for Space Telescopes and its website can be found in https://archive.stsci.edu/missions-and-data/tess.
[b]The TESS-band corresponds to wavelengths between 600 and 1000 nm.
[c]LCOGT stands for Las Cumbres Observatory Global Telescope Network (Brown et al. 2013).

For the transit of every planet gathered, we fitted a model that best fits each light curve using the JKTEBOP code. JKTEBOP is a code written in FORTRAN 77 originally presented by Southworth et al. (2004)[13]. It is based on the EBOP code (Etzel 1981; Popper & Etzel 1981). JKTEBOP is used to fit a model to a light curve of a detached eclipsing star-star or star-planet system. It works by representing the host star and its planet as biaxial spheroids but adopting a spherical approximation for the calculation of light lost during an eclipse (Southworth 2013). JKTEBOP works with data from light curves (in relative magnitude units) and an input file containing the initial estimated values of each parameter. It then proceeds to fit the light curve with Levenberg-Marquardt minimization and generates a file containing the model found that best fits the transit, a file with the fitted parameters and their uncertainties, and a file with the residuals of the observations. The formal uncertainties of the fitted parameters are given by the covariance matrix done with the minimization algorithm; however, these are not the final uncertainties reported. That is because uncertainties obtained from the solution covariance matrix are unreliable in the presence of parameter correlation (Popper 1984; Maceroni & Rucinski 1997; Southworth & Clausen 2007). Instead, we made use of Montecarlo (MC) and residual-permutation (RP) simulations (also done with JKTEBOP) to estimate reliable parameter uncertainties, which are proven to give reliable results as shown in Southworth et al. (2005).

The main parameters fitted by JKTEBOP are: the orbital inclination (i), the time of mid-transit (T_{mid}), the sum of fractional radii ($r_s + r_p$), and the fractional radii of the star and planet r_s and r_p (Southworth et al. 2004). These radii are defined as $r_s = R_s/a$ and $r_p = R_p/a$, where R_s and R_p are the radii of the star and planet respectively, and a is the orbital semi-major axis of the planet. JKTEBOP reads as input the parameters i, T_{mid}, $r_s + r_p$, $k = r_p/r_s = R_p/R_s$ and fits them (Southworth et al. 2005). The advantage of this method, comes from the fact that, these two quantities are weakly correlated for a wide variety of light curve shapes, which in turn, improves solution convergence of the code (Southworth 2008). Note that the ratio of the fractional radii squared k^2 is commonly referred to as the transit depth ($\Delta F = k^2$) of a light curve. We fixed the P_{orb} to the value known from the literature for a planet, because JKTEBOP does not run simultaneously the analysis of

[12]The ETD website can be found in http://var2.astro.cz/ETD/index.php
[13]The code and more information regarding how to download, install and run JKTEBOP can be found in https://www.astro.keele.ac.uk/jkt/codes/jktebop.html

all the light curve data available. Another parameter needed by the code is the mass ratio (M_p/M_s), which determines how aspherical the system is in the EBOP code (Southworth 2008). It has a negligible effect on the solutions found by JKTEBOP for transiting planets (Southworth 2008), so we leave it fixed to the ratio that we calculate from the most accurate measurements of the planet and star masses reported by other authors. We left the eccentricity of the orbit fixed at zero. This is because, for the planets of this sample, it has been shown in previous works that the eccentricity is zero or close to zero (Faedi et al. 2011; Anderson et al. 2014; Hartman et al. 2015a; Mancini et al. 2018). We note that, from now on, we refer to k, T_{mid}, i and the sum of radii, i.e. $r_s + r_p$ as the photometric parameters of the transit. In Tables 4.5 and 4.6 we show the initial values for the parameters used in JKTEBOP.

Table 4.5: Parameters used in JKTEBOP from the literature as the initial input for WASP-69.

Parameter	Murgas et al. (2020)
$r_s + r_p$	0.093818
k	$0.13238\ ^{+0.00091}_{-0.00094}$
i (°)	$88.692\ ^{+0.122}_{-0.123}$
M_p/M_s	0.0003008
P_{orb} (days)	3.86814
ecc	0

Table 4.6: Parameters used in JKTEBOP from the literature as the initial input for HATS-6.

Parameter	Hartman et al. (2015a)
$r_s + r_p$	0.0860
k	0.17978 ±0.00077
i (°)	88.210 ±0.084
M_p/M_s	0.0005305
P_{orb} (days)	3.32527
ecc	0

Before we perform any type of fitting to the light curve data, we must first make sure that the light curve is normalized. Normalization of a light curve is done by scaling the out of transit magnitude value of the light curve to zero (or unity in case of flux) and by fitting a polynomial function that levels the out of transit to the desired "normal" value of the light curve. In this work, all our light curves are presented in magnitude, with the normalized out of transit value being zero. Normalization allows to adjust different light curves with variable values of magnitude to a same scale that allows for an easy management of the data and ease in visualization. JKTEBOP can fit a polynomial function to a light curve and calculate the out of transit value (initially set to zero by us), should the data given be non-normalized. The transit model and the polynomial fitting are done simultaneously by JKTEBOP. In this work, we used most of the time a second order polynomial to fit the light curves that needed to be normalized. The majority of the light curves gathered from the literature were already normalized and thus, the second order polynomial fitting became unnecessary in most cases.

For this work the effect of limb darkening from the host star in the light curves was accounted for. Stellar limb darkening (LD) is an optical effect observed in stars, where the central disk appears to be brighter than the limb of the disk. In the center of the stellar observable disk, photons from hotter, deeper layers escape to the surface and become observable to us back on Earth. Near the limb of the star only photons from upper, colder layers pass through the stellar interior. The general effects of LD are important in several branches of stellar physics, including exoplanet transits (Southworth 2008). Some of the changes to light curves due to LD include a measurable change in ΔF, shaping the bottom part of the transit, giving it a "rounder" bottom and blurring the boundary between ingress/egress. Because of this, astronomers use equations which describe the LD in function of which part of the star is being eclipsed by the planet when fitting light curves.

LD laws are described as a function of $\mu = \cos\gamma$ where γ is the angle separation between a line normal to the stellar surface and the observer's line of sight. In this work, we only used a quadratic LD law; nonetheless it should be known that there are other types of LD laws (linear, logarithmic, square-root, cubic). We ran JKTEBOP adopting a quadratic LD law, because it has been shown by Southworth et al. (2007), that using a quadratic LD law can give better results compared to other types of LD laws for the type of host stars in our

sample. The quadratic LD law used, as given by Kopal (1950) is:

$$\frac{I_\mu}{I_0} = 1 - c_1(1-\mu) - c_2(1-\mu)^2$$

where I_0 represents the total intensity at the center of the stellar disk and I_μ the total intensity at an angle γ. In this equation, c_1 and c_2 represent the linear and non-linear coefficients respectively. LD coefficients are wavelength dependent, so the value changes depending on the wavelength range used to perform the observation of the transit. To find out the limb darkening coefficients needed, we made use of the JKTLD code (Southworth 2008)[14]. This code (also written in FORTRAN 77) performs bilinear interpolation to determine limb darkening coefficients from published grids of coefficients for linear, quadratic, logarithmic and square-root LD laws. Naturally, we only needed the coefficient values given for the quadratic LD law. The input parameters needed by JKTLD are: the stellar effective temperature (K), surface gravity of the star, stellar metallicity and microturbulence velocity (km/s). The name that JKTLD assigns these parameters is T_{eff}, $logg$, $[M/H]$ and $Vmicro$ respectively. The JKTLD code outputs a file with the values of the LD coefficients in several passbands. JKTLD works with tables calculated from theoretical studies done by van Hamme (1993); Diaz-Cordoves et al. (1995); Claret et al. (1995); Claret (2000); Claret & Hauschildt (2003); Claret (2004); Sing (2010).

As to how the MC algorithm used by JKTEBOP works, it first finds the solution that best fits the light curve data and uses the result to create a model light curve with the same time sampling (Southworth 2008). Then, Gaussian noise is added by the algorithm and the resulting synthetic light curve is fitted with the same conditions as the real one (Southworth 2008). The number of Montecarlo simulations that the code runs depends on a number given as input by the user. The 1 σ uncertainties in the fitted parameters are taken from the distribution of best fits to the simulated light curves (Southworth 2008). For the fitted parameters given by the input, the program applies random perturbations just before fitting the synthetic light curve in order to get a detailed mapping of the parameter space and explore parameter correlation (Southworth 2008). The disadvantage of the MC algorithm is that, despite being able to correct random noise in the light curve, it is incapable of accounting for correlated "red" noise that produces systematic errors in the data (Southworth 2008). For this work, we have used 10,000 Montecarlo simulations each time we ran the algorithm to fit the given input parameters with JKTEBOP.

The RP algorithm (Jenkins et al. 2002), takes the residuals from the best fitting light curve solution and shifts them to the next data point. Then a new best fit is found and again are the residuals shifted with those which drop off the end of the data set being wrapped around to the start of the data (Southworth 2008). This iteration is completed when the residual have been cycled back to their original positions which results in a distribution of values for the fitted parameters from which we can estimate their uncertainties (Southworth 2008). However, for light curves with a low number of data points (less than a thousand), the reliability of the method is constrained, because the algorithm does not have the number of iterations that are necessary to make a good exploration of the parameter space of the fitted parameters.

The LD has a considerable effect on the results found for the fitted parameters of a light curve, this is why the first step consists in running JKTEBOP using a quadratic law and three different options for the LD coefficients. In the first one, both LD coefficients are fixed, in the second one both LD coefficients are fitted and in the last one, the linear coefficient is fitted and the non-linear coefficient is perturbed. From the three models generated by JKTEBOP for each transit, we selected the option with a reduced chi-square χ^2_ν with the closest value to the unity.

The initial values of the input parameters are obtained from the literature. For WASP-69, the parameters were taken from Anderson et al. (2014); and for HATS-6, we used parameters given by Hartman et al. (2015a). The values given as output by the JKTLD code for the LD coefficients were used as initial input. If the observation of a transit was made using a filter that does not exist in the catalog of the JKTLD code, we used the most similar filter available in JKTLD. JKTEBOP allows the user to change whether certain input parameters remain fixed or are to be fitted. The fitted parameters are the photometric parameters previously mentioned $(k, i, T_{mid}, r_s + r_p)$, as well as the out-of-transit value of the light curve. Also, models in which the sum of both LD coefficients was above one or below zero, were discarded, given that models with these LD coefficient values are physically unlikely. This first result will serve to select which combination of LD fitting will be used for the rest of the steps using JKTEBOP.

For the next step with JKTEBOP, we fitted the photometric parameters to obtain our own values and uncertainties. In order to account for all the light curves we took from the literature, we modified the error bars of

[14]The code is available from https://www.astro.keele.ac.uk/jkt/codes/jktld.html

the light curves data by making the reduced chi-square $\chi^2_\nu = 1$. For us to obtain the best possible photometric parameters we only used light curves of transits that are complete (ingress and egress are to be found in the light curve) and with the smallest amount of red noise and systematic noise. We used a quadratic LD law and the same LD coefficients values for each passband. The LD fitting option selected was that, which gave the smallest value of χ^2 in the previous step. Input parameter values and fitted parameters remain the same as before, as well as the use of a polynomial fit for non-normalized light curves. The 1σ error bars are obtained with 10,000 MC simulations. This number was chosen because it gives a good balance between computational time and avoidance of small-number statistics. Error bars were also obtained with the RP algorithm. Originally, the photometric parameters and error bars were to be selected from the algorithm that yielded the larger uncertainties. However, due to many of the light curves having less than 1000 observations, we concluded that the results produced by the RP algorithm ($<$ 1000 simulations) were not as statistically robust as the MC method (10,000 simulations), and so, it was decided that all the photometric parameters and their uncertainties would be chosen from the results given by the MC algorithm.

Next, weighted averages of the photometric parameters obtained for each light curve were calculated. The uncertainties from the JKTEBOP MC algorithm were used as weights in the averaging operation for the mean value. The error bars of these new photometric parameters were obtained by calculating the standard deviation of all the values obtained from the light curves for each parameter. An exception in this part of the work was done for HATS-6b. With this planet, instead of creating a weighted average from several transits, the photometric parameters were obtained from the fitting of a single light curve observed from multiple transits observed by the TESS satellite (Ricker et al. 2015). This was decided given the overall nice shape of the TESS light curve. HATS-6b was observed by the TESS satellite with 2-minute cadence in sectors 6 (from 11 December 2018 to 7 January 2019), 32 (from 19 November to 17 December 2020), and 33 (from 17 December 2020 to 13 January 2021). From the Mikulski Archive for Space Telescope (MAST), we retrieved the Presearch Data Conditioning Simple Aperture Photometry (PDC-SAP) (Stumpe et al. 2014) with the tools provided by the Lightkurve python package (Lightkurve Collaboration et al. 2018). Given that the light curves from sectors 32 and 33 show a large dispersion in flux, we decided to use only the photometric data from sector 6. Adopting the orbital period estimated in Hartman et al. (2015a), we phased the seven complete transits from sector 6 and built the LC shown in figure 4.25. Only photometric data between phases 0.45 and 0.55 were considered. This allowed us to reduce the computational time employed by JKTEBOP to perform the fit and to ensure a large number of data points in the out-of-transit. The measurement of the transit depth of the TESS light curve was not included in the transmission spectrum of HATS-6b because it contains light pollution from neighboring stars. The resulting values for each parameter and their comparison with the literature are shown in Tables 4.7 and 4.8.

Using these new values of the photometric parameters as input, we run JKTEBOP one last time to calculate the value of k of every light curve. Once again, using the MC and RP algorithms of JKTEBOP, but this time, on1y fitting k and T_{mid}, while the rest of the photometric parameters and out-of-transit value remained fixed. The quadratic LD law and same LD coefficient fitting option that was previously found were used. From each transit we were able to obtain a value of k from which we could build our own transmission spectrum for the planet. The uncertainties for the fitted parameters were again taken from the MC method. For each of the fitted light curves, we calculated the β factor of the light curve as defined by Winn et al. (2008). This factor allow us to quantify the amount of red noise in the light curve. This factor was added to explain why some of the light curve fittings give odd values of transit depth, so that we can determine if they should be considered in the transmission spectrum of the planet. The method used in this work to calculate the β factor is called "time-averaging", as shown in Winn et al. (2008). First, after using JKTEBOP to obtain the best-fitting model (and residuals), of each light curve, we calculated the standard deviation σ_1 of all the light curve model residuals. Next, we separated the data points of each light curve into M number of bins separated by a time interval, with each bin containing a certain N number of residual values. In this work, we used two time intervals of 15 and 30 minutes. We averaged the residuals in each bin and calculated the standard deviation σ_N of all these averaged binned residuals. As shown in Winn et al. (2008), without any red noise, σ_N would appear as

$$\sigma_N = \frac{\sigma_1}{\sqrt{N}}\sqrt{\frac{M}{M-1}},$$

however, σ_N more often than not is larger than σ_1 by a β factor. The β factor found for each light curve was calculated by averaging the β factor values found using the 15 minute and 30 minute bins. Indeed, some of the light curves obtained from the literature had to be removed from the analysis given that the best models fitted by JKTEBOP were giving a poor fit to the data of the light curve and had a high value for the β factor found for them. In the case of HATS-6b, two light curves obtained from the ETD (both made with no filter),

were excluded from the transmission spectrum of the planet. The β factor of these two ETD light curves was elevated at 2.06 and 1.77. No β factor was calculated for the TESS light curve. For WASP-69b, no light curve was excluded from the transmission spectrum due to their low value of β factor. The results of the fitting process carried out in the last run of JKTEBOP for the k of WASP-69b and HATS-6b are shown in Tables 4.9 and 4.10, were we present the tabulated transmission spectrum of the planet. For WASP-69b, the light curves used in its transmission spectrum, as well as the best-fitted models found by JKTEBOP are shown in Figures 4.19, 4.20, 4.21, 4.22 and 4.23. For HATS-6b, the light curves used in its transmission spectrum, as well as the best-fitted models found by JKTEBOP are shown in Figures 4.24 and 4.25.

Parameter	Symbol (Unit)	This Work	Anderson et al. (2014)	Murgas et al. (2020)
Radii ratio	R_p/R_s	0.1309 $\pm$0.0010	0.1336 $\pm$0.0016	0.13238 $^{+0.00091}_{-0.00094}$
Radii sum	$R_p/a + R_s/a$	0.0927 $\pm$0.0006	-	-
Planetary radius	R_p (R_J)	1.0164 $\pm$0.0162	1.057 $\pm$0.047	-
Stellar radius	R_s ($R_\odot$)	0.7977 $\pm$0.0108	0.813 $\pm$0.028	-
Orbital inclination	i (°)	86.7745 $\pm$0.0488	86.71 $\pm$0.20	86.692 $^{+0.122}_{-0.123}$

Table 4.7: Comparison between the obtained photometric parameters for WASP-69, and those reported in the literature.

Parameter	Symbol (Unit)	This Work	Hartman et al. (2015a)
Radii ratio	R_p/R_s	0.1792 $\pm$0.0021	0.17978 $\pm$0.00077
Radii sum	$R_p/a + R_s/a$	0.0868 $^{+0.0041}_{-0.0042}$	-
Planetary radius	R_p (R_J)	0.9998 $\pm$0.0579	0.998 $\pm$0.019
Stellar radius	R_s ($R_\odot$)	0.5734 $\pm$0.0278	0.570 $\pm$0.011
Orbital inclination	i (°)	88.1548 $^{+0.5083}_{-0.4070}$	88.210 $\pm$0.084

Table 4.8: Comparison between the obtained photometric parameters for HATS-6, and those reported in the literature.

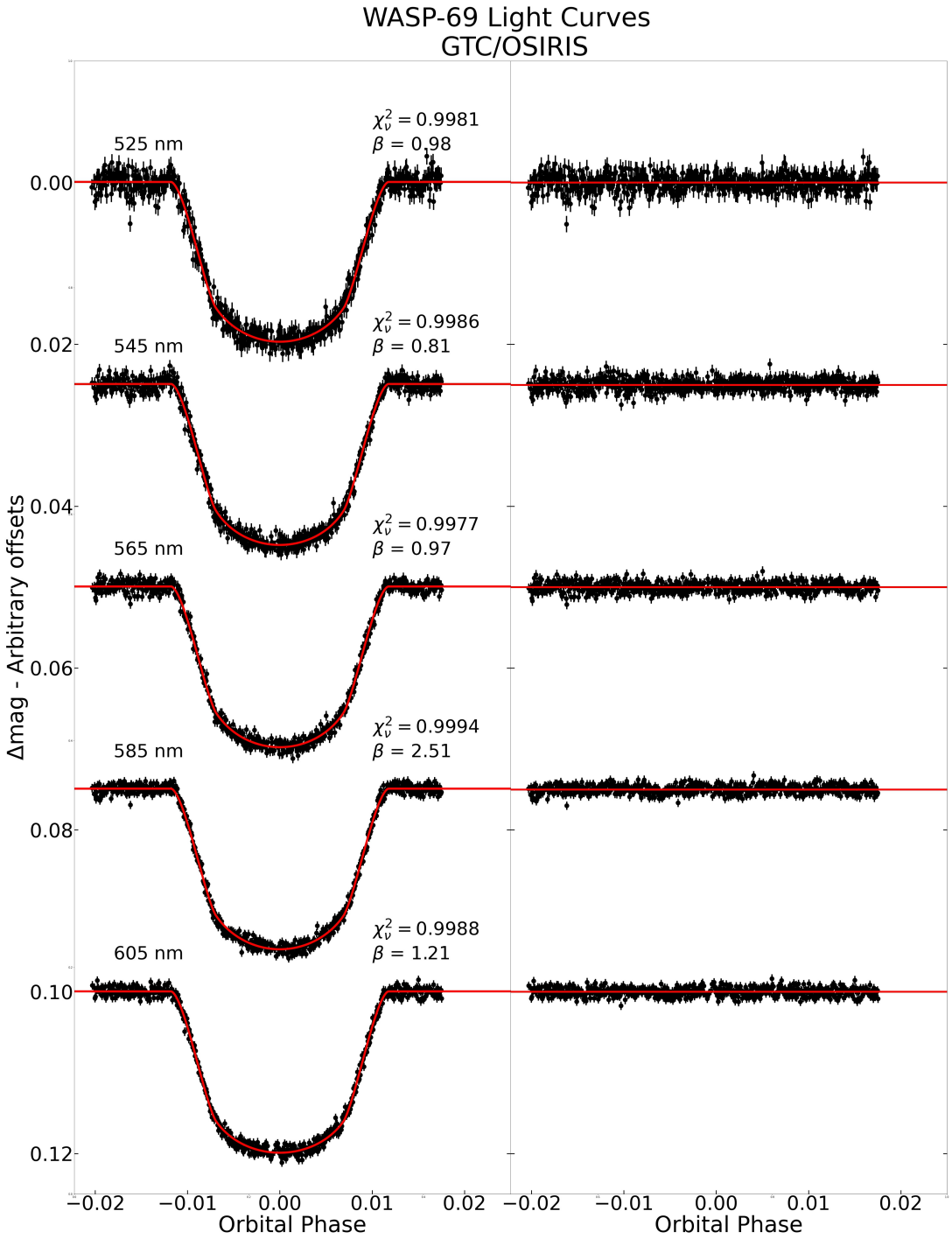

Figure 4.19: Left-hand panel: Phased light curves of the WASP-69b transits. The black data points show the transit light curve magnitude and uncertainty for each observation. The magnitude of the transits has been normalized, with an offset added in the vertical axis for clarity. The solid red line represents the best-fitting model found for the light curve with the MC algorithm. The telescope and band used in the observations are shown on the left of the light curves. The value of χ^2_ν and β factor for each fitting are also shown to the right of the light curve. Right-hand panel: the residuals for each model fitted to a light curve are shown as black points.

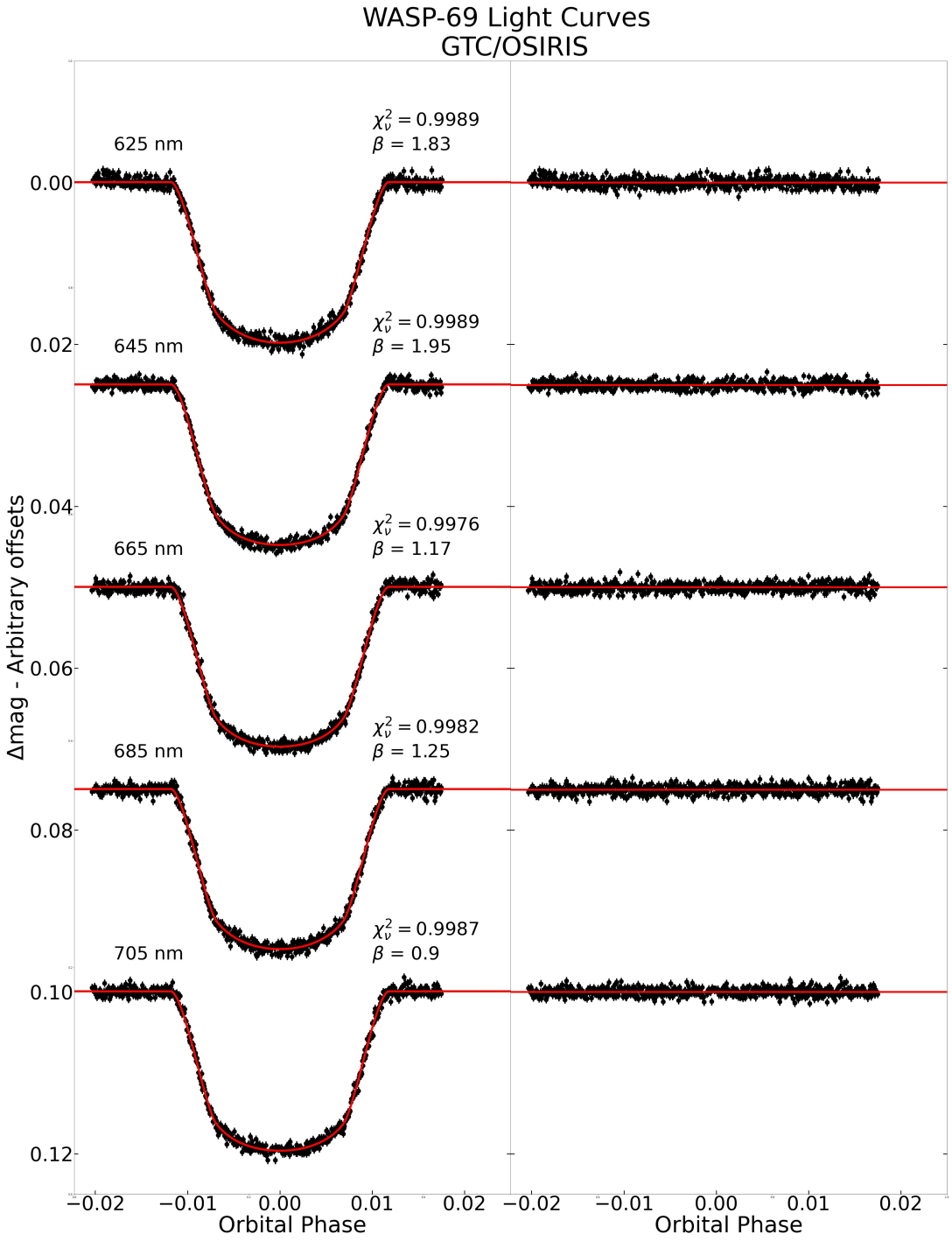

Figure 4.20: Same as Figure 4.19.

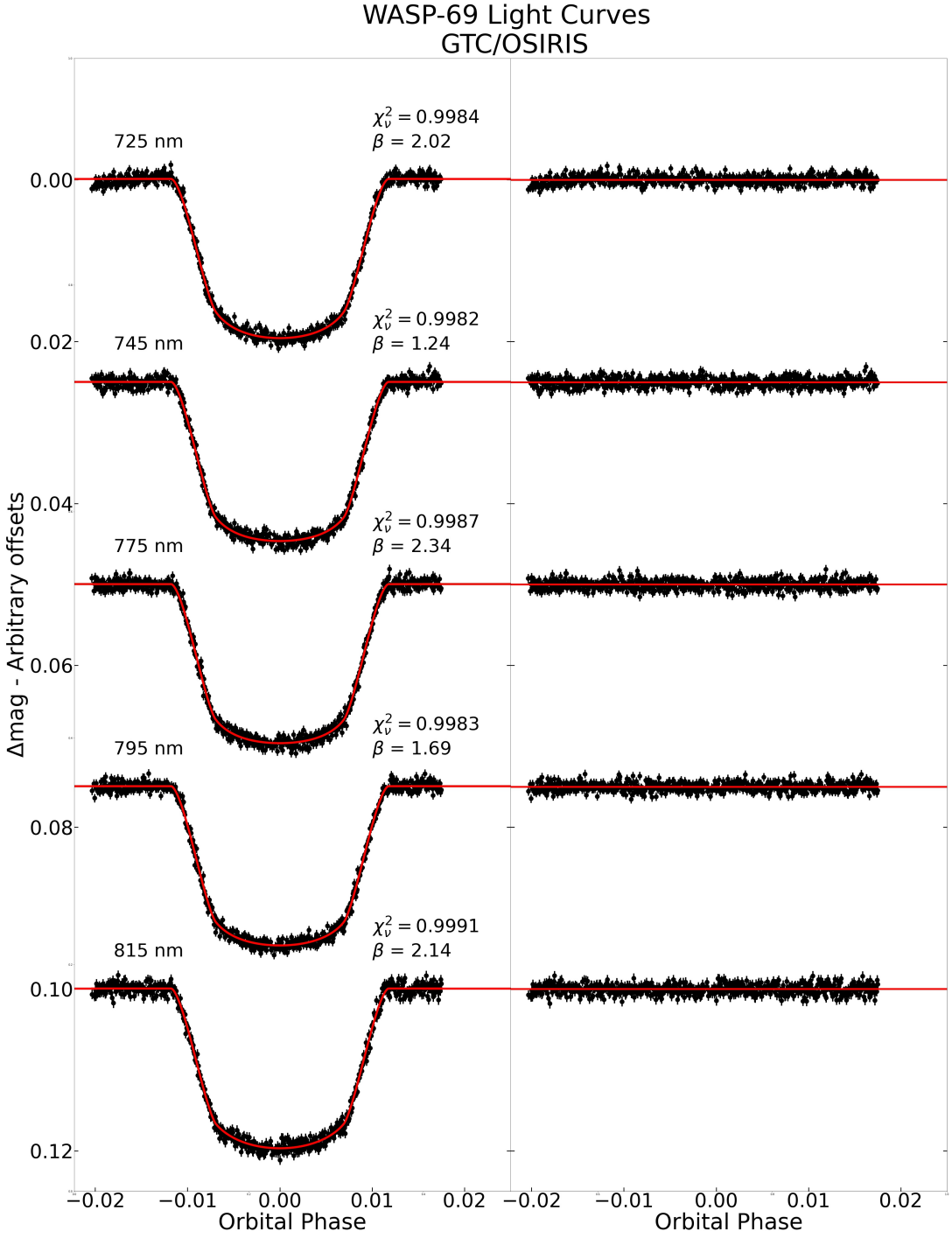

Figure 4.21: Same as Figure 4.19.

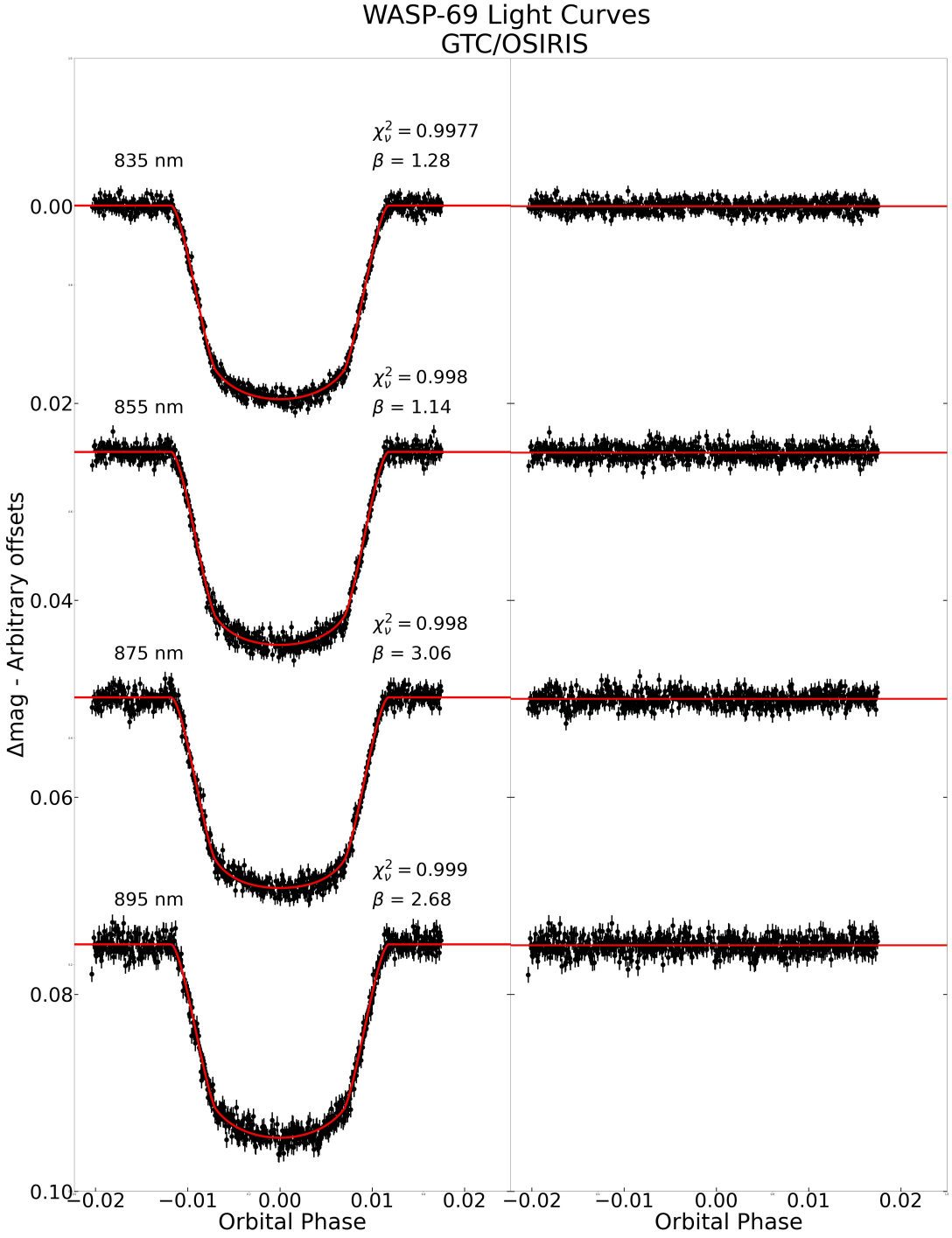

Figure 4.22: Same as Figure 4.19.

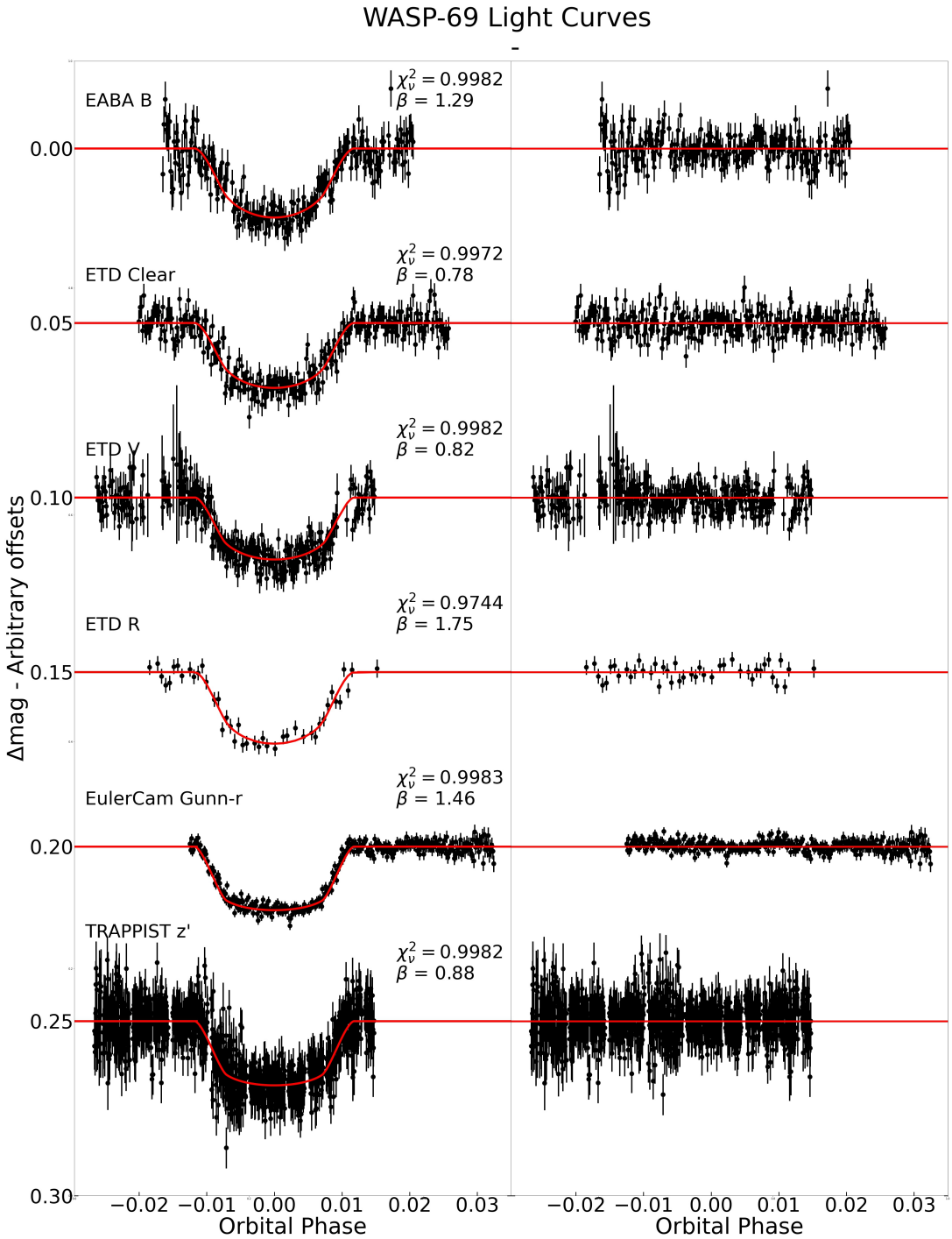

Figure 4.23: Same as Figure 4.19.

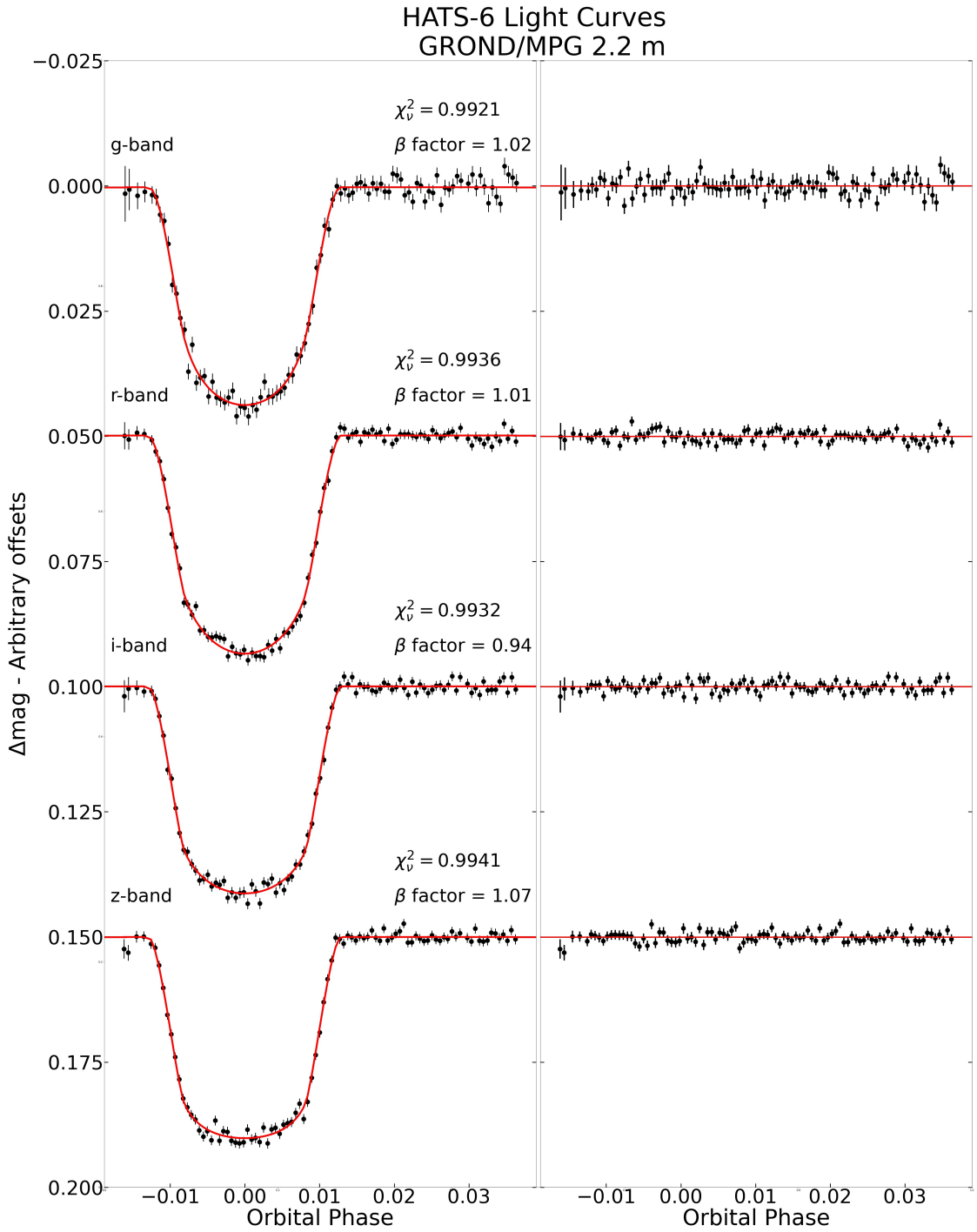

Figure 4.24: Left-hand panel: Phased light curves of the HATS-6b transits. The black data points show the transit light curve magnitude and uncertainty for each observation. The magnitude of the transits has been normalized, with an offset added in the vertical axis for clarity. The solid red line represents the best-fitting model found for the light curve with the MC algorithm. The telescope and band used in the observations are shown on the left of the light curves. The value of χ^2_ν and β factor for each fitting are also shown to the right of the light curve. Right-hand panel: the residuals for each model fitted to a light curve are shown as black points.

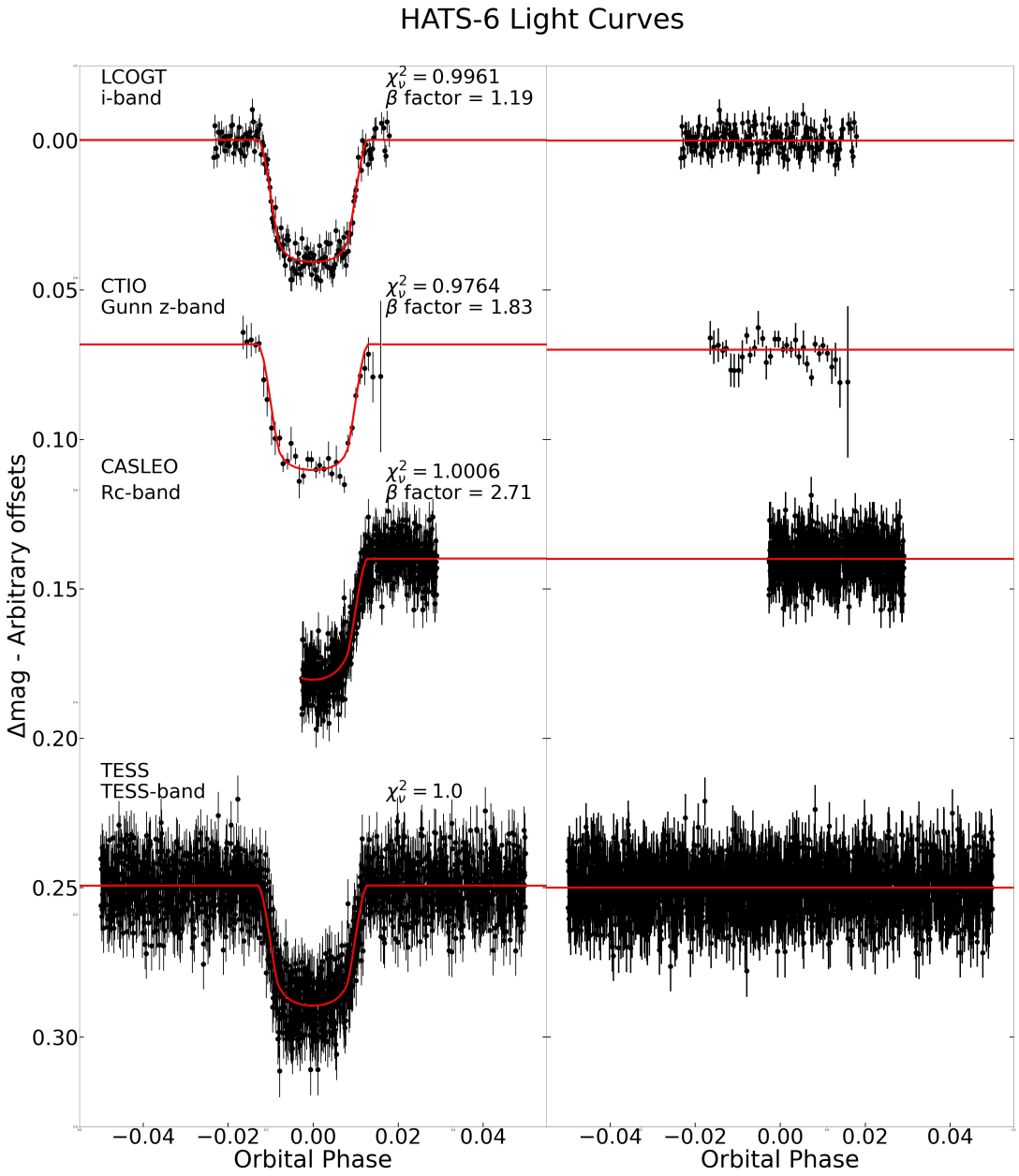

Figure 4.25: Same as Figure 4.24.

Table 4.9: Tabulated transmission spectrum of WASP-69b and the quadratic LD coefficients used.

Author/Source	Filter	λ (nm)	k	c1	c2
EABA	B	437.81	$0.13048\ ^{+0.00403}_{-0.00419}$	0.9332	-0.0745
ReaRea (2016)	Clear	591.20	$0.12584\ ^{+0.00299}_{-0.00314}$	0.7466	0.1296
Bretton (2019)	V	546.61	$0.12342\ ^{+0.00261}_{-0.00264}$	0.7112	0.0836
Gaitan (2020)	R	669.56	$0.13233\ ^{+0.00634}_{-0.00655}$	0.7049	0.1745
Anderson et al. (2014)	-	665.60	$0.12626\ ^{+0.00049}_{-0.00049}$	0.5470	0.1747
Anderson et al. (2014)	-	1050.65	$0.12654\ ^{+0.00102}_{-0.00107}$	0.3573	0.2424
Murgas et al. (2020)	-	525	$0.13092\ ^{+0.00099}_{-0.00101}$	0.6232	0.0881
Murgas et al. (2020)	-	545	0.13089 ± 0.00069	0.5136	0.2417
Murgas et al. (2020)	-	565	$0.13101\ ^{+0.00058}_{-0.00059}$	0.5787	0.1626
Murgas et al. (2020)	-	585	$0.13132\ ^{+0.00031}_{0.00029}$	0.6208	0.0859
Murgas et al. (2020)	-	605	0.13154 ± 0.00030	0.5167	0.1732
Murgas et al. (2020)	-	625	0.13117 ± 0.00052	0.4517	0.2286
Murgas et al. (2020)	-	645	$0.13018\ ^{+0.00046}_{-0.00045}$	0.2041	0.5520
Murgas et al. (2020)	-	665	$0.13033\ ^{+0.00047}_{-0.00048}$	0.2737	0.4376
Murgas et al. (2020)	-	685	0.13087 ± 0.00050	0.3755	0.2982
Murgas et al. (2020)	-	705	0.13035 ± 0.00047	0.2789	0.4001
Murgas et al. (2020)	-	725	$0.13002\ ^{+0.00051}_{-0.00052}$	0.1359	0.5535
Murgas et al. (2020)	-	745	$0.13020\ ^{+0.00055}_{-0.00054}$	0.0733	0.5711
Murgas et al. (2020)	-	775	$0.13014\ ^{+0.00055}_{-0.00054}$	0.0515	0.5919
Murgas et al. (2020)	-	795	$0.13057\ ^{+0.00054}_{-0.00052}$	0.1391	0.4731
Murgas et al. (2020)	-	815	0.13131 ± 0.00058	0.3197	0.2613
Murgas et al. (2020)	-	835	$0.13100\ ^{+0.00056}_{-0.00055}$	0.2823	0.2903
Murgas et al. (2020)	-	855	$0.13035\ ^{+0.00066}_{-0.00063}$	0.1395	0.4610
Murgas et al. (2020)	-	875	$0.12916\ ^{+0.00068}_{-0.00067}$	0.0394	0.5938
Murgas et al. (2020)	-	895	$0.13121\ ^{+0.00081}_{-0.00079}$	0.3570	0.1935

Table 4.10: Tabulated transmission spectrum of HATS-6b and the quadratic LD coefficients used.

Author/Source	Filter	λ (nm)	k	c1	c2
Hartman et al. (2015a)	GROND g-band	450.45	$0.17701\ ^{+0.00102}_{-0.00101}$	0.5415	0.4469
Hartman et al. (2015a)	GROND r-band	609.80	$0.18073\ ^{+0.00064}_{-0.00065}$	0.5917	0.1752
Hartman et al. (2015a)	GROND i-band	760.47	$0.18025\ ^{+0.00067}_{-0.00066}$	0.4290	0.1883
Hartman et al. (2015a)	GROND z-band	892.93	0.17951 ± 0.00062	0.2162	0.4032
Hartman et al. (2015a)	LCOGT i-band	760.70	$0.18090\ ^{+0.00174}_{-0.00172}$	0.0387	0.6798
Hartman et al. (2015a)	CTIO Gunn-z	958.30	$0.18491\ ^{+0.00171}_{-0.00167}$	0.1209	0.4737
CASLEO	Rc	635.80	$0.17717\ ^{+0.00098}_{-0.00094}$	0.3380	0.3956

4.4 Atmospheric Fitting

In this section, we discuss what the fitting of an atmosphere is, why is it needed and how we applied it to this work in order to find the best solution for each one of our systems.

An atmospheric retrieval means one is able to obtain valuable information of the properties in the atmosphere of an exoplanet from a transmission spectrum created from observed data (Deeg & Belmonte 2018). Some of the atmospheric properties that can be inferred from this method include temperature profiles, chemical composition, whether there is the presence or not of cloud and/or hazes, and the energy circulation in the atmosphere (Deeg & Belmonte 2018). When these properties are known, it is possible to understand the temperature profile and physicochemical processes of the planetary atmosphere and how they interact with the incoming radiation from the host star (Deeg & Belmonte 2018).

However, there are also challenges that must be overcome when studying atmospheres beyond our own solar system. Because these planets are at extremely large distances (compared to the solar system), the S/N ratio we get from their spectra is many times more faint when compared to our own solar system planets (Deeg & Belmonte 2018); besides, any kind of existing knowledge gathered from solar system research does not always holds true for exoplanets, and so, the range of physical and chemical parameters needed to study exoplanets is considerably greater than that necessary for the solar system (Deeg & Belmonte 2018). That is because, exoplanets in general, have a broad range of masses, radii, temperatures, surface gravity, chemical compositions, irradiation fluxes, etc. compared to our solar system (Deeg & Belmonte 2018).

For us to obtain the main atmospheric properties of WASP-69b and HATS-6b, we performed a fitting to the transmission spectra obtained in Section 4.3, by using existing grids of atmospheric models taken from the literature that were computed from atmospheric retrieval. The atmospheric model grid used in this work for the atmospheric fitting was taken from Goyal et al. (2018). The grid was created using ATMO, a 1D radiative-convective-chemical equilibrium model for planetary atmospheres (Tremblin et al. 2015, 2016; Amundsen et al. 2014b; Drummond et al. 2016; Tremblin et al. 2017). ATMO works by solving the radiative transfer equation for a given temperature-pressure (P-T) profile, opacities and chemical abundances (Goyal et al. 2018). This grid of transmission spectrum models, represent the transit depth $(Rp/Rs)^2$ of the planet as a function of wavelength λ, and were created by adopting an isothermal P-T profile and chemical equilibrium abundances. This grid of atmospheric models was made for 117 hot exoplanets, with 3920 models per planet, including the two planets of our sample (Goyal et al. 2018). The models were designed with a planet specific approach, meaning that they were generated using the specific values for the stellar radius, planetary radius and surface gravity of the planet (Goyal et al. 2018).

As explained in Goyal et al. (2018), ATMO computes transmission spectra following the formula

$$R^2_{p,eff}(\lambda) = R^2_{p,opq}(\lambda) + 2\int_{R_{p,opq}}^{R_{p,TOA}} bdb(1 - e^{-\tilde{\tau}(b,\lambda)}),$$

where $R_{p,eff}(\lambda)$ is the wavelength-dependent effective planetary radius (atmosphere included), $R_{p,opq}(\lambda)$ is the radius below which the atmosphere is optically thick, $R_{p,TOA}$ is the radius at the top of the atmosphere, b is the impact parameter. All of these parameters are in units of cm (Goyal et al. 2018). In Figure 4.26 we show a detailed diagram with the explanation of how the transmission spectrum is computed. In the transmission spectrum equation, $\tilde{\tau}(b, \lambda)$ is the atmospherical optical depth, that for 1D P-T profiles is spherically symmetric and a function of b, such that

$$\tilde{\tau}(b, \lambda) = \int_{s_{min}}^{s_{max}} ds\kappa_\rho(\lambda, s)\rho(s),$$

where s_{min} is the minimum path coordinate of the ray as it leaves the atmosphere, and s_{max} is the maximum path coordinate of the ray as it enters the atmosphere (see Figure 4.26), with both s_{min} and s_{max} in cm. Next, $\rho(s)$ is the density in g cm^{-3} at the ray path coordinate s, given by $\sqrt{r^2 - b^2}$, where r is the distance measured from the center of the planet to s, with s in cm, and where $\kappa_\rho(\lambda, s)$ is the opacity as a function of wavelength λ and path s in cm^{2}g^{-1} (Goyal et al. 2018). The chemical and thermodynamic properties of the planetary atmosphere are described with the ρ and κ variables respectively (Goyal et al. 2018).

The parameter space of the grid consists of five major physical parameters that affect the transmission spectra of the grid. The first one is the temperature of the planet, which has a considerable effect on the measured transmission spectrum of a planet and spectral features as shown in Fortney et al. (2010). The temperature can be considered the most important parameter that plays a key role in the determination of physical and chemical features of a planetary atmosphere. For example, for temperatures below ∼1000 K, methane (CH_4)

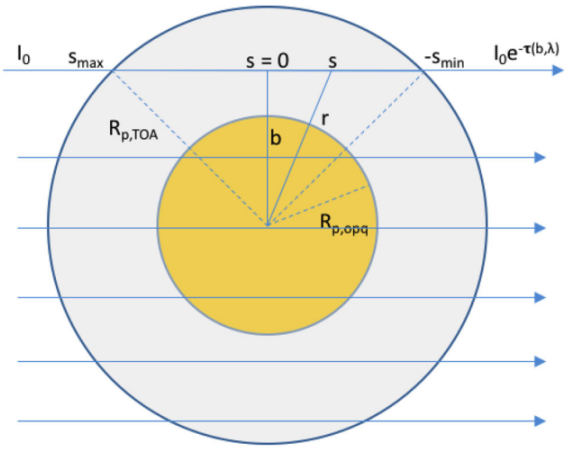

Figure 4.26: Geometry of the transmission spectrum computation for a planet with atmosphere. I_0 is the incoming stellar radiation, $R_{p,eff}(\lambda)$ is the wavelength-dependent radius of the planet including the atmosphere, $R_{p,opq}(\lambda)$ is the radius below which the atmosphere is optically thick, $R_{p,TOA}$ is the radius at the top of the atmosphere, b is the impact parameter, $\tilde{\tau}(b,\lambda)$ is the atmospheric optical depth, s is the ray path coordinate, s_{max} is the maximum ray coordinate, s_{min} is the minimum ray coordinate and r is the distance from the center of the planet to s. Diagram taken from Goyal et al. (2018).

controls the characteristics of the transmission spectrum (Goyal et al. 2018). Once the temperature is 1110 K, a potassium (K) feature begins to emerge, as well as water features that overshadow those of methane. When the temperature reaches 1260 K, sodium (Na) features appear. Carbon monoxide (CO) also starts to appear in the transmission spectrum at about 960 K (Goyal et al. 2018). With temperatures greater than ∼2000 K, features of vanadium(II)[15] oxide VO start to appear. Once the temperature becomes higher, concentrations of VO and titanium(II)[16] oxide TiO become increasingly dominant on the spectral features of the atmosphere (Goyal et al. 2018). As a first guess for the temperature of the planet, the equilibrium temperature T_{eq} is used. The T_{eq} of a planet is defined as the surface blackbody temperature for which the incident stellar flux is balanced by the energy absorbed and re-radiated by the planet or its atmosphere (Perryman 2011). The T_{eq} is calculated from the total incident energy of the star on the planet, the albedo of the planet, its distance to its star, and ignoring other possible heat sources such as tidal deformation, radioactive decay and greenhouse effects (Perryman 2011). The T_{eq} can be written, as used in Charbonneau et al. (2005), with the equation

$$T_{eq} = T_s(\frac{R_s}{2a})^{1/2}[f(1-A_B)]^{1/4},$$

where T_s is the stellar effective temperature, a is the semi-major axis of the planet's orbit, f is the heat redistribution factor that describes the effectiveness of atmospheric circulation and heat transfer, and A_B is the Bond albedo; which is the fraction of energy re-emitted to the amount received, integrated over all wavelengths (Perryman 2011). The presence of an atmosphere is not necessary for the computation of a planetary equilibrium temperature. It is important to note that the T_{eq} does not represent an upper or lower boundary of the planet temperature. The measured temperature of a planet can differ from the T_{eq}. One possible explanation is due to the presence of greenhouse gases in the atmosphere that retain some of the incidental radiation and then re-emit it (Perryman 2011). Molecules such as CO_2, CH_4, CO and H_2O can generate this effect on the atmosphere, if they are present in the planet's atmospheric composition. Other phenomena that can modify the measured temperature of a planet include: a lack of air or greenhouse gases, and the existence of internal energy mechanisms. The temperature of the atmosphere that is computed in the grid, is where the pressure of the atmosphere equals 1 millibar (Goyal et al. 2018), which is the region where the planet radius is defined (Lecavelier Des Etangs et al. 2008). This definition helps to standardize the comparison between multiple transmission spectra with a wide range of variables (Goyal et al. 2018). The atmosphere of a planet has a wide range of temperatures that are dependent on which part of the atmosphere we are in. So, the temperature parameter of each transmission spectrum model is then the temperature that the planet would have at 1 millibar. Which is why the T_{eq} calculated for the planet is used as a first guess to find the temperature in this pressure zone. The

[15]There are several types of vanadium oxides, with each type identified with a roman number, e.g., vanadium(II) oxide VO, vanadium(III) oxide V_2O_3, vanadium(IV) oxide VO_2, and vanadium(V) oxide V_2O_5.

[16]Titanium oxides include titanium(II) oxide TiO, titanium(III) oxide Ti_2O_3 and titanium(IV) oxide TiO_2.

main purpose of the atmospheric fitting is to find the atmospheric model that best fits the temperature and characteristics of the planet's atmosphere. The only restriction to the temperature of the planet comes from the equilibrium temperature. The grid varies the value of the atmospheric temperature in increments of 150 K to a maximum of ±300 K with respect to the T_{eq} of the planet (Goyal et al. 2018), so in total there are five temperature grid points for each planet grid. These temperature grid points can vary for each planet.

The second parameter used in the grid is the metallicity of the planet. The metallicity indirectly affects the chemical composition of the planetary atmosphere and thus, its transmission spectrum (Goyal et al. 2018). At higher metallicities, the value of the transit depth increases, which can be the result of an increase in the opacity of the transmission spectrum for all wavelengths (Fortney et al. 2010; Goyal et al. 2018). At the optical wavelength range, the metallicity can vary the strength of Rayleigh scattering present in the transmission spectrum (Goyal et al. 2018). Where Rayleigh scattering is the scatter of electromagnetic radiation by particles with a size smaller than the wavelength of the radiation itself. In the infrared and near-infrared wavelengths, a higher metallicity tends to increase the strength of all the spectral features present in the spectrum (Goyal et al. 2018). The grid uses metallicity values that go from 0.005, 0.5, 1, 10, 50, 100 to 200 times the solar metallicity.

The third parameter is the carbon-oxygen C/O ratio of the planet. When variations in the C/O ratio exist, there are alterations in the equilibrium chemistry balance between CO, CH_4 and H_2O that affect the resulting transmission spectrum of the atmosphere (Perryman 2011). In general, when the C/O ratio increases, the features of the spectrum go from being H_2O dominant to CH_4 dominant in the infrared region of the spectrum (Goyal et al. 2018). For reference, the solar C/O ratio is 0.56 (Caffau et al. 2011). The effects that C/O ratios can have in the atmosphere of a planet have been studied by Seager et al. (2005), Kopparapu et al. (2012), Madhusudhan (2012) and Moses et al. (2013). The C/O ratio space parameter in the grid is 0.15, 0.35, 0.56, 0.7, 0.75, 1 and 1.5.

The fourth parameter is haze, small scattering aerosol particles (less than 1 μm in size) that are suspended in the planetary atmosphere. Haze is an important source of scattering in planetary atmospheres (Goyal et al. 2018). The opacity of haze in the atmosphere is implemented in ATMO as parameterized enhanced Rayleigh scattering (Goyal et al. 2018). An increase in haze means an increase in the amplitude of Rayleigh scattering slope that tends to mute spectral features (Goyal et al. 2018). Haze affects primarily the optical part of the transmission spectrum of a planet due to its scattering nature (Goyal et al. 2018). It is computed as $\sigma(\lambda) = \alpha_{haze}\sigma_0$, where $\sigma(\lambda)$ is the total scattering cross-section with haze, α_{haze} is the haze enhancement factor and σ_0 is the scattering cross-section due to all other gases (Goyal et al. 2018). The haze space parameter in the grid represents the enhancement factor α_{haze}, and consists of 1, 10, 150 and 1100 times Rayleigh scattering.

The fifth parameter, clouds, are considered as large particles (approximately 20 μm) with gray opacity, similar to the ones used in Sing et al. (2016). When the presence of clouds in the atmosphere is significant, the molecular absorption features are obscured or muted by these clouds (Goyal et al. 2018). In these atmospheric models, clouds are represented as gray scattering. The size of absorption features can be seen as a function of the strength of gray scattering (Goyal et al. 2018), expressed as $\kappa(\lambda)_c = \kappa(\lambda) + \alpha_{cloud}\kappa_{H_2}$, where $\kappa(\lambda)_c$ is the total scattering opacity in cm^2g^{-1}, $\kappa(\lambda)$ is the scattering opacity due to nominal Rayleigh scattering (with the same units), α_{cloud} is the cloudiness strength factor that represents the gray scattering strength, and κ_{H_2} is the scattering opacity due to H_2 at 350 nm which is approximately $2.5 \times 10^{-3} cm^2 gm^{-1}$ (Goyal et al. 2018). The clouds parameter space represents the cloudiness strength factor α_{cloud} and consists of 0, 0.06, 0.2 and 1 times the gray cloud strength factor in the atmosphere. In Tables 4.11 and 4.12 we show the parameter space used by each of the planet specific grids of the two planets.

The model grid presented in Goyal et al. (2018) consider two options when it comes to calculating the chemical abundances, local condensation and rainout condensation. With local condensation, the condensed species are allowed to form and deplete the gas-phase abundance of the elements locally, with each model level being independent and with the same elemental abundance (Goyal et al. 2018). This type of condensation assumes that the formation of condensates in one model level does not affect the availability of elements in other model levels (Goyal et al. 2018). With rainout condensation, the condensed elements are formed, and the elemental abundance of these elements within the condensed species is progressively depleted along the profile (Goyal et al. 2018). Once the particles of elements condense, they sink into the deeper parts of the atmosphere and the elemental abundance of these condensates is depleted from the layers above (Goyal et al. 2018).

With the objective of finding the atmospheric model that best represents the transmission spectrum of each object of our sample through the minimization of the χ^2 statistic, we developed, as part of this work, a code in Python that automatically executes this fit. The atmospheric fitting program that we used is composed of three parts. The first one is designed to setup all the variables and files that serve as inputs for the program.

The second part of the program runs the actual fitting of the atmospheric models to the transmission spectrum of the selected planet. The third part, is used to choose and plot the best atmospheric models found, alongside their parameters and the transmission spectrum of the planets we presented in Section 4.3.

In the first part, the program starts by reading an initial input which declares which one of the planets (WASP-69 and HATS-6) is selected for the fitting. Once the planet is selected, the program reads a first input file that contains columns of data with the name of the planet, a reference identifier assigned to each planet (W69 for WASP-69b, H6 for HATS-6b), the radius of the star (in solar radii), the radius of the planet (in Jupiter radii), the gravity at surface level of the planet and the equilibrium temperature of the planet. Then, the file that contains the data from the transmission spectrum of the specified planet is read as input, along with the directories where the grid of atmospheric models using local and rainout condensation are stored. The data used in the transmission spectra of WASP-69b and HATS-6b are those in Tables 4.9 and 4.10, respectively, shown in Section 4.3. Next, we introduce as input the parameter space of temperature, metallicity, C/O ratio, haze and clouds. Of all these five parameters, only the temperature parameter space varies depending on which system is being fitted, with the other four parameters using the same parameter space for all three planets. For this reason, the program reads a second input file that contains the temperature parameter space used by the specific grid of the selected planet. In this first part of the program, we declare that the amount of degrees of freedom for the fitting is always six, five coming from the parameters used by the grid and one for the scaling done in the vertical axis (transit depth) of the models.

In the second part of the program, where the fitting is done, we begin by opening an output file where the results of the fitting are saved. The general idea of the fitting process is to explore and fit every atmospheric model contained in the grid, while varying the vertical scaling of the transit depth k^2 of each model by a constant amount ($\Delta k^2 = 0.00005$) to find the value of Δk^2 where the χ^2 of every model goes to a minimum. Once the smallest value of χ^2 is found for a model, we calculate the χ^2_ν and save the name of the model, the χ^2, χ^2_ν, and amount of vertical offset of that model in an output text file. To calculate the χ^2 of a model, we must be able to compare it to the transmission spectrum that we have from that planet. In order to do that, we obtain averaged values in the transit depth of the atmospheric model within the range encompassed by the minimum and maximum wavelength of the transmission curve of the filter used for each observation in the transmission spectrum. We compare this averaged value of the model to the one found in the transmission spectrum and calculate the χ^2 of the model. It should be noted that each time the vertical offset added to the atmospheric model changes, the computation of each average value is done once again. We run this entire process twice for the grid, once using the local condensation models and another with the rainout condensation models of the selected planet.

The third and final part of the atmospheric fitting program is used for selecting and plotting the best-fitting atmospheric models found. Here, we read the output files that we have created and search for the local condensation and rainout condensation atmospheric models that have the smallest value of χ^2_ν. Once found, we know the temperature, metallicity, C/O ratio, haze and clouds that these models have, along with the amount of vertical offset added during the fitting of the models. Again, this was done for both the local and rainout condensation atmospheric models, so when creating our final plot output we can display the transmission spectrum of the planet, the models with the smallest χ^2_ν (for local and rainout condensation models), the averaged values of the model in the wavelength intervals of the transmission spectrum observations and the parameters of each model. The results for the targets of our sample, WASP-69 and HATS-6, obtained with this code are shown in Chapter 5.

Table 4.11: Parameter space of the ATMO WASP-69b planet specific grid

T_{eff} (K)	log g (ms^{-2})	$[M/H]$	C/O	$Haze$	$Cloud$
633	5	1	0.35	1	0
833	10	10	0.56	10	0.06
963	20	50	0.7	100	0.2
1113	50	100	1.0	1100	1
1263		200			

Table 4.12: Parameter space of the ATMO HATS-6b planet specific grid

T_{eff} (K)	log g (ms^{-2})	$[M/H]$	C/O	$Haze$	$Cloud$
413	5	1	0.35	1	0
563	10	10	0.56	10	0.06
713	20	50	0.7	100	0.2
863	50	100	1.0	1100	1
1013		200			

Chapter 5

Results

In this chapter, we present the results obtained with the atmospheric fitting process described in Section 4.4. We show the best-fit atmospheric models found for the transmission spectra of WASP-69b and HATS-6b, and a comparison of them with the results from previous works.

5.1 WASP-69b

The best-fitting model found for WASP-69b transmission spectrum has an equilibrium temperature of 1113 K, a metallicity of 2.3, a C/O ratio of 0.56 in the case of the local condensation model, 0.70 for the rainout condensation model, a haze factor of 1 and a cloud factor of 0.20 and 0.06 for the local and rainout condensation models respectively. In Figure 5.1, we present the transmission spectrum of WASP-69b and the best-fitting models found considering local and rainout condensation. In this case, we can see that the parameter values for both the C/O ratio and cloud factor differ from one model to another. We selected the local condensation model, as the final atmospheric model of WASP-69b, as it is the one with the smallest value of χ^2_ν. These results are presented in Table 5.1. This planet specific model of WASP-69b is the one used to study the characteristics of its atmosphere.

Model Parameters	Local Condensation	Rainout Condensation
Equilibrium temperature (T_{eq}) [K]	1113	1113
Metallicity (log [M/H])	2.3	2.3
C/O ratio	0.56	0.70
Haze	1	1
Clouds	0.20	0.06
χ^2_ν	6.1767	6.2134

Table 5.1: Parameter values found from the atmospheric fitting process for the local and rainout condensation models with the smallest value of χ^2_ν for the transmission spectrum of WASP-69b.

In the discovery paper of WASP-69b, Anderson et al. (2014) present an equilibrium temperature of 963 K for this planet. In a second paper, Murgas et al. (2020) use spectral retrieval analysis with PLATON (Zhang et al. 2019) assuming atmospheric scattering models with and without stellar spots, and find an equilibrium temperature of 1203^{+123}_{-429} K and 1227^{+133}_{-164} K respectively. Our own atmospheric analysis determines that the equilibrium temperature of the planet must be around 1113 K, hotter than the result found by Anderson et al. (2014) and cooler than the results presented in Murgas et al. (2020). However, in the case of Murgas et al. (2020), it should be noted that our results actually fall within the uncertainty range of their results. This is the temperature around it starts to be possible to observe Na (∼1260 K) or K (∼1110 K) features in the transmission spectrum of a planet. For the atmospheric model that best fits the transmission spectrum of WASP-69b, we see a Na line appearing near the 600 nm (see Figure 5.1). Indeed, studies by other authors such as Casasayas-Barris et al. (2017) have reported the detection of Na in the atmosphere of WASP-69b. The metallicity of the planet was not a parameter studied in the discovery paper of WASP-69b by Anderson et al. (2014), so we can only compare our results to the one obtained by Murgas et al. (2020). They found the log of the metallicity to be $2.7^{+0.2}_{-0.4}$ with stellar spots, pretty close to the value of 2.3 that we found. Although it is important to keep in

mind that the parameter space of our atmospheric models is a set of six preset values that range from sub-solar to many times the metallicity of the Sun, and the metallicity being log 2.3 (or 200 times the Sun's metallicity) is actually the highest possible value available in the grid, so exploring higher level for the metallicity was simply not an option. However, when accounting for stellar spots, the metallicity value we find actually falls within the range of the uncertainty of Murgas et al. (2020) results. The C/O ratio of 0.56 that we found also falls within the range of the results presented in Murgas et al. (2020), they report a value of $0.41^{+0.19}_{-0.20}$ when considering stellar spots. At this value, that is also the approximate value of the solar C/O ratio, we would expect water and methane abundances to be almost equal to one another (Goyal et al. 2018). A haze factor of one appears to indicate that the presence of hazes in the atmosphere is minimal, and thus, has a weak effect on the dampening of any spectral features, particularly in the visible part of the spectrum. We can also see in Figure 5.1, a small amount of Rayleigh scattering present in the visible-UV part of the spectrum. Finally, a cloud factor of 0.20 seems to indicate a slight presence of clouds in the atmosphere that contribute to gray scattering that can obscure the absorption features of all the wavelengths of the transmission spectrum (Goyal et al. 2018). The best-fitting atmospheric model found for WASP-69b, with the smallest value of χ^2_ν, belongs to the local condensation grid. As previously explained, this means that the abundance of condensate elements in one layer will no influence what happens with the elemental abundances in other layers of the atmospheric model. We did not derive uncertainties for the atmospheric parameters found during the atmospheric fit.

As an experiment, we also decided to run the atmospheric-fitting code that we created, using only the measurements of transit depth that we got from the light curves presented in Murgas et al. (2020), with the results shown in Figure 5.2. The same parameter values were found for both the local condensation and rainout condensation grids, but the local condensation model resulted in a smaller value of χ^2_ν. The results were: an equilibrium temperature of 963 K, a metallicity of -1.0, a C/O ratio of 0.15, a haze factor of 1 and a cloud factor of zero. We present these results in Table 5.2. Using only the light curves from Murgas et al. (2020) we see that the equilibrium temperature of the planet drops to 963 K, a value reported by Anderson et al. (2014) however, both the metallicity and the C/O ratio of the atmosphere change considerably to the values reported by Murgas et al. (2020), well beyond the uncertainties they reports for these parameters in their analysis. Also, the strength factor of both hazes and clouds drops to their respective minimum value possible, meaning in this case, a very weak effect of hazes on the atmosphere and practically no clouds present in it. The results of using only these light curve are shown in Figure 5.2. In this figure, we can also see that the amount of Rayleigh scattering in the transmission spectrum increases significantly. It should be noted that the general shape of our transmission spectrum differs from the transmission spectrum showed in Fig. 5 of Murgas et al. (2020). These differences in the transit depth values found between our work and theirs could be attributed to the fact that they performed the systematics correction simultaneously with the transit fitting, using a Gaussian process. Meanwhile, in this work the systematics corrections were done before the transit fitting with JKTEBOP and using multi-linear regression.

Model Parameters	Local Condensation	Rainout Condensation
Equilibrium temperature (T_{eq}) [K]	963	963
Metallicity (log [M/H])	-1.0	-1.0
C/O ratio	0.15	0.15
Haze	1	1
Clouds	0.00	0.00
χ^2_ν	1.2546	1.2639

Table 5.2: Parameter values found from the atmospheric fitting process for the local and rainout condensation models with the smallest value of χ^2_ν for the transmission spectrum of WASP-69b considering only the light curves of Murgas et al. (2020).

5.2 HATS-6b

The parameters found for the atmospheric model that best fits the HATS-6b transmission spectrum show an equilibrium temperature of 1013 K, a metallicity of 1.7, a C/O ratio of 0.15, a haze factor of 1 and a cloud factor of 0.0. These results are identical for both the local condensation and rainout condensation models, meaning that in both cases, the model with these parameters was the one with the smallest value of χ^2_ν (see Table 5.3). Having both types of condensation models with the same parameters is not something that will necessarily occur for every planet. For the final atmospheric model of HATS-6b, we decided on the local condensation model, given its smaller value of χ^2_ν. This model will be the one used to analyze the physical and chemical properties of the HATS-6b atmosphere.

Model Parameters	Local Condensation	Rainout Condensation
Equilibrium temperature (T_{eq}) [K]	1013	1013
Metallicity (log [M/H])	1.7	1.7
C/O ratio	0.15	0.15
Haze	1	1
Clouds	0.0	0.0
χ^2_ν	22.5044	24.1376

Table 5.3: Parameter values found from the atmospheric fitting process for the local and rainout condensation models with the smallest value of χ^2_ν for the transmission spectrum of HATS-6b.

In the discovery paper of HATS-6b, Hartman et al. (2015a) reported an equilibrium temperature (assuming zero albedo) of $712.8 \pm 5.1K$. However, our atmospheric analysis determined that this temperature should be some 300 degrees hotter at 1013 K. Unfortunately, the other four parameters of our atmospheric model were not studied in Hartman et al. (2015a). With an equilibrium temperature of 1013 K, we see that H_2O absorption bands dominate the spectrum in the near infrared. The logarithm of the metallicity for the best-fitting model is 1.7, which is equivalent to 50 times the solar metallicity. At higher metallicity values likes these, the transit depth of the spectrum becomes higher, as a consequence of an increase in opacity at all wavelengths (Fortney et al. 2010; Goyal et al. 2018). From our atmospheric analysis, we find a C/O ratio of 0.15, which implies that H_2O abundance should be greater than CH_4 abundance in its atmosphere, with a C/O ratio of 0.56 being the transition value (Goyal et al. 2018), where below 0.56, H_2O dominates and above it CH_4 does. For low C/O ratios i.e., C/O <0.56, the abundance of molecules such as CO and CO_2 dominates over other types of carbon-bearing molecules (Goyal et al. 2018). All this would indicate that water features should dominate over methane features in the spectrum of the planet. Moreover, a haze factor of 1 would suggest that the amount of haze in the atmosphere is minimum, and this in turn, means that the amount of Rayleigh scattering in the optical part of the atmosphere is considerable low. We also have a cloud factor of zero, which means no clouds at all in the atmosphere. This means that clouds are not responsible for any type of muting in the absorption features of the spectrum at any given wavelength. In Figure 5.3 we show the results of our atmospheric-fitting code for the transmission spectrum of HATS-6b, as well as the best-fitting models found for its atmosphere. Similar to with WASP-69b, for HATS-6b the best-fitting atmospheric model comes from the local condensation grid, thus, the abundance of condensate elements in one layer does not influence the elemental abundances in other layers. In HATS-6b case, we did not perform a similar analysis to that of WASP-69b because we did not have any type of spectrophotometric observations available from the literature. Same as with WASP-69b, we did not derive uncertainties for the atmospheric parameters found during the atmospheric fit.

It should be noted that HATS-6b is a planet that has very few observations published in the literature, and the ones made, use broad-band filters. To have a better understanding of the characteristics and physical processes that take place within the atmosphere of HATS-6b, it is necessary to acquire more observations in narrow-band filters that cover an ample range of wavelengths. This could be accomplished through spectrophotometric observations of the system during the transit. In the following section, we shall explain further what the results found in this work mean both in the context of these two planets and for Saturn-type planets in general.

In Figures 5.4 and 5.5, and Tables 5.4 and 5.5, we present the O-C values, i.e., the difference between the mid-transit times measured by JKTEBOP and the predicted ones by a linear ephemeris as a function of epoch for WASP-69 and HATS-6 systems, respectively. The ephemeris have the form $t0_{expected} = n * period + t0_{original}$, where n is always a real number $n = (t0_{measured} - t0_{original})/period$. Here, $t0_{measured}$ is the value found for $t0$ from the transit fit (see Section 4.3), for each light curve with JKTEBOP. For WASP-69b, the period P = 3.8681382 ±0.0000017 days, and for HATS-6b, P = 3.3252725 ±0.0000021 days. The adopted value for the

Table 5.4: Tabulated results for the O-C values found for WASP-69b in this work.

Author/Source	Filter	λ (nm)	n	O-C (min)	error
Murgas et al. (2020)	-	525	0	-0.091037	0.131097
Murgas et al. (2020)	-	545	0	0.050918	0.094159
Murgas et al. (2020)	-	565	0	0.155520	0.078707
Murgas et al. (2020)	-	585	0	0.073195	0.067279
Murgas et al. (2020)	-	605	0	0.187387	0.066929
Murgas et al. (2020)	-	625	0	0.431611	0.067593
Murgas et al. (2020)	-	645	0	0.143683	0.057456
Murgas et al. (2020)	-	665	0	-0.140371	0.060440
Murgas et al. (2020)	-	685	0	0.007589	0.061978
Murgas et al. (2020)	-	705	0	0.000000	0.061138
Murgas et al. (2020)	-	725	0	-0.132912	0.064967
Murgas et al. (2020)	-	745	0	-0.089496	0.067496
Murgas et al. (2020)	-	775	0	-0.096999	0.067921
Murgas et al. (2020)	-	795	0	-0.045547	0.065934
Murgas et al. (2020)	-	815	0	0.078408	0.072554
Murgas et al. (2020)	-	835	0	0.138153	0.066235
Murgas et al. (2020)	-	855	0	0.041846	0.079243
Murgas et al. (2020)	-	875	0	-0.119448	0.085483
Murgas et al. (2020)	-	895	0	-0.191520	0.099458
EABA	B	437.81	180	0.438120	1.114182
Rea (2016)	Clear	591.20	-10	4.381185	0.896674
Bretton (2019)	V	546.20	281	1.504627	0.929368
Gaitan (2020)	R	669.56	372	0.402451	1.413932

Table 5.5: Tabulated results for the O-C values found for HATS-6b in this work.

Author/Source	Filter	λ (nm)	n	O-C (min)	error
Hartman et al. (2015a)	GROND g-band	450.45	0	0.318096	0.246942
Hartman et al. (2015a)	GROND r-band	609.80	0	0	0.156986
Hartman et al. (2015a)	GROND i-band	760.47	0	-0.168221	0.156594
Hartman et al. (2015a)	GROND z-band	892.93	0	-0.381355	0.146567
Hartman et al. (2015a)	LCOGT i-band	760.70	-27	0.534327	0.426312
Hartman et al. (2015a)	CTIO Gunn-z	958.30	-165	1.770926	0.699615
CASLEO	Rc	635.80	203	4.184913	0.417060

$t0_{original}$ was the $t0$ found for the best light curve of each planet. In WASP-69b case, this corresponds to the 705 nm light curve in Murgas et al. (2020), and for HATS-6b, it is the GROND r light curve in Hartman et al. (2015a).

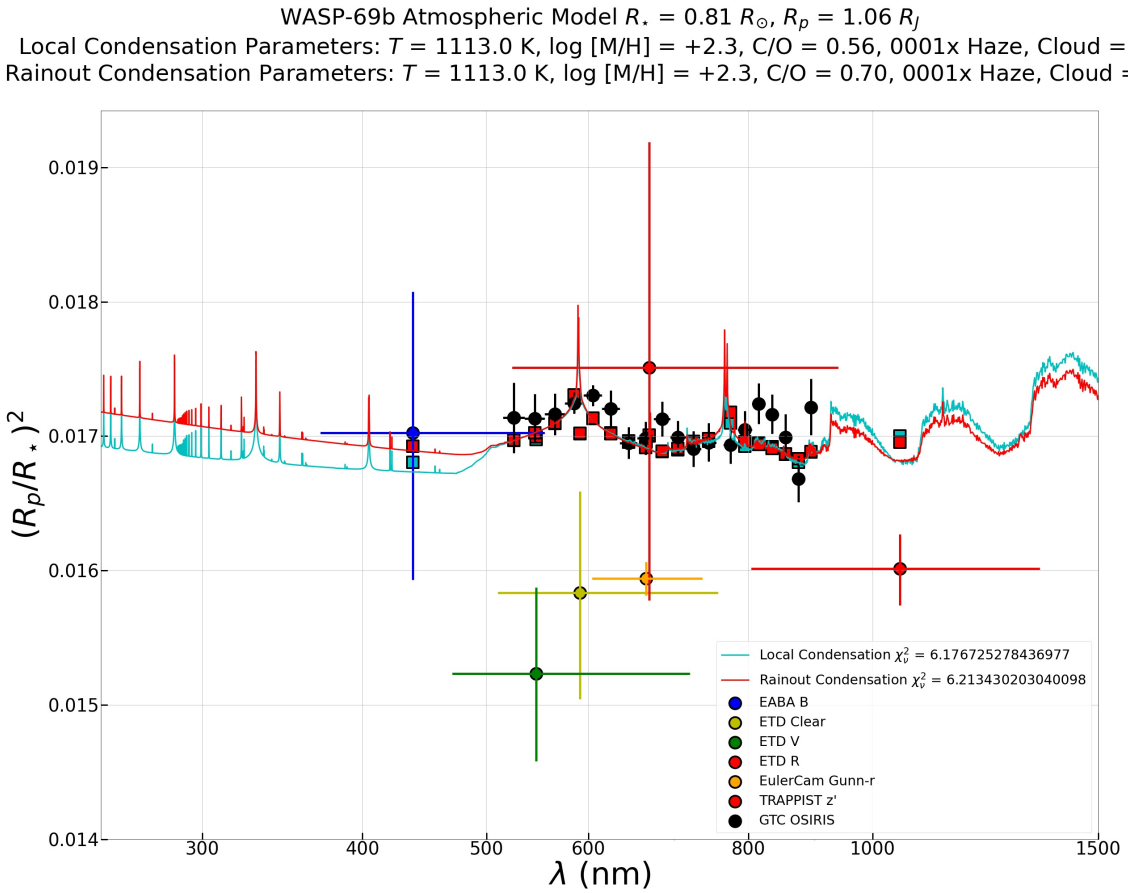

Figure 5.1: Results of the atmospheric fitting for the WASP-69b planet. The vertical axis represents the transit depth ($\Delta F = k^2$) of the planet. The horizontal axis shows the wavelength. The solid circles represent the transit depth measurements made for the observed transits in this work and those taken from the literature, tabulated from the transmission spectrum of the WASP-69b light curves that we showed in Table 4.9. The horizontal bars on the solid circles represent the wavelength band of each filter. The vertical bars on the solid circles represent the 1σ uncertainties of the transit depth measurements. The solid squares in red and cyan show the average transit depth value of the model within the wavelength range of the band used for each data point in the transmission spectrum. The red and cyan solid lines represent the best-fitting models found using the WASP-69b local condensation and rainout condensation models from the Goyal et al. (2018) planet-specific grid.

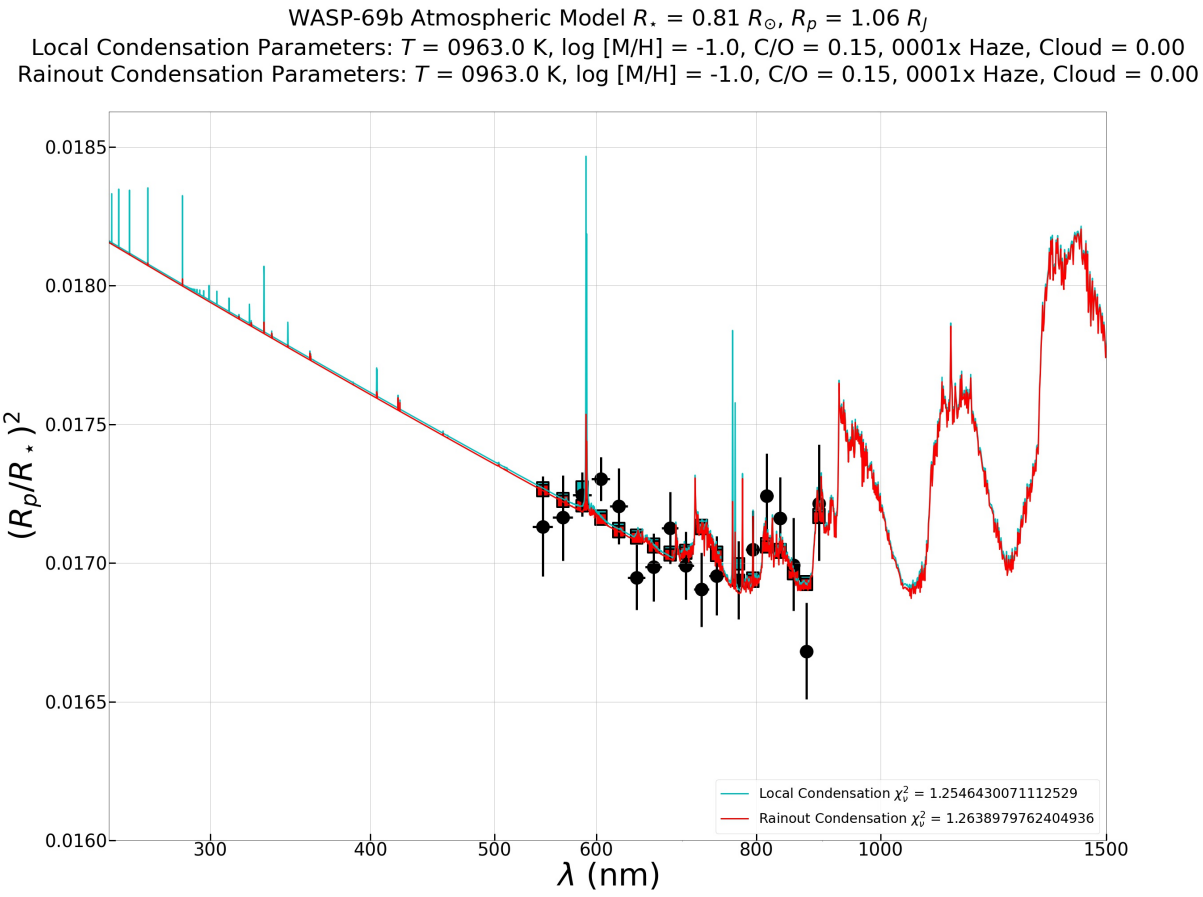

Figure 5.2: Same as Figure 5.1, but only using the transit depth measurements from the light curves of Murgas et al. (2020).

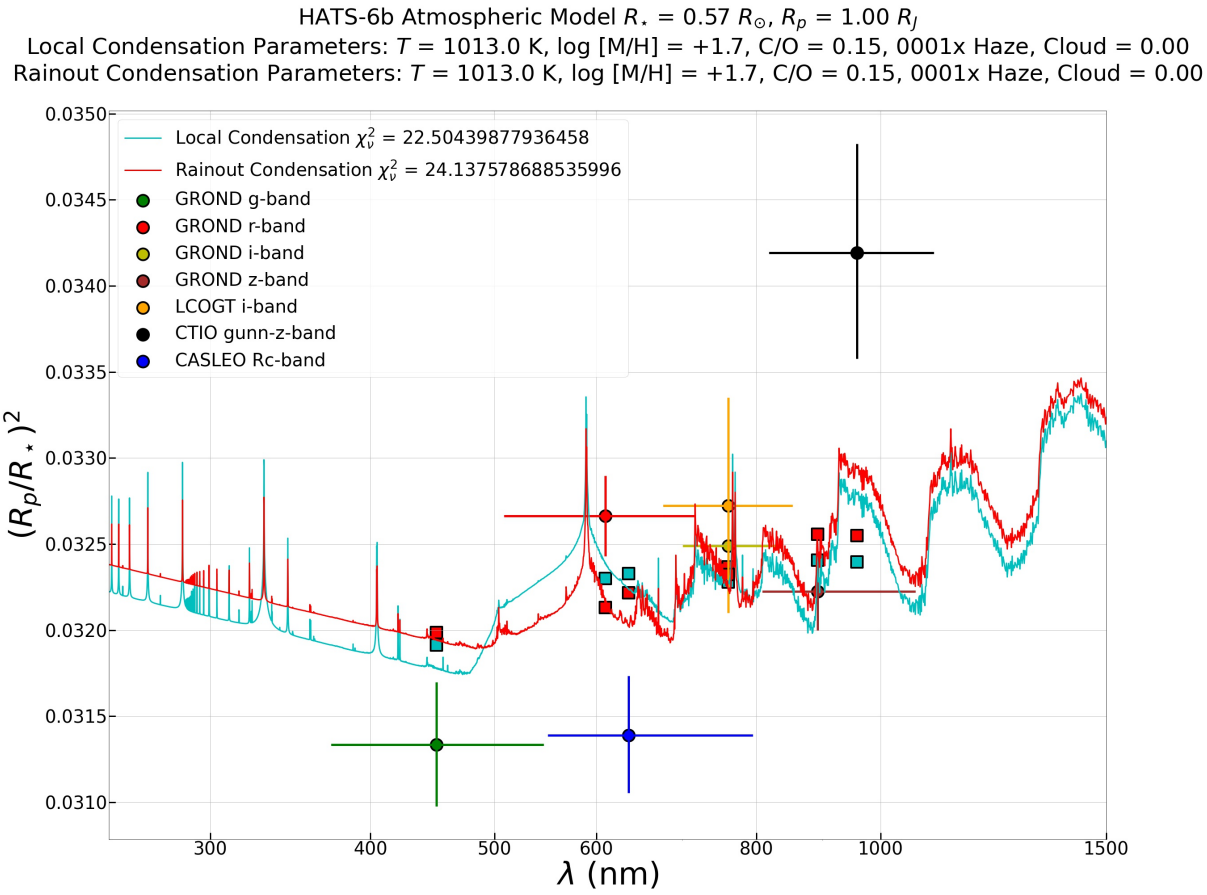

Figure 5.3: Results of the atmospheric fitting for the HATS-6b planet. The vertical axis represents the transit depth ($\Delta F = k^2$) of the planet. The horizontal axis shows the wavelength. The solid circles represent the transit depth from the observed transits in this work and those taken from the literature, tabulated from the transmission spectrum of the HATS-6b light curves that we show in Table 4.10. The horizontal bars on the solid circles represent the wavelength band of each filter. The vertical bars on the solid circles represent the 1σ uncertainties of the transit depth measurements. The solid squares in red and cyan show the average transit depth value of the model within the wavelength range of the band used for each data point in the transmission spectrum. The red and cyan solid lines represent the best-fitting models found using the HATS-6b local condensation and rainout condensation models from the Goyal et al. (2018) planet-specific grid.

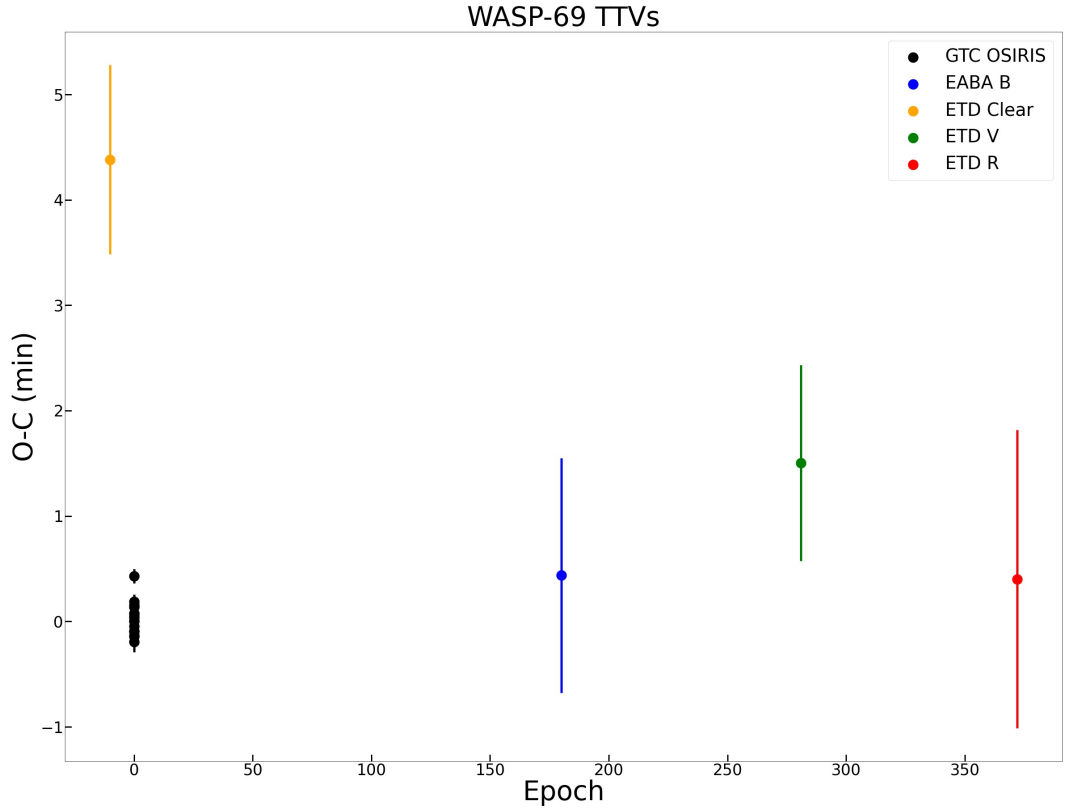

Figure 5.4: O-C values of WASP-69b. The horizontal axis represents the epoch of the light curves. The vertical axis represents the time difference between the expected and measured values for $t0$ in minutes. The spectrophotometric transits from Murgas et al. (2020) were derived from the same white light curve and thus, have the same ephemeris, which is why the appear with the same epoch. The error bars of these results are an average of the 1σ uncertainties found from the Montecarlo fit by JKTEBOP.

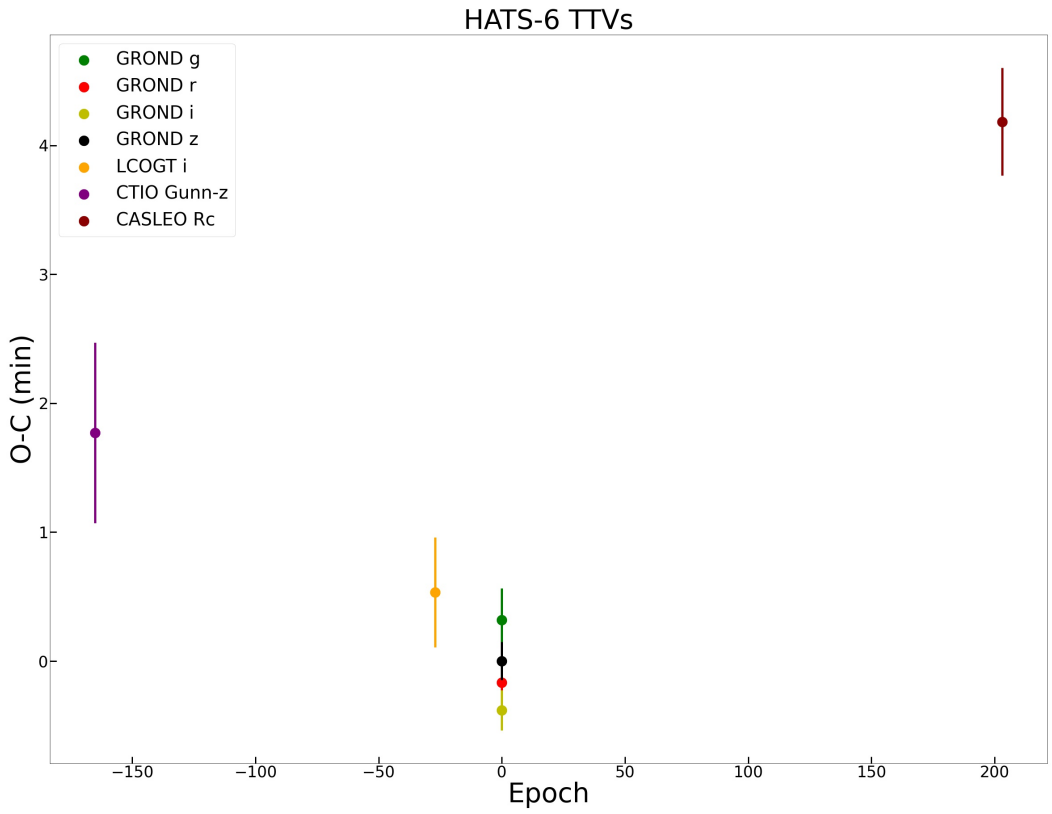

Figure 5.5: O-C values for HATS-6b. The horizontal axis represents the epoch of the light curves. The vertical axis represents the time difference between the expected and measured values for $t0$ in minutes. Transits from the GROND instrument in Hartman et al. (2015a) were taken simultaneously, having the same epoch. The error bars of these results are an average of the 1σ uncertainties.

Chapter 6

Discussion & Conclusions

In this chapter, we present the conclusions gathered from the results obtained in this work. We measured the transit depth of several light curves of two Saturn-type exoplanets in order to better understand the physical and chemical characteristics of their respective atmospheres. Here, we discuss the results obtained for both WASP-69b and HATS-6b, as well as some remarks about the Saturn-type planets in general and some generalized conclusions that can be inferred from the results of this work.

For WASP-69b, our final atmospheric model had an equilibrium temperature of 1113 K, a metallicity 200 times the solar metallicity, a C/O ratio of 0.56, a haze factor of 1 and a cloud factor of 0.2, using local condensation. This model also shows the presence of Na and K absorption at approximately 600 and 800 nm respectively. Our results are in agreement with the Na that appears to have been detected in the atmosphere of the planet in Casasayas-Barris et al. (2017). It has been previously found by Nortmann et al. (2018), that the atmosphere of WASP-69b also contains helium. However, in this work we did not find any evidence of helium contribution to the transmission spectrum. We also found that the atmosphere of the planet contains a small amount of Rayleigh scattering, in agreement with Murgas et al. (2020). Our model also appears to indicate the presence of water absorption features in the near-infrared and infrared parts of the spectrum. However, a lack of data in this part of our transmission spectrum does not allow us to confirm this, given that most of the light curves we gathered from the literature and the ones that we observed ourselves stay roughly within the optical range of the spectrum. Another thing to note, is that the transit depth measurements we obtained for the light curves presented in Murgas et al. (2020) have overall slightly smaller values than those reported in that paper.

For HATS-6b, our final atmospheric model had an equilibrium temperature of 1013 K, a metallicity 50 times the solar metallicity, a C/O ratio of 0.15, a haze factor of 1 and a cloud factor of zero, using local condensation. The analysis of HAST-6b results were a little more complex because currently, there is not much knowledge about the atmosphere of this planet, or many light curves available of its transit since its discovery by Hartman et al. (2015a). Our atmospheric model suggests the presence of Rayleigh scattering in its atmosphere, as well as a Na absorption feature at around 600 nm, and a K absorption feature at around 800 nm. The model also seems to indicate the presence of water vapor in its atmosphere as seen in the near-infrared and infrared parts of the transmission spectrum. However, none of the light curves available cover the near-infrared or infrared part of the transmission spectrum of HATS-6b. Nevertheless, the amount of light curve data that we have for the planet is limited, and having only available broad-band observations made the uncertainties of the fit to increase. More research is needed in order to get a better grasp of the properties of HATS-6b atmosphere.

We noted that the fitted atmospheric parameters do not have estimated uncertainties because we did not derive them. An analysis would be needed in a future work to determine the uncertainties of these parameters. To do this, we would need to analyze the value of χ^2 obtained by every atmospheric model in the grid. For a model with 6 parameters of interest, the 1σ confidence level of $\Delta\chi^2$ would be χ^2+7.04, where χ^2 is the minimum χ^2 found from all atmospheric models in the grid. Plotting this, the horizontal axis would represent an atmospheric parameter (temperature, metallicity, C/O ratio, etc.), and the vertical axis the value of χ^2 found for that model. A figure for each of the six atmospheric parameters would be the result. Another alternative to estimate the uncertainties would be by selecting some models with the minimum χ^2, and obtaining from them the mean and standard deviation of the atmospheric parameters. With this, it is possible to obtain a measurement of the uncertainties in the atmospheric parameters.

For both the WASP-69 and HATS-6 systems, no time transit variations (TTVs) were observed. This is presented

in Figures 5.4 and 5.5 in Chapter 5. It could be left as a potential future work to further refine the periods measured for each planet with more observations and search for any signs of TTVs. All of the photometric data available would be required, including that coming from the WASP and HAT instruments. In this work, we did not fit the period as another parameter because our data and analysis do not encompass the same span of time that the WASP and HAT data do.

Saturn-type planets in general have not been studied in detail compared with other types of planets such as giant Jupiters or Neptune-like planets. However, what is known of them appears to indicate that these planets tend to have atmospheres with a temperature between 800 and 1200 K, possible Na and K absorption in their atmospheres, the presence of water vapor and opaque clouds, with some amount of Rayleigh scattering present in the visible and UV part of their spectrum. The results presented in this work with an atmospheric fitting for our transmission spectra could be improved in a future work, by obtaining more precise results for the characteristics of each planetary atmosphere using an atmospheric retrieval process (see Section 4.4). The work presented in Goyal et al. (2018, 2019) is a good example of this. Apart from the sources studied here, some other Saturn-type planets that have been discovered and studied include WASP-117b (Lendl et al. 2014), WASP-131b (Hellier et al. 2017), and WASP-39b (Faedi et al. 2011).

We note that the analysis and data reduction that we performed in this work using JKTEBOP to measure the transit depth of light curves was done individually and one at a time. A possible alternative to this method would be to run the fitting of all the light curve data at the same time using programs such as EXOFAST (Eastman et al. 2012). A possible explanation to the discrepancies between the transit depth values found for the Murgas et al. (2020) light curves and the values reported here could be attributed to this difference in methodology. In future work, it could be possible to do a comparative analysis between the results obtained by JKTEBOP and EXOFAST. EXOFAST allows for the fitting of all light curves simultaneously, such that the results have a single physical solution for the system. On the other hand, JKTEBOP (as described in Section 4.3) requires that the average photometric parameters be derived initially and then the depth of the transits are fitted, to ensure a single physical solution for the system.

Given that the number of Saturn-type planets analyzed in this work is small, compared to all the known planets of this category, we can say that the results found in this work for WASP-69b and HATS-6b are not enough for us to extrapolate their atmospheric characteristics to all other Saturn-type planets that have been found. However, even these kind of studies, where planets are studied on an individual basis are important, as it allows us to explore the potential of the technique used to characterize planets like this. The results of this work indicate that conducting this kind of analysis in a larger sample of Saturn-like planets is necessary. Another important takeaway from this work, is that the measurements of transit depth obtained through the analysis of light curves made with broad-band filters do not give results as precise a those made with spectrophotometric light curves and this can be seen in the results for WASP-69b, where the uncertainties for all photometric light curves have considerably larger error bars than those made with the spectrophotometric method seen in Murgas et al. (2020). So, in order to obtain a transmission spectrum with a high degree of precision, it is necessary to use only observations made through spectrophotometry. I believe it is also possible to develop a more complete and robust methodology for the study of atmospheric properties that could allow for a quicker and more accurate comparison of atmospheric models with transmission spectra.

Appendix A

Transit Observation Data Of WASP-69 And HATS-6

Table A.1: Differential photometry results obtained with the FOTDIFFLU program for the WASP-69 transit observation in Section 4.2.2

Date (BJD)	Relative Flux	Error
2458363.632391	1.479540	0.002185
2458363.633041	1.505211	0.002232
2458363.633692	1.505137	0.002190
2458363.634342	1.494466	0.002211
2458363.634992	1.499882	0.002217
2458363.635643	1.492006	0.002999
2458363.636293	1.493355	0.002210
2458363.636944	1.481126	0.002185
2458363.637594	1.474822	0.002165
2458363.638245	1.476149	0.002171
2458363.638895	1.492401	0.002194
2458363.639546	1.482179	0.002187
2458363.640196	1.491838	0.002201
2458363.640847	1.490212	0.002161
2458363.641498	1.483858	0.002196
2458363.642148	1.476514	0.002182
2458363.642798	1.468821	0.002123
2458363.643448	1.479487	0.002143
2458363.644099	1.470325	0.002130
2458363.644750	1.485147	0.002151
2458363.645400	1.493442	0.002162
2458363.646050	1.487600	0.002156
2458363.646701	1.462553	0.001728
2458363.647353	1.476124	0.002135
2458363.648003	1.473047	0.002128
2458363.648655	1.472786	0.001578
2458363.649305	1.490035	0.002154
2458363.649955	1.493628	0.001756
2458363.650606	1.481449	0.001742
2458363.651256	1.476590	0.001695
2458363.651907	1.482223	0.001744
2458363.652558	1.472627	0.001589
2458363.653209	1.482015	0.001749
2458363.653860	1.477333	0.001738
2458363.654510	1.469025	0.001734

Date (BJD)	Relative Flux	Error
2458363.655161	1.473197	0.001693
2458363.655812	1.474827	0.001586
2458363.656462	1.469670	0.001686
2458363.657113	1.470097	0.001581
2458363.657764	1.464254	0.001538
2458363.658415	1.464783	0.001574
2458363.659066	1.478669	0.001741
2458363.659717	1.458066	0.002109
2458363.660367	1.476769	0.001737
2458363.661018	1.471893	0.001725
2458363.661669	1.470429	0.001735
2458363.662319	1.470613	0.001740
2458363.662970	1.466439	0.001725
2458363.663620	1.463882	0.001724
2458363.664271	1.455955	0.001710
2458363.664922	1.462672	0.001536
2458363.665573	1.457334	0.001719
2458363.666224	1.465609	0.001725
2458363.666875	1.455116	0.001717
2458363.667525	1.458454	0.001674
2458363.668176	1.459345	0.001677
2458363.668826	1.455095	0.001523
2458363.669476	1.465446	0.001726
2458363.672161	1.470454	0.001532
2458363.672811	1.456312	0.001520
2458363.673461	1.462786	0.001524
2458363.674112	1.463613	0.001525
2458363.674762	1.450062	0.001514
2458363.675413	1.459164	0.001523
2458363.676064	1.449603	0.001517
2458363.676715	1.463314	0.001518
2458363.677365	1.462570	0.001529
2458363.678016	1.454676	0.001521
2458363.678666	1.469748	0.001532
2458363.679317	1.458559	0.001530
2458363.679967	1.460272	0.001521
2458363.680619	1.459223	0.001527
2458363.681270	1.459835	0.001528
2458363.681920	1.453216	0.001515
2458363.682570	1.455194	0.001519
2458363.683221	1.454044	0.001518
2458363.683871	1.451368	0.001515
2458363.684522	1.450555	0.001509
2458363.685172	1.447716	0.001471
2458363.685822	1.444742	0.001506
2458363.686473	1.446820	0.001508
2458363.687124	1.446856	0.001513
2458363.687774	1.459374	0.001521
2458363.688425	1.456576	0.001520
2458363.689075	1.455128	0.001520
2458363.689726	1.457176	0.001522
2458363.690377	1.460607	0.001527
2458363.691027	1.449013	0.001515
2458363.691679	1.454426	0.001515
2458363.692329	1.459514	0.001527
2458363.692980	1.456651	0.001523
2458363.693631	1.456533	0.001523

Date (BJD)	Relative Flux	Error
2458363.694281	1.465728	0.001684
2458363.694932	1.460681	0.001675
2458363.695582	1.462756	0.001677
2458363.696234	1.454974	0.001515
2458363.696884	1.449759	0.001513
2458363.697535	1.453580	0.001556
2458363.698186	1.450690	0.001661
2458363.698836	1.460688	0.001565
2458363.699486	1.460924	0.001676
2458363.700137	1.462280	0.001721
2458363.700787	1.457163	0.001523
2458363.701438	1.459014	0.001716
2458363.702088	1.447690	0.001512
2458363.702739	1.449547	0.001510
2458363.703390	1.444530	0.001505
2458363.704041	1.447354	0.001512
2458363.704691	1.450247	0.001512
2458363.705341	1.446876	0.001546
2458363.705992	1.453142	0.001515
2458363.706642	1.451692	0.001513
2458363.707293	1.458249	0.001671
2458363.709135	1.459210	0.001521
2458363.709786	1.464039	0.001528
2458363.710436	1.450768	0.001508
2458363.711086	1.453575	0.001513
2458363.711737	1.451034	0.001554
2458363.712392	1.458249	0.001671
2458363.713043	1.465714	0.001521
2458363.713694	1.460198	0.001668
2458363.714345	1.451219	0.001511
2458363.714996	1.453526	0.001519
2458363.715646	1.455080	0.001514
2458363.716297	1.457954	0.001516
2458363.716947	1.455009	0.001517
2458363.717597	1.456752	0.001519
2458363.718248	1.453014	0.001513
2458363.718899	1.466024	0.001523
2458363.719550	1.460478	0.001665
2458363.720201	1.455750	0.001514
2458363.720851	1.461520	0.001520
2458363.721502	1.465498	0.001522
2458363.722152	1.457396	0.001513
2458363.722803	1.461590	0.001519
2458363.723454	1.461542	0.001521
2458363.724105	1.460127	0.001520
2458363.724756	1.466968	0.001676
2458363.725407	1.467658	0.001680
2458363.726058	1.470440	0.001681
2458363.727465	1.466779	0.001719
2458363.728115	1.464537	0.001566
2458363.728766	1.466063	0.001526
2458363.729416	1.461682	0.001521
2458363.730066	1.464239	0.001523
2458363.730717	1.470038	0.001531
2458363.731367	1.474331	0.001579
2458363.732017	1.465103	0.001525
2458363.732668	1.474852	0.001686

Date (BJD)	Relative Flux	Error
2458363.733318	1.480376	0.001691
2458363.733968	1.480662	0.001693
2458363.734619	1.474772	0.001533
2458363.735269	1.476581	0.001536
2458363.735919	1.481844	0.001689
2458363.736570	1.476770	0.001685
2458363.737221	1.479159	0.001581
2458363.737871	1.487394	0.001698
2458363.738521	1.480405	0.001692
2458363.739982	1.486462	0.001549
2458363.740632	1.486849	0.001698
2458363.741282	1.491703	0.001745
2458363.741932	1.488757	0.001739
2458363.742583	1.481778	0.001732
2458363.743233	1.479322	0.001728
2458363.743884	1.482957	0.001736
2458363.744534	1.496467	0.001750
2458363.745185	1.488477	0.001743
2458363.745835	1.485291	0.001736
2458363.746486	1.489488	0.001742
2458363.747136	1.481690	0.001734
2458363.747786	1.482735	0.001736
2458363.748437	1.478723	0.001732
2458363.749087	1.487777	0.001742
2458363.749737	1.484930	0.001739
2458363.750388	1.480553	0.001739
2458363.751038	1.482942	0.001737
2458363.751689	1.479712	0.001737
2458363.752340	1.475262	0.001770
2458363.752990	1.484561	0.001735
2458363.753640	1.476532	0.002172
2458363.754291	1.483794	0.001737
2458363.754941	1.477241	0.001774
2458363.755591	1.478020	0.001776
2458363.756242	1.479741	0.001775
2458363.756893	1.475256	0.002165
2458363.757544	1.481975	0.001775
2458363.758195	1.475115	0.001726
2458363.758845	1.484071	0.002454
2458363.761499	1.495788	0.001749
2458363.762150	1.485737	0.001742
2458363.762801	1.568216	0.002329
2458363.764376	1.485337	0.001743
2458363.765027	1.486622	0.001740
2458363.765678	1.485334	0.001745
2458363.766329	1.493089	0.001751
2458363.766980	1.488122	0.001742
2458363.767631	1.485885	0.001739
2458363.768281	1.497421	0.001753
2458363.768932	1.494519	0.001750
2458363.769584	1.485150	0.002187
2458363.770236	1.492995	0.001748
2458363.770886	1.483385	0.002187
2458363.771537	1.496059	0.002203
2458363.772187	1.491372	0.001747
2458363.772838	1.474933	0.001727
2458363.773489	1.490146	0.002144

Date (BJD)	Relative Flux	Error
2458363.774141	1.493620	0.001750
2458363.774792	1.491647	0.002149
2458363.775443	1.490355	0.002142

Table A.2: Differential photometry results obtained with the FOTDIFFLU program for the HATS-6 transit observation.

Date (BJD)	Relative flux	Error
2457398.565551	0.229509	0.001102
2457398.565716	0.226986	0.001090
2457398.565875	0.227405	0.001092
2457398.566040	0.229298	0.001101
2457398.566200	0.232274	0.001115
2457398.566360	0.230144	0.001105
2457398.566522	0.228665	0.001098
2457398.566682	0.229509	0.001102
2457398.566844	0.232274	0.001115
2457398.567004	0.229298	0.001101
2457398.567166	0.229087	0.001100
2457398.567328	0.229298	0.001101
2457398.567489	0.227615	0.001093
2457398.567649	0.229509	0.001102
2457398.567811	0.230569	0.001107
2457398.567973	0.228244	0.001096
2457398.568132	0.229932	0.001104
2457398.568294	0.228876	0.001099
2457398.568456	0.231846	0.001113
2457398.568618	0.229721	0.001103
2457398.568780	0.228876	0.001099
2457398.568941	0.227824	0.001185
2457398.569101	0.229298	0.001101
2457398.569263	0.230569	0.001107
2457398.569425	0.229298	0.001101
2457398.569587	0.230356	0.001106
2457398.569747	0.228876	0.001099
2457398.569909	0.231420	0.001111
2457398.570070	0.228244	0.001096
2457398.570229	0.230569	0.001107
2457398.570392	0.229298	0.001101
2457398.570554	0.229932	0.001104
2457398.570716	0.228034	0.001095
2457398.570874	0.229932	0.001104
2457398.571037	0.229087	0.001100
2457398.571198	0.227615	0.001093
2457398.571360	0.230781	0.001108
2457398.571520	0.229509	0.001102
2457398.571680	0.230356	0.001106
2457398.571842	0.230569	0.001107
2457398.572003	0.230781	0.001108
2457398.572165	0.229087	0.001100
2457398.572324	0.229298	0.001101
2457398.572489	0.231633	0.001112
2457398.572648	0.230356	0.001106
2457398.572810	0.228455	0.001097

Date (BJD)	Relative flux	Error
2457398.572970	0.230781	0.001108
2457398.573132	0.231633	0.001112
2457398.573294	0.229509	0.001102
2457398.573455	0.229932	0.001104
2457398.573617	0.230356	0.001106
2457398.573775	0.227615	0.001093
2457398.573939	0.231633	0.001112
2457398.574101	0.229721	0.001103
2457398.574261	0.228876	0.001099
2457398.574422	0.229298	0.001101
2457398.574581	0.228876	0.001099
2457398.574743	0.230781	0.001108
2457398.574908	0.229298	0.001101
2457398.575065	0.229087	0.001100
2457398.575227	0.229932	0.001104
2457398.575391	0.230994	0.001109
2457398.575551	0.230569	0.001107
2457398.575713	0.229298	0.001101
2457398.575874	0.230144	0.001105
2457398.576034	0.228455	0.001097
2457398.576196	0.230356	0.001106
2457398.576358	0.230569	0.001107
2457398.576520	0.229087	0.001100
2457398.576682	0.229932	0.001104
2457398.576842	0.225944	0.001085
2457398.577004	0.230144	0.001105
2457398.577166	0.231206	0.001110
2457398.577327	0.227405	0.001092
2457398.577486	0.228876	0.001099
2457398.577646	0.226986	0.001090
2457398.577808	0.227196	0.001181
2457398.577969	0.229932	0.001104
2457398.578132	0.231420	0.001111
2457398.578291	0.229087	0.001100
2457398.578450	0.226986	0.001090
2457398.578615	0.232916	0.001118
2457398.578774	0.227824	0.001094
2457398.578936	0.227405	0.001092
2457398.579097	0.229298	0.001101
2457398.579259	0.230994	0.001109
2457398.579423	0.228034	0.001095
2457398.579581	0.230569	0.001107
2457398.579743	0.229721	0.001103
2457398.579903	0.229087	0.001100
2457398.580065	0.229298	0.001101
2457398.580227	0.228244	0.001096
2457398.580388	0.227405	0.001092
2457398.580548	0.230994	0.001109
2457398.580710	0.228455	0.001097
2457398.580872	0.229298	0.001101
2457398.581031	0.227405	0.001092
2457398.581193	0.229721	0.001103
2457398.581352	0.229298	0.001101
2457398.581516	0.229509	0.001102
2457398.581676	0.228455	0.001097
2457398.581838	0.229509	0.001102
2457398.581998	0.229298	0.001101

Date (BJD)	Relative flux	Error
2457398.582159	0.228034	0.001095
2457398.582321	0.226569	0.001088
2457398.582483	0.227615	0.001093
2457398.582642	0.228876	0.001099
2457398.582802	0.228455	0.001097
2457398.582966	0.228665	0.001098
2457398.583125	0.229298	0.001101
2457398.583288	0.227615	0.001093
2457398.583450	0.230569	0.001107
2457398.583609	0.230781	0.001108
2457398.583771	0.228244	0.001096
2457398.583933	0.228455	0.001097
2457398.584093	0.230781	0.001108
2457398.584255	0.228455	0.001097
2457398.584415	0.228876	0.001099
2457398.584578	0.229509	0.001102
2457398.584735	0.228034	0.001095
2457398.584897	0.229087	0.001100
2457398.585058	0.229087	0.001100
2457398.585221	0.229087	0.001100
2457398.585383	0.227196	0.001091
2457398.585542	0.228244	0.001096
2457398.585704	0.231633	0.001112
2457398.585863	0.229509	0.001102
2457398.586025	0.232702	0.001117
2457398.586187	0.229298	0.001101
2457398.586349	0.229932	0.001104
2457398.586510	0.229298	0.001101
2457398.586672	0.228244	0.001096
2457398.586834	0.226360	0.001087
2457398.586994	0.227615	0.001184
2457398.587154	0.229932	0.001104
2457398.587318	0.229298	0.001101
2457398.587478	0.229298	0.001101
2457398.587642	0.228665	0.001098
2457398.587802	0.228244	0.001096
2457398.587964	0.231633	0.001112
2457398.588125	0.230144	0.001105
2457398.588287	0.230994	0.001109
2457398.588447	0.229932	0.001104
2457398.588609	0.230781	0.001108
2457398.588768	0.231846	0.001113
2457398.588930	0.230356	0.001106
2457398.589089	0.230144	0.001105
2457398.589251	0.232274	0.001115
2457398.589413	0.229087	0.001100
2457398.589575	0.231846	0.001113
2457398.589737	0.230994	0.001109
2457398.589897	0.228876	0.001099
2457398.590058	0.228665	0.001098
2457398.590220	0.230356	0.001106
2457398.590382	0.230144	0.001105
2457398.590541	0.228665	0.001098
2457398.590704	0.230994	0.001109
2457398.590863	0.231633	0.001112
2457398.591028	0.230356	0.001106
2457398.591190	0.228034	0.001095

Date (BJD)	Relative flux	Error
2457398.591349	0.232274	0.001115
2457398.591511	0.229932	0.001104
2457398.591672	0.229509	0.001102
2457398.591832	0.229932	0.001104
2457398.591994	0.232060	0.001114
2457398.592156	0.230356	0.001106
2457398.592316	0.229932	0.001104
2457398.592478	0.231846	0.001113
2457398.592639	0.228876	0.001099
2457398.592798	0.229298	0.001101
2457398.592963	0.230144	0.001105
2457398.593120	0.230781	0.001108
2457398.593284	0.231846	0.001113
2457398.593446	0.228244	0.001096
2457398.593609	0.230781	0.001108
2457398.593768	0.230994	0.001109
2457398.593929	0.230356	0.001106
2457398.594092	0.229087	0.001100
2457398.594251	0.231206	0.001110
2457398.594413	0.226986	0.001090
2457398.594575	0.230781	0.001108
2457398.594735	0.229721	0.001103
2457398.594897	0.229298	0.001101
2457398.595058	0.230994	0.001109
2457398.595220	0.228876	0.001099
2457398.595379	0.230144	0.001105
2457398.595539	0.231206	0.001110
2457398.595706	0.230144	0.001105
2457398.595863	0.230356	0.001106
2457398.596025	0.230781	0.001108
2457398.596187	0.228034	0.001095
2457398.596349	0.230356	0.001106
2457398.596510	0.232702	0.001117
2457398.596670	0.229087	0.001100
2457398.596832	0.228244	0.001096
2457398.596992	0.230994	0.001109
2457398.597154	0.229932	0.001104
2457398.597312	0.229087	0.001100
2457398.597474	0.232488	0.001116
2457398.597636	0.231846	0.001113
2457398.597800	0.230781	0.001108
2457398.597960	0.233346	0.001120
2457398.598122	0.229087	0.001100
2457398.598282	0.229721	0.001103
2457398.598444	0.232274	0.001115
2457398.598605	0.231633	0.001112
2457398.598767	0.235288	0.001129
2457398.598929	0.230994	0.001109
2457398.599091	0.231206	0.001110
2457398.599253	0.228034	0.001095
2457398.599412	0.230994	0.001109
2457398.599574	0.233561	0.001121
2457398.599736	0.229721	0.001103
2457398.599897	0.230144	0.001105
2457398.600057	0.230994	0.001109
2457398.600217	0.230994	0.001109
2457398.600379	0.230356	0.001106

Date (BJD)	Relative flux	Error
2457398.600541	0.230994	0.001109
2457398.600703	0.232060	0.001114
2457398.600864	0.231633	0.001112
2457398.601026	0.230781	0.001108
2457398.601184	0.231206	0.001110
2457398.601348	0.230781	0.001108
2457398.601506	0.230994	0.001109
2457398.601669	0.232702	0.001117
2457398.601828	0.231846	0.001113
2457398.601991	0.232702	0.001117
2457398.602152	0.231420	0.001111
2457398.602312	0.231206	0.001110
2457398.602476	0.232274	0.001115
2457398.602636	0.230781	0.001108
2457398.602797	0.230781	0.001108
2457398.602958	0.232702	0.001117
2457398.603119	0.231633	0.001112
2457398.603282	0.232702	0.001117
2457398.603444	0.234639	0.001126
2457398.603602	0.232274	0.001115
2457398.603763	0.234207	0.001124
2457398.603925	0.230994	0.001109
2457398.604087	0.230569	0.001107
2457398.604248	0.231633	0.001112
2457398.604409	0.233131	0.001119
2457398.604572	0.232274	0.001115
2457398.604733	0.232274	0.001115
2457398.604895	0.231633	0.001112
2457398.605055	0.233776	0.001122
2457398.605215	0.233776	0.001122
2457398.605378	0.234423	0.001125
2457398.605539	0.233776	0.001122
2457398.605700	0.233776	0.001122
2457398.605863	0.232274	0.001115
2457398.606024	0.233776	0.001122
2457398.606182	0.232702	0.001117
2457398.606344	0.233776	0.001122
2457398.606505	0.233991	0.001123
2457398.606667	0.234639	0.001126
2457398.606829	0.233346	0.001120
2457398.606987	0.235722	0.001131
2457398.607150	0.234639	0.001126
2457398.607312	0.235072	0.001128
2457398.607472	0.235722	0.001131
2457398.607635	0.235072	0.001128
2457398.607796	0.234423	0.001125
2457398.607958	0.233991	0.001123
2457398.608119	0.235939	0.001133
2457398.608281	0.232702	0.001117
2457398.608443	0.235072	0.001128
2457398.608601	0.235072	0.001128
2457398.608763	0.233131	0.001119
2457398.608925	0.235722	0.001131
2457398.609085	0.235072	0.001128
2457398.609247	0.234855	0.001127
2457398.609405	0.236592	0.001136
2457398.609568	0.236592	0.001136

Date (BJD)	Relative flux	Error
2457398.609731	0.234855	0.001127
2457398.609890	0.236157	0.001134
2457398.610051	0.235939	0.001133
2457398.610216	0.234639	0.001126
2457398.610375	0.234423	0.001125
2457398.610535	0.236157	0.001134
2457398.610696	0.236810	0.001137
2457398.610858	0.234423	0.001125
2457398.611019	0.237247	0.001139
2457398.611182	0.235939	0.001133
2457398.611343	0.234639	0.001126
2457398.611504	0.237684	0.001141
2457398.611666	0.237028	0.001138
2457398.611824	0.238561	0.001145
2457398.611990	0.236592	0.001136
2457398.612150	0.236810	0.001137
2457398.612312	0.236374	0.001135
2457398.612473	0.236592	0.001136
2457398.612635	0.235072	0.001128
2457398.612794	0.237028	0.001138
2457398.612956	0.235505	0.001130
2457398.613118	0.235072	0.001128
2457398.613277	0.235072	0.001128
2457398.613439	0.237247	0.001139
2457398.613599	0.236592	0.001136
2457398.613762	0.238781	0.001146
2457398.613920	0.236374	0.001135
2457398.614085	0.235505	0.001130
2457398.614243	0.237903	0.001142
2457398.614405	0.235939	0.001133
2457398.614566	0.238342	0.001144
2457398.614729	0.235505	0.001130
2457398.614887	0.238122	0.001143
2457398.615036	0.238122	0.001143
2457398.615210	0.239883	0.001151
2457398.615373	0.235722	0.001131
2457398.615534	0.237247	0.001139
2457398.615696	0.237465	0.001140
2457398.615856	0.238122	0.001143
2457398.616019	0.238781	0.001146
2457398.616177	0.237247	0.001139
2457398.616338	0.236810	0.001137
2457398.616499	0.237903	0.001142
2457398.616662	0.236157	0.001134
2457398.616824	0.236157	0.001134
2457398.616984	0.236157	0.001134
2457398.617143	0.235505	0.001130
2457398.617305	0.239001	0.001147
2457398.617467	0.236810	0.001137
2457398.617629	0.239662	0.001150
2457398.617788	0.241213	0.001158
2457398.617953	0.236592	0.001136
2457398.618112	0.239662	0.001150
2457398.618272	0.238342	0.001144
2457398.618434	0.237903	0.001142
2457398.618596	0.235722	0.001131
2457398.618757	0.237028	0.001138

Date (BJD)	Relative flux	Error
2457398.618919	0.236810	0.001137
2457398.619081	0.238781	0.001146
2457398.619243	0.238342	0.001144
2457398.619403	0.235072	0.001128
2457398.619566	0.236374	0.001135
2457398.619725	0.237247	0.001139
2457398.619886	0.237903	0.001142
2457398.620051	0.235505	0.001130
2457398.620210	0.236374	0.001135
2457398.620369	0.238342	0.001144
2457398.620531	0.236374	0.001135
2457398.620693	0.238342	0.001144
2457398.620853	0.236157	0.001134
2457398.621014	0.239221	0.001148
2457398.621176	0.239442	0.001149
2457398.621337	0.236592	0.001136
2457398.621498	0.237903	0.001142
2457398.621661	0.238781	0.001146
2457398.621818	0.239883	0.001151
2457398.623085	0.238561	0.001145
2457398.623248	0.238781	0.001146
2457398.623407	0.240547	0.001155
2457398.623571	0.239221	0.001148
2457398.623729	0.236374	0.001135
2457398.623894	0.240326	0.001154
2457398.624052	0.236374	0.001135
2457398.624214	0.238781	0.001146
2457398.624375	0.238342	0.001144
2457398.624534	0.237247	0.001139
2457398.624696	0.237247	0.001139
2457398.624858	0.239883	0.001151
2457398.625020	0.238781	0.001146
2457398.625181	0.239662	0.001150
2457398.625343	0.239001	0.001147
2457398.625503	0.238781	0.001146
2457398.625667	0.237903	0.001142
2457398.625826	0.236374	0.001135
2457398.625985	0.239442	0.001149
2457398.626147	0.236810	0.001137
2457398.626308	0.237684	0.001141
2457398.626470	0.239662	0.001150
2457398.626633	0.239662	0.001150
2457398.626794	0.239001	0.001147
2457398.626955	0.237903	0.001142
2457398.627113	0.238122	0.001143
2457398.627275	0.239001	0.001147
2457398.627437	0.237028	0.001138
2457398.627599	0.237028	0.001138
2457398.627762	0.238781	0.001146
2457398.627921	0.237903	0.001142
2457398.628081	0.234639	0.001126
2457398.628245	0.239883	0.001151
2457398.628405	0.234639	0.001126
2457398.628567	0.238561	0.001145
2457398.628728	0.237465	0.001140
2457398.628888	0.238122	0.001143
2457398.629051	0.237465	0.001140

Date (BJD)	Relative flux	Error
2457398.629212	0.237903	0.001142
2457398.629370	0.237028	0.001138
2457398.629531	0.239883	0.001151
2457398.629694	0.237903	0.001142
2457398.629856	0.239442	0.001149
2457398.630014	0.237684	0.001141
2457398.630176	0.238122	0.001143
2457398.630340	0.238781	0.001146
2457398.630499	0.239883	0.001151
2457398.630661	0.237684	0.001141
2457398.630823	0.239001	0.001147
2457398.630983	0.239883	0.001151
2457398.631145	0.237465	0.001140
2457398.631304	0.240547	0.001155
2457398.631465	0.237684	0.001141
2457398.631627	0.238122	0.001143
2457398.631789	0.238561	0.001145
2457398.631951	0.237903	0.001142
2457398.632112	0.237247	0.001139
2457398.632270	0.236810	0.001137
2457398.632433	0.238342	0.001144
2457398.632595	0.238342	0.001144
2457398.632757	0.239442	0.001149
2457398.632918	0.239221	0.001148
2457398.633079	0.237684	0.001141
2457398.633241	0.241657	0.001160
2457398.633403	0.238781	0.001146
2457398.633561	0.238122	0.001143
2457398.633722	0.237903	0.001142
2457398.633884	0.238561	0.001145
2457398.634046	0.238561	0.001145
2457398.634206	0.239001	0.001147
2457398.634365	0.236592	0.001136
2457398.634530	0.237247	0.001139
2457398.634690	0.238122	0.001143
2457398.634850	0.236592	0.001136
2457398.635012	0.238781	0.001146
2457398.635172	0.237903	0.001142
2457398.635331	0.240326	0.001154
2457398.635493	0.239001	0.001147
2457398.635658	0.237903	0.001142
2457398.635817	0.239221	0.001148
2457398.635980	0.239001	0.001147
2457398.636141	0.237028	0.001138
2457398.636301	0.236157	0.001134
2457398.636463	0.237247	0.001139
2457398.636622	0.235939	0.001133
2457398.636783	0.239662	0.001150
2457398.636945	0.238342	0.001144
2457398.637108	0.239662	0.001150
2457398.637268	0.240326	0.001154
2457398.637429	0.240769	0.001156
2457398.637592	0.238561	0.001145
2457398.637750	0.236374	0.001135
2457398.637912	0.239662	0.001150
2457398.638073	0.238781	0.001146
2457398.638235	0.238781	0.001146

Date (BJD)	Relative flux	Error
2457398.638395	0.238781	0.001146
2457398.638555	0.237028	0.001138
2457398.638720	0.238342	0.001144
2457398.638878	0.238342	0.001144
2457398.639040	0.238122	0.001143
2457398.639202	0.237903	0.001142
2457398.639363	0.239442	0.001149
2457398.639526	0.238561	0.001145
2457398.639686	0.239001	0.001147
2457398.639848	0.237903	0.001142
2457398.640007	0.237247	0.001139
2457398.640169	0.237684	0.001141
2457398.640331	0.239001	0.001147
2457398.640493	0.239662	0.001150
2457398.640654	0.239883	0.001151
2457398.640814	0.237028	0.001138
2457398.640973	0.240547	0.001155
2457398.641135	0.237247	0.001139
2457398.641297	0.237465	0.001140
2457398.641458	0.237465	0.001140
2457398.641620	0.238122	0.001143
2457398.641779	0.239001	0.001147
2457398.641939	0.239883	0.001151
2457398.642101	0.240326	0.001154
2457398.642262	0.239662	0.001150
2457398.642423	0.239001	0.001147
2457398.642583	0.238781	0.001146
2457398.642748	0.238122	0.001143
2457398.642906	0.238781	0.001146
2457398.643069	0.239442	0.001149
2457398.643230	0.238122	0.001143
2457398.643392	0.238122	0.001143
2457398.643549	0.239442	0.001149
2457398.643714	0.238781	0.001146
2457398.643872	0.239883	0.001151
2457398.644034	0.238122	0.001143
2457398.644196	0.237903	0.001142
2457398.644358	0.238781	0.001146
2457398.644520	0.240991	0.001157
2457398.644680	0.239001	0.001147
2457398.644840	0.240547	0.001155
2457398.645004	0.237465	0.001140
2457398.645163	0.238342	0.001144
2457398.645325	0.238122	0.001143
2457398.645487	0.237903	0.001142
2457398.645648	0.238561	0.001145
2457398.645810	0.239001	0.001147
2457398.645968	0.238561	0.001145
2457398.646129	0.237903	0.001142
2457398.646291	0.239662	0.001150
2457398.646453	0.236810	0.001137
2457398.646614	0.240547	0.001155
2457398.646773	0.240991	0.001157
2457398.646935	0.239662	0.001150
2457398.647100	0.239001	0.001147
2457398.647261	0.237684	0.001141
2457398.647421	0.236374	0.001135

Date (BJD)	Relative flux	Error
2457398.647582	0.237684	0.001141
2457398.647744	0.240991	0.001157
2457398.647904	0.235505	0.001130
2457398.648068	0.239001	0.001147
2457398.648229	0.240326	0.001154
2457398.648389	0.238342	0.001144
2457398.648551	0.238122	0.001143
2457398.648711	0.239221	0.001148
2457398.648871	0.238561	0.001145
2457398.649034	0.239221	0.001148
2457398.649195	0.236374	0.001135
2457398.649357	0.239001	0.001147
2457398.649516	0.237903	0.001142
2457398.649676	0.239883	0.001151
2457398.649842	0.236592	0.001136
2457398.650002	0.237247	0.001139
2457398.650163	0.240104	0.001153
2457398.650323	0.237684	0.001141
2457398.650485	0.237684	0.001141
2457398.650646	0.239001	0.001147
2457398.650808	0.237903	0.001142
2457398.650970	0.236592	0.001136
2457398.651129	0.239001	0.001147
2457398.651291	0.239221	0.001148
2457398.651453	0.238781	0.001146
2457398.651616	0.237684	0.001141
2457398.651776	0.238561	0.001145
2457398.651938	0.238561	0.001145
2457398.652100	0.236810	0.001137
2457398.652261	0.237247	0.001139
2457398.652419	0.237903	0.001142
2457398.652581	0.237465	0.001140
2457398.652743	0.239001	0.001147
2457398.652906	0.237684	0.001141
2457398.653066	0.237028	0.001138
2457398.653225	0.234423	0.001125
2457398.653386	0.236374	0.001135
2457398.653548	0.239221	0.001148
2457398.653710	0.240769	0.001156
2457398.653872	0.235939	0.001133
2457398.654032	0.236592	0.001136
2457398.654190	0.237465	0.001140
2457398.654352	0.237903	0.001142
2457398.654518	0.237247	0.001139
2457398.654676	0.240104	0.001153
2457398.654838	0.237465	0.001140
2457398.654999	0.238781	0.001146
2457398.655161	0.240326	0.001154
2457398.655322	0.239442	0.001149
2457398.655484	0.239442	0.001149
2457398.655644	0.239442	0.001149
2457398.655804	0.239442	0.001149
2457398.655964	0.235722	0.001131
2457398.656126	0.239001	0.001147
2457398.656291	0.238122	0.001143
2457398.656446	0.235939	0.001133
2457398.656610	0.238122	0.001143

Date (BJD)	Relative flux	Error
2457398.656771	0.237247	0.001139
2457398.656933	0.237465	0.001140
2457398.657094	0.236810	0.001137
2457398.657253	0.236810	0.001137
2457398.657415	0.238342	0.001144
2457398.657579	0.238122	0.001143
2457398.657738	0.240547	0.001155
2457398.657900	0.237028	0.001138
2457398.658060	0.237684	0.001141
2457398.658224	0.238342	0.001144
2457398.658385	0.239221	0.001148
2457398.658545	0.237465	0.001140
2457398.658705	0.236374	0.001135
2457398.658867	0.237247	0.001139
2457398.659027	0.237247	0.001139
2457398.659189	0.237465	0.001140
2457398.659352	0.239221	0.001148
2457398.659514	0.238781	0.001146
2457398.659674	0.237465	0.001140
2457398.659836	0.238561	0.001145
2457398.659994	0.235288	0.001129
2457398.660156	0.234423	0.001125
2457398.660318	0.236592	0.001136
2457398.660481	0.237028	0.001138
2457398.660640	0.238122	0.001143
2457398.660799	0.235722	0.001131
2457398.660961	0.238781	0.001146
2457398.661124	0.237903	0.001142
2457398.661285	0.239221	0.001148
2457398.661447	0.237903	0.001142
2457398.661608	0.237247	0.001139
2457398.661769	0.236374	0.001135
2457398.661931	0.238342	0.001144
2457398.662090	0.238561	0.001145
2457398.662251	0.235722	0.001131
2457398.662412	0.236592	0.001136
2457398.662575	0.238561	0.001145
2457398.662733	0.240104	0.001153
2457398.662895	0.235939	0.001133
2457398.663057	0.237465	0.001140
2457398.663218	0.234855	0.001127
2457398.663377	0.238781	0.001146
2457398.663539	0.237903	0.001142
2457398.663702	0.237247	0.001139
2457398.663861	0.239001	0.001147
2457398.664022	0.238122	0.001143
2457398.664183	0.237903	0.001142
2457398.664346	0.238122	0.001143
2457398.664507	0.237684	0.001141
2457398.664664	0.238781	0.001146
2457398.664828	0.235722	0.001131
2457398.664989	0.239883	0.001151
2457398.665149	0.237465	0.001140
2457398.665313	0.240991	0.001157
2457398.665473	0.237028	0.001138
2457398.665635	0.239001	0.001147
2457398.665796	0.237684	0.001141

Date (BJD)	Relative flux	Error
2457398.665956	0.238122	0.001143
2457398.666122	0.238561	0.001145
2457398.666280	0.238342	0.001144
2457398.666441	0.240104	0.001153
2457398.666603	0.237903	0.001142
2457398.666765	0.237465	0.001140
2457398.666926	0.238342	0.001144
2457398.667088	0.236810	0.001137
2457398.667245	0.239221	0.001148
2457398.667407	0.240326	0.001154
2457398.667569	0.238122	0.001143
2457398.667731	0.237028	0.001138
2457398.667892	0.238561	0.001145
2457398.668053	0.237903	0.001142
2457398.668212	0.241213	0.001158
2457398.668377	0.236592	0.001136
2457398.668536	0.235505	0.001130
2457398.668698	0.236810	0.001137
2457398.668858	0.236592	0.001136
2457398.669020	0.236592	0.001136
2457398.669184	0.237028	0.001138
2457398.669341	0.237684	0.001141
2457398.669503	0.237903	0.001142
2457398.669665	0.234855	0.001127
2457398.669826	0.234855	0.001127
2457398.669987	0.237465	0.001140
2457398.670148	0.237247	0.001139
2457398.670308	0.236810	0.001137
2457398.670469	0.238342	0.001144
2457398.670631	0.239442	0.001149
2457398.670790	0.237903	0.001142
2457398.670952	0.235505	0.001130
2457398.671116	0.238342	0.001144
2457398.671274	0.237465	0.001140

Bibliography

Almenara, J. M., Bouchy, F., Gaulme, P., et al. 2013, Astron. & Astrophys., 555, A118

Amundsen, D. S., Baraffe, I., Tremblin, P., et al. 2014a, Astron. & Astrophys., 564, A59

Amundsen, D. S., Baraffe, I., Tremblin, P., et al. 2014b, Astron. & Astrophys., 564, A59

Anderson, D. R., Collier Cameron, A., Delrez, L., et al. 2014, Mon. Not. of the Royal Astron. Soc., 445, 1114

Anderson, D. R., Collier Cameron, A., Hellier, C., et al. 2015, Astron. & Astrophys., 575, A61

Anisman, L. O., Edwards, B., Changeat, Q., et al. 2020, Astronomical Journal, 160, 233

Bakos, G. Á., Lázár, J., Papp, I., Sári, P., & Green, E. M. 2002, Public. of the Astron. Soc. Pac., 114, 974

Bhatti, W., Bakos, G. Á., Hartman, J. D., et al. 2016, arXiv e-prints, arXiv:1607.00322

Boch, T. & Fernique, P. 2014, in Astronomical Society of the Pacific Conference Series, Vol. 485, Astronomical Data Analysis Software and Systems XXIII, ed. N. Manset & P. Forshay, 277

Bond, I. A., Udalski, A., Jaroszyński, M., et al. 2004, Astrophysical Journal, Letters, 606, L155

Bonnarel, F., Fernique, P., Bienaymé, O., et al. 2000, Astron. & Astrophys., Supplement, 143, 33

Borucki, W. J., Koch, D. G., Lissauer, J., et al. 2007, in Astronomical Society of the Pacific Conference Series, Vol. 366, Transiting Extrapolar Planets Workshop, ed. C. Afonso, D. Weldrake, & T. Henning, 309

Bouchy, F., Hebb, L., Skillen, I., et al. 2010, Astron. & Astrophys., 519, A98

Bozza, V., Mancini, L., & Sozzetti, A. 2016, Methods of Detecting Exoplanets, Vol. 428 (Springer)

Brahm, R., Hartman, J. D., Jordán, A., et al. 2018, Astronomical Journal, 155, 112

Bretton, M. 2015, HATS-6 b Transit, provided by the Exoplanet Transit Database

Bretton, M. 2019, WASP-69 b Transit, provided by the Exoplanet Transit Database

Brown, T. M. 2001, Astrophysical Journal, 553, 1006

Brown, T. M., Baliber, N., Bianco, F. B., et al. 2013, Public. of the Astron. Soc. Pac., 125, 1031

Budaj, J., Hubeny, I., & Burrows, A. 2012, Astron. & Astrophys., 537, A115

Burrows, A., Hubeny, I., Budaj, J., Knutson, H. A., & Charbonneau, D. 2007, Astrophysical Journal, Letters, 668, L171

Caffau, E., Ludwig, H. G., Steffen, M., Freytag, B., & Bonifacio, P. 2011, Sol. Phys., 268, 255

Carone, L., Mollière, P., Zhou, Y., et al. 2021, Astron. & Astrophys., 646, A168

Casasayas-Barris, N., Palle, E., Nowak, G., et al. 2017, Astron. & Astrophys., 608, A135

Chamberlain, J. W. & Hunten, D. M. 1987, Theory of planetary atmospheres. An introduction to their physics and chemistry., Vol. 36 (Academic Press)

Charbonneau, D., Allen, L. E., Megeath, S. T., et al. 2005, Astrophysical Journal, 626, 523

Charbonneau, D., Brown, T. M., Latham, D. W., & Mayor, M. 2000, Astrophysical Journal, Letters, 529, L45

Ciceri, S., Mancini, L., Southworth, J., et al. 2016, Mon. Not. of the Royal Astron. Soc., 456, 990

Claret, A. 2000, Astron. & Astrophys., 363, 1081

Claret, A. 2004, Astron. & Astrophys., 428, 1001

Claret, A., Diaz-Cordoves, J., & Gimenez, A. 1995, Astron. & Astrophys., Supplement, 114, 247

Claret, A. & Hauschildt, P. H. 2003, Astron. & Astrophys., 412, 241

Da Costa, G. S. 1992, in Astronomical Society of the Pacific Conference Series, Vol. 23, Astronomical CCD Observing and Reduction Techniques, ed. S. B. Howell, 90

Davis, L. E. 1994, A Reference Guide to the IRAF/DAOPHOT Package, IRAF Programming Group, National Optical Astronomy Observatories, Tucson, Arizona 85726

Deeg, H. J. & Belmonte, J. A. 2018, Handbook of Exoplanets

Demangeon, O. D. S., Faedi, F., Hébrard, G., et al. 2018, Astron. & Astrophys., 610, A63

Diaz-Cordoves, J., Claret, A., & Gimenez, A. 1995, Astron. & Astrophys., Supplement, 110, 329

Djorgovski, S. 1984, in NASA Conference Publication, Vol. 2350, NASA Conference Publication, 152–176

Doyle, L. R., Carter, J. A., Fabrycky, D. C., et al. 2011, Science, 333, 1602

Drummond, B., Tremblin, P., Baraffe, I., et al. 2016, Astron. & Astrophys., 594, A69

Eastman, J., Gaudi, B. S., & Agol, E. 2012, EXOFAST: Fast transit and/or RV fitter for single exoplanet

Eastman, J., Siverd, R., & Gaudi, B. S. 2010, Public. of the Astron. Soc. Pac., 122, 935

Etzel, P. B. 1981, in Photometric and Spectroscopic Binary Systems, 111

Faedi, F., Barros, S. C. C., Anderson, D. R., et al. 2011, Astron. & Astrophys., 531, A40

Fischer, P. D., Knutson, H. A., Sing, D. K., et al. 2016, Astrophysical Journal, 827, 19

Fortney, J. J., Lodders, K., Marley, M. S., & Freedman, R. S. 2008, Astrophysical Journal, 678, 1419

Fortney, J. J., Shabram, M., Showman, A. P., et al. 2010, Astrophysical Journal, 709, 1396

Gaitan, J. 2020, HATS-6 b Transit, provided by the Exoplanet Transit Database

Goyal, J. M., Mayne, N., Sing, D. K., et al. 2018, Mon. Not. of the Royal Astron. Soc., 474, 5158

Goyal, J. M., Wakeford, H. R., Mayne, N. J., et al. 2019, Mon. Not. of the Royal Astron. Soc., 482, 4503

Guillot, T. 2010, Astron. & Astrophys., 520, A27

Hartman, J. D., Bakos, G. Á., Sato, B., et al. 2011, Astrophysical Journal, 726, 52

Hartman, J. D., Bayliss, D., Brahm, R., et al. 2015a, Astronomical Journal, 149, 166

Hartman, J. D., Bhatti, W., Bakos, G. Á., et al. 2015b, Astronomical Journal, 150, 168

Hébrard, G., Santerne, A., Montagnier, G., et al. 2014, Astron. & Astrophys., 572, A93

Hellier, C., Anderson, D. R., Collier Cameron, A., et al. 2017, Mon. Not. of the Royal Astron. Soc., 465, 3693

Hellier, C., Anderson, D. R., Collier Cameron, A., et al. 2015, Astronomical Journal, 150, 18

Hellier, C., Anderson, D. R., Collier Cameron, A., et al. 2010, Astrophysical Journal, Letters, 723, L60

Henry, G. W., Marcy, G. W., Butler, R. P., & Vogt, S. S. 2000, Astrophysical Journal, Letters, 529, L41

Houghton, J. 2002, The Physics of Atmospheres (Cambridge University Press)

Howell, S. B. 1989, Public. of the Astron. Soc. Pac., 101, 616

Howell, S. B. 2006, Handbook of CCD Astronomy, Vol. 5 (Cambridge University Press)

Hubeny, I., Burrows, A., & Sudarsky, D. 2003, Astrophysical Journal, 594, 1011

Janesick, J. & Blouke, M. 1987, Sky and Telescope, 74, 238

Jenkins, J. M., Caldwell, D. A., & Borucki, W. J. 2002, Astrophysical Journal, 564, 495

Johnson, M. C., Dai, F., Justesen, A. B., et al. 2018, Mon. Not. of the Royal Astron. Soc., 481, 596

Jongen, Y. 2020, HATS-6 b Transit, provided by the Exoplanet Transit Database

Kirk, J., López-Morales, M., Wheatley, P. J., et al. 2019, Astronomical Journal, 158, 144

Komacek, T. D., Showman, A. P., & Tan, X. 2017, Astrophysical Journal, 835, 198

Kopal, Z. 1950, Harvard College Observatory Circular, 454, 1

Kopparapu, R. k., Kasting, J. F., & Zahnle, K. J. 2012, Astrophysical Journal, 745, 77

Lecavelier Des Etangs, A., Pont, F., Vidal-Madjar, A., & Sing, D. 2008, Astron. & Astrophys., 481, L83

Lendl, M., Anderson, D. R., Collier-Cameron, A., et al. 2012, Astron. & Astrophys., 544, A72

Lendl, M., Triaud, A. H. M. J., Anderson, D. R., et al. 2014, Astron. & Astrophys., 568, A81

Lightkurve Collaboration, Cardoso, J. V. d. M., Hedges, C., et al. 2018, Lightkurve: Kepler and TESS time series analysis in Python

Maceroni, C. & Rucinski, S. M. 1997, Public. of the Astron. Soc. Pac., 109, 782

Madhusudhan, N. 2012, Astrophysical Journal, 758, 36

Madhusudhan, N. & Seager, S. 2010, Astrophysical Journal, 725, 261

Mancini, L., Esposito, M., Covino, E., et al. 2018, Astron. & Astrophys., 613, A41

Maxted, P. F. L., Anderson, D. R., Collier Cameron, A., et al. 2016, Astron. & Astrophys., 591, A55

Mayor, M. & Queloz, D. 1995, Nature, 378, 355

Merline, W. J. & Howell, S. B. 1995, Experimental Astronomy, 6, 163

Mighell, K. J. 1999, in Astronomical Society of the Pacific Conference Series, Vol. 189, Precision CCD Photometry, ed. E. R. Craine, D. L. Crawford, & R. A. Tucker, 50

Mortara, L. & Fowler, A. 1981, in Society of Photo-Optical Instrumentation Engineers (SPIE) Conference Series, Vol. 290, Proc. SPIE, 28

Moses, J. I., Line, M. R., Visscher, C., et al. 2013, Astrophysical Journal, 777, 34

Murgas, F., Chen, G., Nortmann, L., Palle, E., & Nowak, G. 2020, Astron. & Astrophys., 641, A158

Nikolov, N., Sing, D. K., Gibson, N. P., et al. 2016, Astrophysical Journal, 832, 191

Nortmann, L., Pallé, E., Salz, M., et al. 2018, Science, 362, 1388

Perez-Becker, D. & Showman, A. P. 2013, Astrophysical Journal, 776, 134

Perryman, M. 2011, The Exoplanet Handbook (Cambridge University Press)

Petrucci, R., Jofré, E., Gómez Maqueo Chew, Y., et al. 2020, Mon. Not. of the Royal Astron. Soc., 491, 1243

Petrucci, R. & Jofré, J. E. 2016, Boletin de la Asociacion Argentina de Astronomia La Plata Argentina, 58, 298

Pinhas, A., Madhusudhan, N., Gandhi, S., & MacDonald, R. 2019, Mon. Not. of the Royal Astron. Soc., 482, 1485

Pollacco, D. L., Skillen, I., Collier Cameron, A., et al. 2006, Public. of the Astron. Soc. Pac., 118, 1407

Popper, D. M. 1984, Astronomical Journal, 89, 132

Popper, D. M. & Etzel, P. B. 1981, Astronomical Journal, 86, 102

Rea, D. 2016, WASP-69 b Transit, provided by the Exoplanet Transit Database

Ricker, G. R., Winn, J. N., Vanderspek, R., et al. 2015, Journal of Astronomical Telescopes, Instruments, and Systems, 1, 014003

Sato, B., Fischer, D. A., Henry, G. W., et al. 2005, Astrophysical Journal, 633, 465

Sato, B., Hartman, J. D., Bakos, G. Á., et al. 2012, Publications of the ASJ, 64, 97

Schneider, J., Dedieu, C., Le Sidaner, P., Savalle, R., & Zolotukhin, I. 2011, Astron. & Astrophys., 532, A79

Seager, S. & Mallén-Ornelas, G. 2003, Astrophysical Journal, 585, 1038

Seager, S., Richardson, L. J., Hansen, B. M. S., et al. 2005, Astrophysical Journal, 632, 1122

Seager, S. & Sasselov, D. D. 2000, Astrophysical Journal, 537, 916

Showman, A. P., Lewis, N. K., & Fortney, J. J. 2015, Astrophysical Journal, 801, 95

Sing, D. K. 2010, Astron. & Astrophys., 510, A21

Sing, D. K., Fortney, J. J., Nikolov, N., et al. 2016, Nature, 529, 59

Southworth, J. 2008, Mon. Not. of the Royal Astron. Soc., 386, 1644

Southworth, J. 2013, Astron. & Astrophys., 557, A119

Southworth, J., Bohn, A. J., Kenworthy, M. A., Ginski, C., & Mancini, L. 2020, Astron. & Astrophys., 635, A74

Southworth, J., Bruntt, H., & Buzasi, D. L. 2007, Astron. & Astrophys., 467, 1215

Southworth, J. & Clausen, J. V. 2007, Astron. & Astrophys., 461, 1077

Southworth, J., Maxted, P. F. L., & Smalley, B. 2004, Mon. Not. of the Royal Astron. Soc., 351, 1277

Southworth, J., Smalley, B., Maxted, P. F. L., Claret, A., & Etzel, P. B. 2005, Mon. Not. of the Royal Astron. Soc., 363, 529

Stetson, P. B. 1987, Public. of the Astron. Soc. Pac., 99, 191

Stetson, P. B. 1990, Public. of the Astron. Soc. Pac., 102, 932

Stetson, P. B. 1992a, in Astronomical Society of the Pacific Conference Series, Vol. 25, Astronomical Data Analysis Software and Systems I, ed. D. M. Worrall, C. Biemesderfer, & J. Barnes, 297

Stetson, P. B. 1992b, Journal of the Royal Astron. Soc. of Canada, 86, 71

Stumpe, M. C., Smith, J. C., Catanzarite, J. H., et al. 2014, Public. of the Astron. Soc. Pac., 126, 100

Sudarsky, D., Burrows, A., & Hubeny, I. 2003, Astrophysical Journal, 588, 1121

Sudarsky, D., Burrows, A., & Pinto, P. 2000, Astrophysical Journal, 538, 885

Tremblin, P., Amundsen, D. S., Chabrier, G., et al. 2016, Astrophysical Journal, Letters, 817, L19

Tremblin, P., Amundsen, D. S., Mourier, P., et al. 2015, Astrophysical Journal, Letters, 804, L17

Tremblin, P., Chabrier, G., Mayne, N. J., et al. 2017, Astrophysical Journal, 841, 30

van Hamme, W. 1993, Astronomical Journal, 106, 2096

Wakeford, H. R., Sing, D. K., Deming, D., et al. 2018, Astronomical Journal, 155, 29

Winn, J. N., Holman, M. J., Torres, G., et al. 2008, Astrophysical Journal, 683, 1076

Wolszczan, A. & Frail, D. A. 1992, Nature, 355, 145

Wright, J. T., Marcy, G. W., Howard, A. W., et al. 2012, Astrophysical Journal, 753, 160

Xie, J.-W. 2014, Astrophysical Journal, Supplement, 210, 25

Yang, M., Liu, H.-G., Zhang, H., Yang, J.-Y., & Zhou, J.-L. 2013, Astrophysical Journal, 778, 110

Zhang, M., Chachan, Y., Kempton, E. M. R., & Knutson, H. A. 2019, Public. of the Astron. Soc. Pac., 131, 034501

Zhou, G., Bakos, G. Á., Hartman, J. D., et al. 2017, Astronomical Journal, 153, 211

Zhou, G., Bayliss, D., Penev, K., et al. 2014, Astronomical Journal, 147, 144